Spring 4-28-2013

Numerical Simulation and Optimization of CO2 Sequestration in Saline Aquifers

Zheming Zhang
Washington University in St. Louis

WASHINGTON UNIVERSITY IN ST. LOUIS
School of Engineering & Applied Science
Department of Mechanical Engineering & Materials Science

Dissertation Examination Committee:
Ramesh Agarwal, Chair
Richard Axelbaum
Ken Jerina
Young-Shin Jun
David Peters
Shankar Sastry

Numerical Simulation and Optimization of CO_2 Sequestration in Saline Aquifers

by

Zheming Zhang

A dissertation presented to the
Graduate School of Arts and Sciences
of Washington University in
partial fulfillment of the
requirements for the degree
of Doctor of Philosophy

May 2013
Saint Louis, Missouri

Table of Contents

List of Figures

List of Tables

Acknowledgments

I would like to express my sincere gratitude to my research and academic advisor Dr. Ramesh K. Agarwal for his encouragement and guidance throughout the course of my Ph.D. program. I thank him for his advice and constant support which has made this work possible.

My thanks also go to Dr. Sally Benson and Yanqin Fan at Stanford University, and to Dr. Cheng Zhu and Peng Lu at Indiana University for providing the precious field data. I am also grateful to dissertation committee members for their comments and suggestions. Morgan Brandon's earlier work on the GA optimization module used in this study is also greatly appreciated.

The financial support for this work was provided by the Consortium for Clean Coal Utilization (CCCU) at Washington University in St Louis. It is gratefully acknowledged.

Special thanks are due to the students of the CFD laboratory of the Department of Mechanical Engineering & Materials Science at Washington University in St. Louis, for creating a wonderful learning environment.

Zheming Zhang

Washington University in St. Louis

May 2013

ABSTRACT OF THE DISSERTATION

Numerical Modeling and Simulation of CO_2 Sequestration in Saline Aquifers

by

Zheming Zhang

Doctor of Philosophy in Mechanical Engineering

Washington University in St. Louis, 2013

Professor Ramesh Agarwal, Chair

With heightened concerns on CO_2 emissions from pulverized-coal power plants, there has been major emphasis in recent years on the development of safe and economical Geological Carbon Sequestration (GCS) technology. Although among one of the most promising technologies to address the problem of anthropogenic global-warming due to CO_2 emissions, the detailed mechanisms of GCS are not well-understood. As a result, there remain many uncertainties in determining the sequestration capacity of the formation/reservoir and the safety of sequestered CO_2 due to leakage. These uncertainties arise due to lack of information about the detailed interior geometry of the formation and the heterogeneity in its geological properties such as permeability and porosity which influence the sequestration capacity and plume migration. Furthermore, the sequestration efficiency is highly dependent on the injection strategy which includes injection rate, injection pressure, type of injection well employed and its orientation etc. The goal of GCS is to maximize the sequestration capacity and minimize the plume migration by optimizing the GCS operation before proceeding with its large scale deployment.

In this dissertation, numerical simulations of GCS are conducted using the DOE multi-phase flow solver TOUGH2 (Transport of Unsaturated Groundwater and Heat). A multi-objective optimization code based on genetic algorithm is developed to optimize the GCS operation for a given geological formation. Most of the studies are conducted for

sequestration in a saline formation (aquifer). First, large scale GCS studies are conducted for three identified saline formations for which some experimental data and computations performed by other investigators are available, namely the Mt. Simon formation in Illinois basin, Frio formation in southwest Texas, and the Utsira formation off the coast of Norway. These simulation studies have provided important insights as to the key sources of uncertainties that can influence the accuracy in simulations. For optimization of GCS practice, a genetic algorithm (GA) based optimizer has been developed and combined with TOUGH2. Designated as GA-TOUGH2, this combined solver/optimizer has been validated by performing optimization studies on a number of model problems and comparing the results with brute force optimization which requires large number of simulations. Using GA-TOUGH2, an innovative reservoir engineering technique known as water-alternating-gas (WAG) injection is investigated in the context of GCS; GA-TOUGH2 is applied to determine the optimal WAG operation for enhanced CO_2 sequestration capacity. GA-TOUGH2 is also used to perform optimization designs of time-dependent injection rate for optimal injection pressure management, and optimization designs of well distribution for minimum well interference. Results obtained from these optimization designs suggest that over 20% reduction of in situ CO_2 footprint, greatly enhanced CO_2 dissolution, and significantly improved well injectivity can be achieved by employing GA-TOUGH2. GA-TOUGH2 has also been employed to determine the optimal well placement in a multi-well injection operation. GA-TOUGH2 appears to hold great promise in studying a host of other optimization problems related to GCS.

Preface

Modern society consumes tremendous amount of energy. For example, the worldwide energy consumption was 474 exajoules (i.e., 474×10^{18} J) in 2008 [1]. Moreover, energy demand in the future will keep on increasing due to the growing population, economy and standards of living. A prediction from US Energy Information Agency (EIA) indicates that by year 2035, worldwide energy consumption will reach approximately 780 exajoules, a 50% increase from year 2008 [2]. Prediction and analysis also suggest that the majority of this energy demand will be to be met by utilizing the fossil fuels. About 80%~90% of worldwide energy in 2008 was derived from the combustion of fossil fuels [1],[2]. Utilization of fossil fuels provides the most affordable solution for the world's energy demand, however various undesirable byproducts are generated by the combustion process. One of the major by-products of combustion is carbon dioxide (CO_2), which has been shown to be directly related to the increase in global mean temperature of the surface of the Earth, potentially giving rise to global warming.

Three approaches have been identified by the scientists for mitigating global warming caused by CO_2 emissions from fossil fuel consumption: 1) capture CO_2 from the emission source and permanently sequestrate it; 2) improve combustion efficiency and employ techniques to convert CO_2 to non-greenhouse products; 3) switch the energy generation from greenhouse gas producing sources to renewable carbon free sources. Among all these approaches, carbon capture and geological sequestration (CSGCS) is considered to be most promising in the near term. CSGCS can provide quick, efficient and economical solution to the excessive anthropogenic carbon emission without drastic change in energy generating sources and technologies [3]. Various geological structures have been identified for possible deployment of geological carbon sequestration (GCS): deep saline aquifers, depleted oil/gas reservoirs, unmineable coal seams, etc. Our research in this dissertation focused on saline aquifer geological carbon sequestration (SAGCS). According to the estimates by the US Energy

Information Administration (EIA), deep saline aquifers appear to be the most viable candidates since their storage potential is sufficiently large to achieve the required carbon emission reduction target.

Geological surveys and pilot studies of SAGCS can be dated back to 1990s'. Although some promising results have been obtained, this technology is still not mature for large scale industrial deployment since many uncertainties about sequestration efficiency and safety still exist. Concisely, SAGCS is an activity with coupled physical and chemical phenomena, such as hydrostatics, fluid dynamics, geological physics and chemical reactions, which occur over large spatial and temporal scales. Therefore, the experimental study of SAGCS at all scales is simply not feasible and is likely to be very costly. However, numerical simulations can be performed at all scales to study SAGCS. Thus numerical simulation approach offers a promising avenue for the purpose of quick screening, evaluation, and prediction.

Over the last decade, numerical simulation programs have been developed in U.S, Europe and Japan to determine a priori CO_2 storage capacity of a saline aquifer and to provide risk assessment with reasonable confidence before the actual deployment of CO_2 sequestration can proceed with enormous investment. In US, TOUGH2 (Transport of Unsaturated Groundwater and Heat, version 2.0) numerical simulator has been widely used for such purpose. Numerical simulations using TOUGH2 can help in determining the influence of uncertainties in SAGCS practice such as the hydrogeological properties of the aquifer. Additionally, they can provide insights into the reservoir performance and the flow transport phenomena. The continuing studies of SAGCS require some important but missing features in TOUGH2 that need to be addressed, in particular it does not have the ability to determine optimal parameters such as injection rate, injection pressure, injection depth, injection well orientation and distribution, for optimal CO_2 storage efficiency with minimal leakage risk. Our work in this dissertation has two main objectives: 1) gain insights into the flow transport in SAGCS for improved understanding and estimation of reservoir performance, including its pressure response, leakage risk, and in situ CO_2 footprint; and 2) develop an optimization module for the TOUGH2 solver, enabling it conduct optimization studies on reservoir engineering techniques for improved CO_2 storage efficiency and safety. The accomplishment of those tow tasks will be beneficial for better understanding of in situ

CO_2 migration and trapping mechanisms, as well as the commercialization potential of SAGCS.

Chapter 1

Introduction

1.1 Energy Consumption, Carbon Emission and Global Warming

The world's energy consumption is likely to maintain its substantial growing in the foreseeable future. A projection by US Energy Information Administration (EIA) suggests 50% increase in energy consumption for the next two decades, as shown in Figure 1.1 [2]. In addition, it also appears almost certain that fossil fuels will remain the major energy source (over 70%) to meet increasing energy demand in the absence of significant technological breakthroughs in ability to use other sources of energy especially the renewables [1],[4].

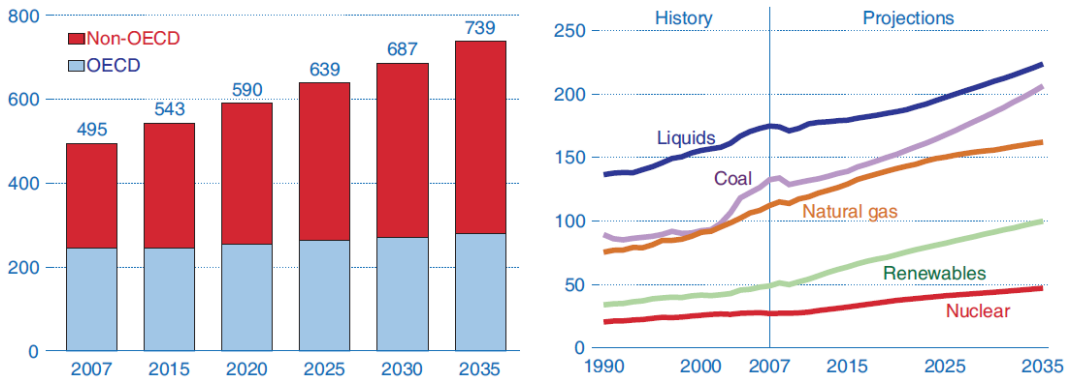

Figure 1.1 World energy consumption projection in quadrillion BTU [2]

Fossil fuels serve as a convenient, efficient, and affordable source of energy. However, the combustion of fossil fuels result in the emission of large amount of CO_2 and other greenhouse gases (GHG). Although it is non-toxic, CO_2 can remain in the atmosphere for hundreds of years and therefore its concentration in atmosphere can continue to increase resulting in change in radiative balance leading to global warming. Recent studies have suggested strong correlation between the elevated concentration of GHG, primarily CO_2, and the increase in the Earth's temperature.

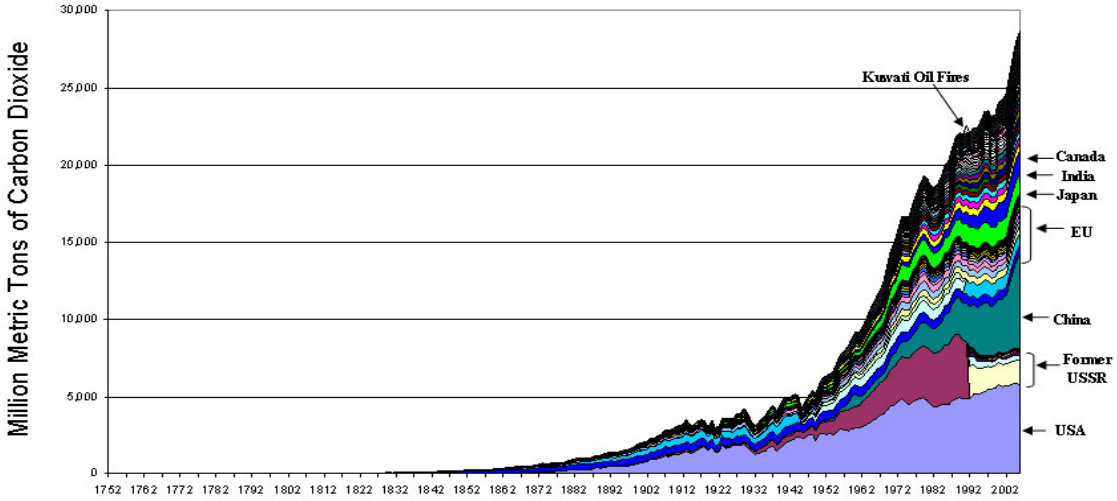

Figure 1.2 World CO_2 emission (EIA, 2010)

Greenhouse gases are gaseous phase components of the atmosphere that contribute to the trapping of radiant heat from the sun within the Earth's atmosphere and thus cause temperature to increase globally. CO_2 emissions have been increasing very rapidly since the beginning of industrialization in early 19th century as shown in Figure 1.2, when human society began to consume large amount of fossil fuels first time in history. Although non-toxic and constitutes nearly 60% of GHG, recent studies have shown strong evidence of CO_2 responsible for global temperature increase due to its ability to stay in the atmosphere for several hundred years increasing its concentration and its strong chemical stability. According to the 2007 Fourth Assessment Report by the Intergovernmental Panel on Climate Change (IPCC), the mean global surface temperature has increased 0.74 ± 0.18 °C during the 20th century as shown in Figure 1.3

[5],[6]. Comparison of Figure 1.2 and Figure 1.3 shows strong correlation between anthropogenic CO_2 emissions and the increase in global surface temperature (i.e. global warming).

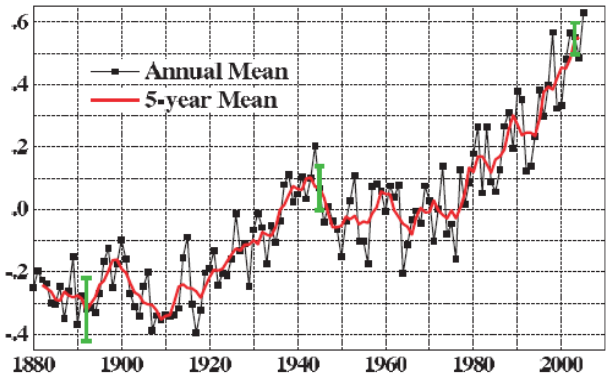

Figure 1.3 Global annual mean temperature anomalies relative to the 1951–1980 average [5][6]

Global warming may result in sea level to rise, oceans to become acidic, changes in the amount and pattern of precipitation, and expansion of subtropical deserts. Other likely effects include changes in the frequency and intensity of extreme weather events, species extinctions, and changes in agricultural yields. The effect of global warming is expected to be strongest in the Arctic region, and it is an alarming fact that the ice cap at the North Pole has shrunk by 20% in past 30 years (as shown in Figure 1.4) [7],[8]. There is little doubt among that if the global warming is not addressed, its effects on climate could be catastrophic to both the human society and the Earth's ecosystem.

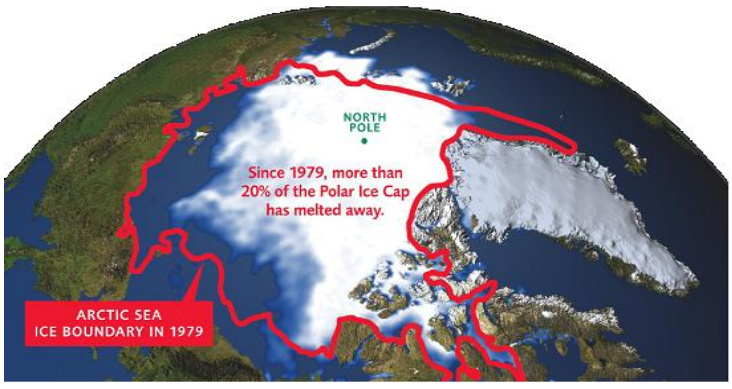

Figure 1.4 Ice cap shrinking at North Pole [7],[8]

Current scientific consensus is that the global warming caused by the anthropogenic CO_2 emission is occurring, and will lead to serious consequences on the Earth's ecosystem if no action is taken. Enhancement of natural/artificial carbon sinks, energy conservation, renewable energy utilization, and efficiency improvements in all sectors of the economy will be needed for reducing the CO_2 emissions. Among the possible remedies, carbon capture and geological sequestration (CCGS) is one of the technologies that can address the reduction of CO_2 emissions into the atmosphere from fossil fuel consuming sources as electricity generating power plants. Quoting from the conclusion section of the Office of Fossil Energy, Department of Energy Report, "*those (other) approaches, however, cannot deliver the level of emissions reduction needed to stabilize the concentrations of greenhouse gases in the atmosphere—especially in view of a growing global demand for energy and the associated increase in GHG emissions. Technological approaches that are effective in reducing atmospheric GHG concentrations and, at the same time, have little or no negative impacts on energy use and economic growth and prosperity are needed. Carbon capture and storage (CCS) promises to provide a significant reduction in greenhouse gas emissions*" [9].

1.2 Geological Carbon Sequestration (GCS)

The technology of carbon capture and geological sequestration (CCGS) offers a practical solution for reducing, and even eliminating, direct CO_2 emissions into the atmosphere. It can therefore help in stabilization of atmospheric CO_2 concentration [10],[11]. CCGS is ideally suited for deployment at large stationary CO_2 emission sources such as power generation facilities based on fossil fuel, fertilizer plants, oil refineries, cement manufacturing plants, etc. "*Information and experience gained from oil and gas exploration, underground natural gas storage, and underground gas injection all support a safe geological storage solution. These information resources, as well as subsurface geologic investigations, suggest that more than enough accessible rock volume exists for geological storage to be a long-term high capacity carbon sequestration option*" [9]. CCGS can be very effective in reducing CO_2 emission into the atmosphere. For example, it is estimated that deploying CCGS at a

modern conventional coal-fired power plant could reduce CO_2 emissions by approximately 80~90 percent compared to the emissions by the same power plant without CCGS [12].

1.2.1 Basic Idea of GCS

The earth crust consists of layers of geological formations, which are generally quite distinct from each other in hydrogeological properties and in situ conditions. A geological reservoir forms when one layer of formation with large void space is bounded by other formations with less void space. Existing oil and gas reservoirs can all be characterized in this manner. Analogously, with proper hydrogeological properties and in situ conditions, highly concentrated CO_2 captured from large stationary emission sources can be injected into such formation and is likely to be confined underground for thousands of years without major concerns of its leakage. Following such idea, CCGS process can be described as follows. CO_2 is first separated at the emission source (the process is known as carbon capture), then compressed and transported to the storage site, and finally injected into the selected geological formation for permanent sequestration (the process is known as geological carbon sequestration). Figure 1.5 shows the schematic of CCGS process [13]. Since the capture process and devices are generally complex and highly energy consuming, large stationary CO_2 sources are more suitable for deployment of carbon capture technology and sequestration. A good example of a large stationary carbon source is the large coal-fired power plant.

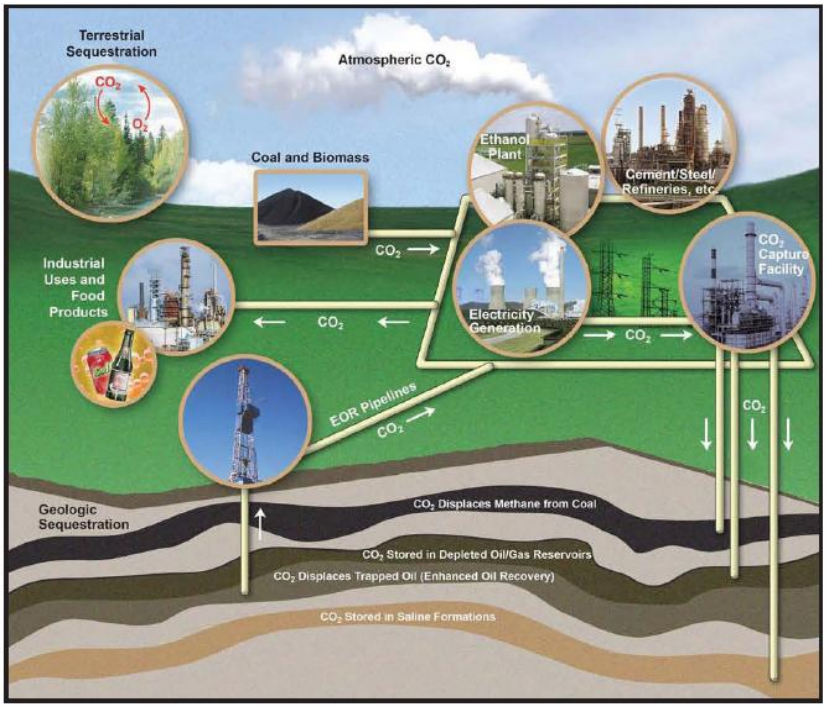

Figure 1.5 Schematic of carbon capture and sequestration [13]

In GCS, four major trapping mechanisms can be identified which are responsible for confining the injected CO_2 in the sequestration site for large time period of thousands of years [14],[15]. These trapping mechanisms are described below.

- **Structural and stratigraphic trapping**. The geological formations selected for GCS can be considered as a CO_2-tight geological container underground. Therefore, three structures recognized as upper, lower and lateral confining formations must present to keep the in situ CO_2 confined within the sequestration formation. The lateral extent of the sequestration formation is generally very large. Due to buoyancy, anticline formed by topography of the upper confining formation is usually the preferred location for structural trapping. Structural trapping occurs very quickly and is responsible for trapping the majority of in situ CO_2 during the early stage of GCS project when most of the in situ CO_2 is still mobile. However, it provides the least amount of security in sequestration due to the relatively high risk of leakage. An illustration of structural trapping is shown in Figure 1.6 (upper-left).

- **Residual trapping**. The void space of the storage formation is originally filled with formation fluid, such as impotable saline water in deep saline formations. When CO_2 is injected into the formation, pressure driven Darcy flow will occur and the original fluid in the formation is displaced as in situ CO_2 moves through the porous formation. As CO_2 continues to migrate away from the injection well, some of it is left behind in the form of disconnected droplets in the pore spaces, which is called residually trapped CO_2. These isolated residual droplets remain immobile due to the capillary pressure. Residual trapping therefore provides better immobility in sequestration, however the amount of residually trapped CO_2 is relatively small and furthermore the development of faults/cracks in the formation may cause its release. An illustration of residual trapping is shown in Figure 1.6 (upper-right).
- **Solubility trapping**. The injected CO_2 can be considered as the solute and the original formation fluid (usually brine) as the solvent. In situ CO_2 gradually dissolves into the formation fluid at the contact surface. Because the formation fluid with dissolved CO_2 is slightly denser than the surrounding fluid, it tends to sink to the bottom of the formation over time, trapping the dissolved CO_2 more securely. However, the dissolution of CO_2 into brine water tends to be a process that occurs very slowly. An illustration of solubility trapping is shown in Figure 1.6 (lower-left).
- **Mineral trapping.** The dissolved CO_2 results in weak carbonic acid formation fluid. Over a long period (hundreds to millions of years), however, the carbonic acid fluid may react with minerals in the formation matrix and form carbonate minerals as precipitates. Once such carbonate minerals are formed, the in situ CO_2 can be considered to be sequestered with ultimate security. An illustration of mineral trapping is shown in Figure 1.6 (lower-right).

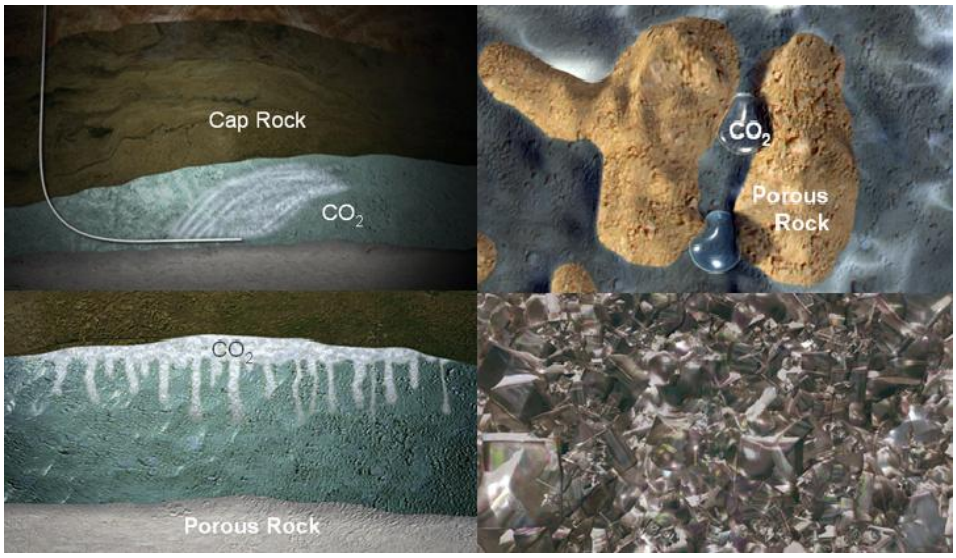

Figure 1.6 Four major trapping mechanisms of GCS [13]

Thus the ultimate sequestration of captured CO_2 is expected to be complete after a considerably long period of time. Each of the above four trapping mechanisms dominates during different time periods in the complete GCS process, therefore having a different level of sequestration security in various time periods. Figure 1.7 illustrates the dominant timeframes, storage contribution, storage security, and governing principles of various trapping mechanisms [16].

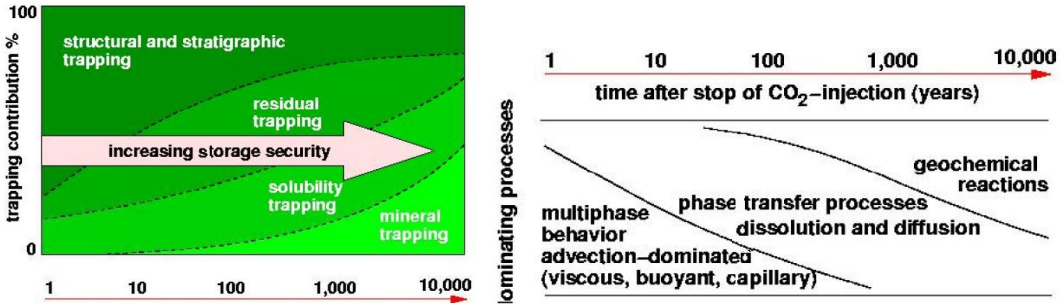

Figure 1.7 Trapping mechanisms and their dominant timeframes, storage contribution, storage security, and governing principles [16]

The sequestrated CO_2 needs to be isolated from the drinking water supply and must be prevented from releasing into the atmosphere, by effectively utilizing all four trapping mechanisms. Monitoring action would be needed throughout the life cycle of the GCS

process to ensure sequestration security. When conducting research on GCS, the time scale of interest as well as the spatial scale of interest must be determined prior to carrying out any substantial work, since different physical principles govern the fate of in situ CO_2 for different trapping mechanisms. Additional details are discussed in Section 2.1.

1.2.2 GCS Practice Worldwide

In the middle of the 1990's, the world's first commercial-scale GCS project, the Sleipner West GCS project, was commissioned in the North Sea, Norway. As a successful demonstration project to show the feasibility of commercial GCS, the Sleipner West GCS project has inspired dozens of other GCS projects worldwide. Some representative pilot and demonstration GCS projects are listed below.

- Sleipner West (Norway): Statoil and the International Energy Agency (IEA) began injecting supercritical phase CO_2 obtained from a nearby natural gas field into the Utsira deep saline formation in North Sea in 1996. The Sleipner GCS project is still ongoing today; approximately one million tons of CO_2 is being sequestrated annually. No significant pressurization or leakage has been reported during the past 16 years of injection.
- Fenn Big Valley (Canada): The Alberta Research Council began injecting CO_2 into deep coal beds for enhanced coal bed methane in 1999. So far, all testing has been successful. Currently the economics of the project is being accessed.
- Weyburn CO_2 Flood Project (Canada): EnCana and IEA began storing CO_2 along with enhanced oil recovery (EOR) in 2000. During 2000 to 2004, more than seven million tons of CO_2 was stored; the geology has been found to be suitable for long-term storage. The site will be maintained to study long-term sequestration. The second phase (2004 and after) includes site characterization, leakage risks, monitoring and verification, and a performance assessment.
- Salah (Algeria). Sonatrach: BP and Statoil began capturing CO_2 from natural gas production in 2004 and started storing it in depleted gas reservoirs, as world's first full-

scale CO_2 capture and storage project at a gas field. The target capacity is one million tons of CO_2 to be stored per year.

- K12-B (Netherlands): Gaz de France is investigating the feasibility of CO_2 storage in depleted natural gas reservoirs on the Dutch continental shelf. K12-B is the first site in the world where CO_2 is injected into the same reservoir from which it originated. The CO_2 injection started in May 2004.
- Snohvit (Norway): Statoil began storing CO_2 from gas production beneath the seabed in April 2008. At full capacity, the target is to store 0.7 million tons of CO_2 per year.
- Ketzin (Germany): GFZ Potsdam, as part of the European research project CO_2SINK, began storing CO_2 in aquifers at a depth of 600 meters on June 30, 2008. The sequestration target is a total of 60000 tons of CO_2 over two years.
- Otway (Australia): CO_2CRC is injecting CO_2 from natural gas wells in hydrocarbon reserves, and the target sequestration amount is 0.1 million tons of CO_2. The objective is to provide technical information on CO_2 storage and monitoring and verification.

1.2.3 GCS Practice in the US (in Collaboration with Canada)

The US is one of the top CO_2 emitting countries and one of the 192 countries that are signatories to the United Nations Framework Convention on Climate Change (UNFCC) – a treaty that calls for stabilization of atmospheric GHG at a level so as to prevent anthropogenic interference with the world's climate. The US Department of Energy is leading the nationwide effort in R&D on GCS related topics and infrastructure construction for GCS projects. The goal is "*to have a technology portfolio by 2012 for safe, cost-effective, and long-term carbon mitigation, management, and storage, which will lead to substantial market penetration after 2012*" [17]. Collaborating with Canada, seven regional carbon sequestration partnerships have been formed by DOE to ensure smooth progress on GCS technology in the two countries (US and Canada). The geographic distribution, participating states/provinces, and the leading organizations of these regional GCS partnerships are shown in Figure 1.8 and summarized in Table 1.1.

Numbers of pilot/demonstration GCS projects are being conducted/proposed by these regional partnerships.

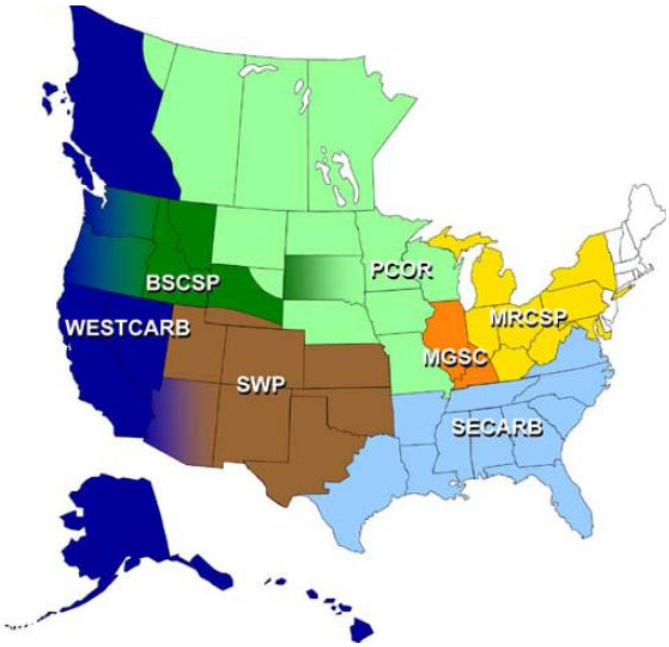

Figure 1.8 Regional Geological Carbon Sequestration Partnerships in US and Canada [17]

Table 1.1 Regional Geological Carbon Sequestration Partnerships in US and Canada [17]

Regional Carbon Sequestration Partnership	Lead Organization	Member State/Province
Midwest Geological Carbon Sequestration Consortium	Illinois State Geological Survey	Illinois, Western Indiana, and Western Kentucky
Midwest Regional Carbon Sequestration Partnership	Battelle Memorial Institute	Eastern Indiana, Eastern Kentucky, Maryland, Michigan, New York Ohio, Pennsylvania, and Western Virginia
Plains CO_2 Reduction Partnership	University of North Dakota, Energy and Environmental Research Center	Easter Montana, Eastern Wyoming, Nebraska, eastern south Dakota, North Dakota, Minnesota, Wisconsin, Iowa, Missouri, Alberta, South Dakota, Manitoba, and Northeastern British Columbia
Southeast Regional Carbon Sequestration Partnership	Southern State Energy Board	East Texas, Arkansas, Louisiana, Mississippi, Alabama, Tennessee, Florida, Georgia, South Carolina, North Carolina, and Virginia
Southwest Regional Partnership	New Mexico Institute of Mining and Technology	West Texas, Oklahoma, Kansas, Colorado, ah, and Eastern Arizona
West Coast Regional Carbon Sequestration Partnership	California Energy Commission	Alaska, Western Arizona, Western British Columbia, California, Hawaii, Nevada, Western Oregon, and Western Washington
Big Sky Carbon Sequestration Partnership	Montana State University	Montana, Idaho, South Dakota, Wyoming, Eastern Oregon and Washington, and adjacent areas in British Columbia and Alberta

1.3 Saline Aquifer Geological Carbon Sequestration (SAGCS)

Studies on GCS have suggested that various geological structures can serve as potential CO_2 storage sites. The major geological carbon sinks include the following structures: 1) conventional hydrocarbon reservoirs, 2) un-minable coal seams, 3) matured oil/gas reservoirs, 4) deep saline formations. Among these candidates, our research is focused on carbon sequestration in saline aquifers considering the following facts.

- Concentrated locations of major sources of CO_2 (such as power plants) are close to existing saline aquifers.
- Geological survey has confirmed vast geological distribution of deep saline formations possibly suitable for GCS in US and Canada.
- Preliminary estimates have suggested large storage capacity of the existing deep saline formations. The US DOE estimates an aggregate storage capacity of approximately 919~3378 billion metric tons of CO_2 for SAGCS in US, which accounts for 80~90 percent of US overall GCS potential [17].
- Since most of the saline formations are located deep underground, i.e., at least 800 m below the sea level, they provide great potential for secured long-term sequestration.
- Significant number of surveys, research projects, and commercial practices have already been carried out for SAGCS, making it attractive for further research and technical contributions.

The vast geographic distribution of deep saline aquifers over North America has been identified by DOE, as shown in Figure 1.9. The DOE estimated storage capacity for SAGCS takes into account more than 80 percent of the overall storage capacity of all possible GCS sites, as given in Table 1.2. In Table 1.2, the low-end capacity of 3634 billion tons of CO_2 is estimated under the condition that ineffective storage may occur due to improper and non-optimized sequestration approaches; on the other hand, the high-end capacity of 13909 billion tons of CO_2 is estimated under the conditions that most effective and optimal storage takes place. It can be seen that the high-end

estimated capacity is nearly four times the low-end estimated capacity. The large difference in estimated storage capacity implies that it is important to deploy optimized reservoir engineering techniques for effective utilization of storage potential and successful GCS practice.

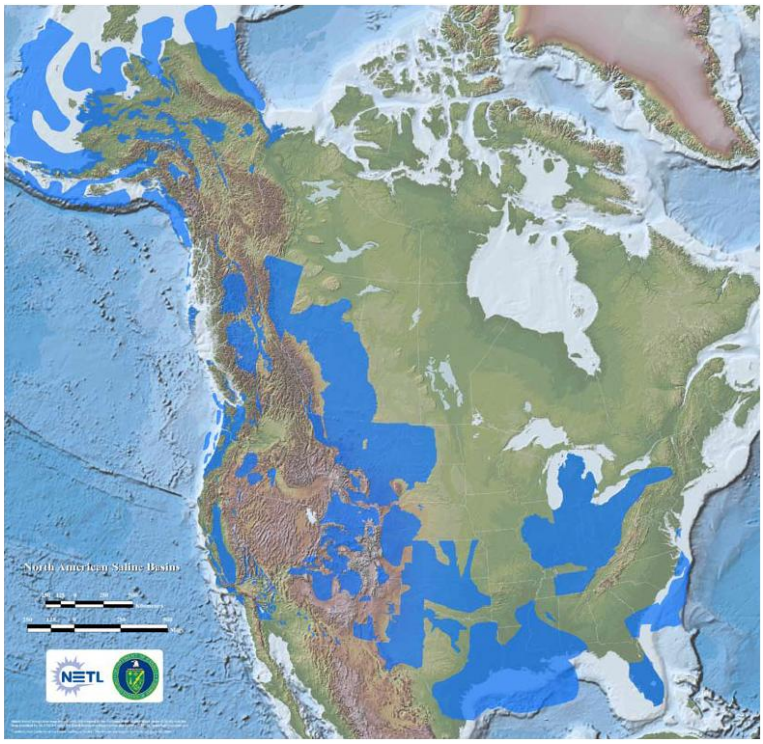

Figure 1.9 Deep saline aquifers in U.S and Canada (blue areas) [17]

Table 1.2 Saline aquifer storage capacity of GCS for different RCSPs [17]

CO_2 Storage Resource Estimates by RCSPs for Saline Formations				
	Low		High	
RCSPs	**Billion Tons**	**Billion Tons**	**Billion Tons**	**Billion Tons**
BSCSP	460.9	508.0	1831.5	2018.9
MGCS	29.2	32.1	116.6	128.6
MRCSP	49.6	54.7	199.1	219.5
PCOR	185.6	204.6	185.6	204.6
SECARB	2274.6	2507.3	9098.4	10029.3
SWP	92.4	101.9	368.9	406.6
WESTCARB	204.5	225.4	818.2	901.9

In Canada and US, several saline aquifer carbon sequestration pilot/demonstration projects are currently being conducted by different RCSPs. Three representative projects are summarized below.

- The Fort Nelson project (PCOR): Approximately 1.1 million tons of sour CO_2 (mixture of CO_2 and hydrogen sulfide H_2S) is injected annually; it is captured from one of the largest gas processing plants. The sour CO_2 is compressed and transported approximately 9 miles in supercritical state through a pipeline to the target injection location. The storage site is the Devonian-age Elk Point carbonate rock formation located in relatively close proximity to the gas plant at a depth of over 2,195 meters [18].
- Tuscaloosa/Paluxy project (SECARB): SECARB is conducting a two-step, large-volume injection test in the lower Tuscaloosa Formation and Paluxy Formation, a key component of a large regional group of similar formations called the Gulf Coast Wedge. The first step began in October 2009 and was scheduled to inject CO_2 at rate of 1.65 million tons per year for 18 months into the lower Tuscaloosa Formation. The second step will inject at a rate of 137500~165000 tons of CO_2 per year for four years into the Paluxy Formation at a different site. CO_2 is supplied by a pilot unit capturing CO_2 from flue gas produced from a Southern Company power plant located near the injection sites [19].
- ADM GCS project (MGSC): The ADM GCS project is a SAGCS demonstration project that captures and sequestrates 1 million tons of CO_2 per year from an existing ethanol plant. The storage site is located at Decatur, Illinois. The target geological formation of the ADM GCS is the Mt. Simon sandstone, a well-characterized saline reservoir located about one mile beneath the surface. Figure 1.10 shows some key locations of the ADM GCS project [20].

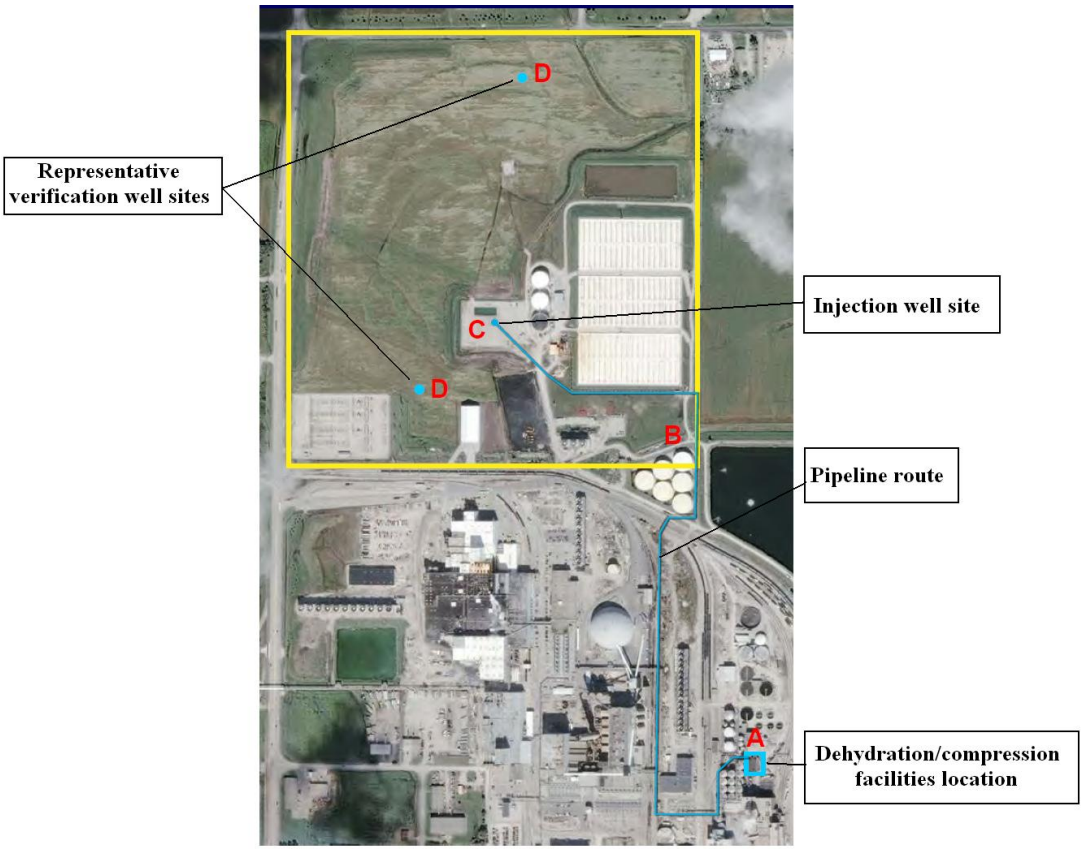

Figure 1.10 Facility locations of the ADM GCS project [20]

In addition to the three demonstration SAGCS project mentioned above, some smaller scale demonstration projects have also been proposed and are currently under evaluations, such as the Shallow Carbon Sequestration Demonstration Project at Springfield, Missouri [21], and the FutureGen 2.0 project proposed for an upgraded zero-emission power plant at Meredosia, Illinois [22].

Chapter 2

Governing Equations and Numerical Formulation

The large spatial extent of the order of kilometers and time duration of the order centuries of CO_2 plume migration after injection makes the study of SAGCS very different for laboratory scale experiment and costly using field tests. However numerical simulations using computation fluid dynamics (CFD) technology can be employed to determine the fate of injected CO_2 in a reservoir. With the development over four decades, CFD technology has now become mature and has been widely and successfully applied to various engineering problems. With the proper modeling of the storage formation and ground water transportation, CFD is capable of providing accurate enough analysis for quick estimation of reservoir performance at considerably lower cost.

In a complex simulation like that of SAGCS, it is impractical to integrate all geophysical and geochemical effects into one single model while retaining acceptable computational efficiency. Therefore, careful examination of physical phenomenon of interest in SAGCS is essential to determine simplifications in modeling of features of interest.

Another important benefit of numerical simulations is that one can investigates the effect of various injection parameters such as injection rate, injection duration, and injection well orientation and displacement on CO_2 storage efficiency and plume migration in a given reservoir. The advantage of numerical simulations makes it possible to perform optimization studies of these injection parameters for achieving the highest possible storage efficiency and minimum plume migration. Such an optimization capability can aid in successful implementation of SAGCS on industrial scale.

2.1 Numerical Modeling Challenges

Saline aquifer carbon sequestration takes place in target aquifers over 800 m (sometimes up to several kilometers) below the ground surface. Referring to its phase diagram (Figure 2.1), the critical point of CO_2 is 7.38 MPa in pressure and 31.1 °C in temperature. Assuming conservative estimation of hydrostatic pressure gradient being 9.81 MPa/km and geothermal gradient being 25 °C/km, the in situ CO_2 for SAGCS will be in supercritical phase – a phase which possesses physical properties of a liquid but dynamically acts like a gas – under reservoir conditions. More specifically, the injected supercritical CO_2 will have liquid-like density and gas-like viscosity and diffusivity. Deep saline aquifers are originally filled with brine which is heavier than supercritical CO_2. Various minerals are also expected in any aquifer. Therefore, multi-phase multi-component flow transportation will occur in SAGCS, with possibly important geochemical reactions and complex phase behavior. A numerical model that captures all the details of these effects will not only be physically very complex, but also computationally very expensive. Even on super computers, one single simulation may run for weeks and even months; needless to say dozens of simulations will be needed to produce meaningful results.

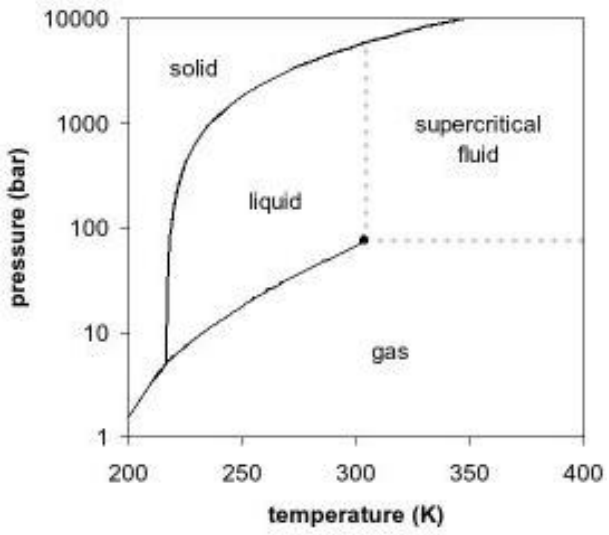

Figure 2.1 Phase diagram of CO_2

SAGCS involves physical processes that are relevant from nanometer to kilometers in special scales and a few milliseconds to hundreds of years in time scale. Therefore, it requires simplified but physically meaningful approaches to be proposed to make the numerical simulation of SAGCS process tractable. Spatial domain decomposition and time domain scaling of the multiphase flow governing equations are two practical approaches [23],[24]. The SAGCS problem to be studied must first be carefully examined and properly addressed to avoid ultimately ineffectiveness due to limitations in the scaling results and excessive computational demand due to the domain decomposition algorithms. In our work of numerical study of SAGCS, following philosophy is adapted: identifying the physical processes that are most critical to the analysis and optimization of the carbon sequestration problem up to a few decades since the inception of injection, and ignore all remaining processes. Such philosophy avoids putting excessive computing power on those minor effects while keeping simulation accuracy from being badly compromised for the phenomenon of interest.

Celia and Nordbotten's analysis on spatial and time scales, as shown in Figure 2.2 and Figure 2.3, serves as excellent roadmap to determine the dominant processes of interest for our research. As the first step to begin the analysis, it is preferred to describe what our research would like to address: numerical study and optimization of a complete carbon sequestration practice over a full-scale deep saline aquifer, i.e., numerical study and optimization of carbon sequestration over extensive spatial and time scales.

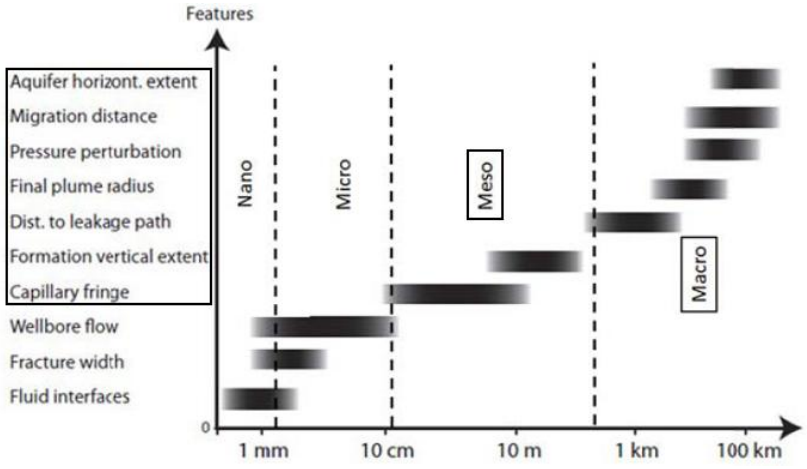

Figure 2.2 Space scale of different processes and features for GCS [23],[24]

Figure 2.2 depicts the dominant process and features for SAGCS with respect to different spatial scales. The spatial scale represents the characteristic length scale of a certain process, varying from nano-scale (order of sub-millimeters, for instance the fluid-fluid interfaces at the pore scale), to macro-scale (order of kilometers, for instance the lateral extent of the CO_2 plume). The black bars in Figure 2.2 indicate the dominant roles of various features. Figure 2.2 suggests that our research should focus on processes and features in the meso- and macro-scale regions, i.e., capillary fringe, formation vertical extent, distance to leakage path, final plume radius, pressure perturbation, migration distance, and aquifer horizontal extent. Such spatial scales and the dominant process and features are highlighted with solid boxes. It should be noted that it is still not practical to model all dominant processes and features even for each spatial scale. The final model should be further simplified on a case-to-case base to focus on the most dominant one or two process(es) and feature(s).

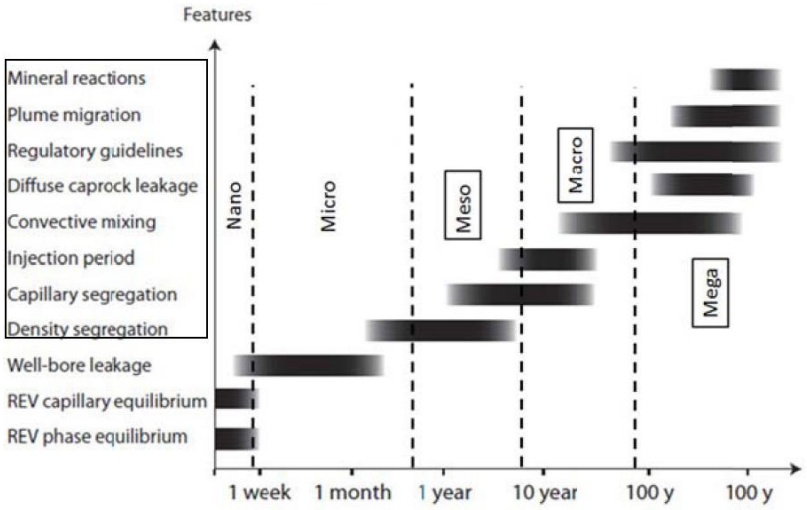

Figure 2.3 Time scale of different processes and features for GCS [23],[24]

Time scale also plays a crucial role in SAGCS process, since the dominant trapping mechanisms alter as time evolves. Such shift of dominant process and features in SAGCS with respect to time scales is illustrated in Figure 2.3. In Figure 2.3, time scale varies from nano-scale (order of seconds or smaller, for instance the dynamics of fluid-fluid interfaces at the pore scale and partitioning of components among phases at the

pore scale) through meso-scale (order of years, for instance the density segregation and capillary segregation) to mega-scale (order of centuries and larger, for instance the unstable gravity-driven miscible mixing of dissolved CO_2 in the bulk brine and long-term mineral reactions). Similar to Figure 2.2, the black bars in Figure 2.3 also represent the dominant roles of various processes and features. Figure 2.3 suggests that our research should focus on the processes and features in late micro-, meso-, macro-, and early mega-scale regions, i.e., density segregation, capillary segregation, injection period, convective mixing, diffuse caprock leakage, regulatory guideline, plume migration, and mineral reaction. Such time scales and the dominant processes and features are highlighted with solid boxes. Similarly to spatial scale analysis, the final model should be further simplified on a case-to-case base to focus on the most dominant one or two process(es) and feature(s).

With the help of analysis from Figure 2.2 and Figure 2.3 , the essential processes and features to be considered in our modeling and simulation become clear. A model that describes a saline aquifer with kilometer-scale horizontal extension and is capable to simulate up to several hundred years of simulation time should be established. The dominant processes to be investigated will be the lateral extension of CO_2 plume migration, pressure perturbation, segregation due to density difference and capillary pressure, and CO_2 dissolution into ambient porewater. Other processes, such as mineral reaction and phase interface interaction, can be excluded from the modeling for the time-being without introducing significant error. The completion of this analysis provides guidelines to obtain CFD solvers that are capable to meet our research demand.

The CFD solver used in this research to perform the numerical modeling and simulation is the second version of Transport of Unsaturated Groundwater and Heat (TOUGH2). TOUGH2 is a multi-dimensional numerical model of simulating the coupled transport of water, vapor, non-condensable gas, and heat in porous and fractured media [25],[26]. The Earth Sciences Division of Lawrence Berkeley National Laboratory, DOE, developed it for the applications of geothermal reservoir engineering, nuclear waste disposal, unsaturated zone hydrology, and geologic sequestration of CO_2. Detailed descriptions of TOUGH2 are discussed in Section 2.4.

The original TOUGH2 does not include any type of optimization ability. Therefore, an optimization module is to be developed and integrated into TOUGH2 as part of this research work. Based on our previous experience, genetic algorithm (GA) is chosen as the optimization technique. The successful implementation of GA optimizer makes the new solver-optimizer integrated code, identified as GA-TOUGH2, capable to perform optimization studies of much broader topics in geological carbon sequestration. Following sections will describe the detailed technical approaches used in numerical simulation and GA optimization. .

2.2 Governing Equations for Underground Multiphase Fluid Dynamics

Considering geophysical processes only, the basic governing equations of mass- and energy-balance for the multi-phase multi-component system can be written in the general form as:

$$\frac{d}{dt}\int_{V_n} M^\kappa dV_n = \int_{\Gamma_n} F^\kappa \cdot n d\Gamma_n + \int_{V_n} q^\kappa dV_n \qquad \text{(Eq. 1)}$$

where V_n is the control volume, an arbitrary sub-domain of the flow system under study. Γ_n is the closed surface that bounds the volume V_n. n is vector normal to the surface element on $d\Gamma_n$ pointing inward into V_n. The quantity M appearing in the accumulation term on LHS represents mass or energy per unit volume, with superscript κ labeling the components mass or energy equation. The quantity F in the advective term (first term on RHS) represents net mass or energy flux through the surface of control volume, and q in the source term (second term on RHS) represents any mass or energy source/sink within the control volume V_n. The explicit form of each of these terms is discussed in the following sections.

2.2.1 Mass Equation:

In the context of mass conservation, the details of Eq.1 can be expressed as follows.

For the LHS of Eq. 1, the general form of the mass accumulation term can be written as

$$M^{\kappa} = \phi \sum_{\beta} S_{\beta} \rho_{\beta} X_{\beta}^{\kappa} \qquad \text{(Eq. 2)}$$

where ϕ is the porosity of the media, S_β is the saturation of phase β, ϱ_β is the density of phase β, and $X_\beta^\varkappa$ is the mass fraction of component $\varkappa$ present in phase β.

The general form of the advective mass flux is a sum over phases, as written in Eq. 3.

$$F^{\kappa} = \sum_{\beta} X_{\beta}^{\kappa} F_{\beta} \qquad \text{(Eq. 3)}$$

The individual mass flux F_β for each phase is given by the multi-phase version of Darcy's law as

$$\begin{aligned} F_{\beta} = \rho_{\beta} \vec{u}_{\beta} &= \rho_{\beta} \left[-k \frac{k_{r\beta} \rho_{\beta} g}{\mu_{\beta}} \left(\nabla \frac{P_{\beta}}{\rho_{\beta} g} - \frac{\rho_{\beta} \vec{g}}{\rho_{\beta} g} \right) \right] \\ &= -k \frac{k_{r\beta} \rho_{\beta}}{\mu_{\beta}} \left(\nabla P_{\beta} - \rho_{\beta} \vec{g} \right) \end{aligned} \qquad \text{(Eq. 4)}$$

where u_β is the Darcy velocity in phase β, k is the absolute permeability, $k_{r\beta}$ is the relative permeability of phase β, μ_β is the viscosity of phase β, g is the gravitational acceleration vector, and P_β is the fluid pressure of phase β which is the sum of the pressure P of a reference phase (usually taken to be the gas phase) and the capillary pressure, given by

$$P_{\beta} = P + P_{c\beta} \qquad \text{(Eq. 5)}$$

Substituting Eq. 2~Eq. 5 into Eq. 1 results in the mass balance equation for multi-phase multi-component fluid system in porous media.

2.2.2 Energy Equation:

The energy balance equation is more complicated than the mass balance equation. For energy conservation, we have the general form of the heat accumulation term

$$M^{\kappa} = (1-\phi) \rho_R C_R T \qquad \text{(Eq. 6)}$$

where ϱ_R and C_R are the grain density and the specific heat of the rock respectively. T is the temperature and u_β is the specific internal energy in phase β.

The general form of the advective heat flux includes conductive and convective components, which are associated with the temperature gradient and fluid mass transportation respectively. This advective term can be modeled as

$$F^{\kappa} = -\lambda \nabla T + \phi \sum_{\beta} h_{\beta} F_{\beta} \qquad \text{(Eq. 7)}$$

where λ is the thermal conductivity and h_β is specific enthalpy in phase β. The first term in RHS of Eq. 7 is the conductive component and the second term is the convective component.

Substituting Eq. 6 ~ Eq. 7 into Eq. 1 results in the equation of energy for multi-phase multi-component fluid system in porous media.

2.2.3 Relative Permeability and Capillary Pressure Models:

Relative permeability and capillary pressure are important geological characteristics that require accurate models for accurate numerical description of the porous media multiphase fluid transportation phenomenon in porous media. Eight models of relative permeability and seven models of capillary pressure, all with respect to phase saturation, have been implemented in TOUGH2 [26]. For relative permeability, they are known as linear function, Corey's function (1954), Grant's function (1977), all phases perfectly mobile function, Fatt and Klikoff function (1959), van Genuchten-Mualem function (1976, 1980), and Verma et al. function (1985) models; for capillary pressure, they are known as linear function, Pickens et al. function (1979), TRUST function (1978), Milly's function (1982), Leverett's function (1941, 1985), and van Genuchten function (1980) models. Since the van Genuchten-Mualem functions for both relative permeability and capillary pressure are primarily used in this dissertation, they are given here.

van Genuchten-Mualem relative permeability model:

liquid relative permeability: $k_{rl} = \begin{cases} \sqrt{S^*}\left\{1-\left(1-[S^*]^{1/\lambda}\right)^{\lambda}\right\}^2 & \text{if } S_l < S_{ls} \\ 1 & \text{if } S_l \geq S_{ls} \end{cases}$ (Eq. 8)

gas relative permeability: $k_{rg} = \begin{cases} 1-k_{rl} & \text{if } S_{gr} = 0 \\ \left(1-\hat{S}\right)^2\left(1-\hat{S}^2\right) & \text{if } S_{gr} > 0 \end{cases}$ (Eq. 9)

subject to the restriction $0 \le k_{rl}, k_{rg} \le 1$, and

$$S^* = \left(S_l - S_{lr}\right) \Big/ \left(S_{ls} - S_{lr}\right), \quad \widehat{S} = \left(S_l - S_{lr}\right) \Big/ \left(1 - S_{lr} - S_{gr}\right) \qquad \text{(Eq. 10)}$$

In this relative permeability function, λ, S_{lr}, S_{ls}, S_{gr} are formation specific parameters.

van Genuchten-Mualem capillary pressure model is given by

$$P_{cap} = -P_0 \left([S^*]^{-1/\lambda} - 1 \right)^{1-\lambda} \qquad \text{(Eq. 11)}$$

subject to the restriction $-P_{max} \le P_{cap} \le 0$, and S^* is the same as defined in relative permeability function. In this capillary pressure function, λ, S_{lr}, S_{ls}, P_{max}, $1/P_0$ are formation specific parameters.

Other than Darcy flow, diffusion and hydrodynamic dispersion can also cause mass transportation. These processes can be described as follows.

$$F^{\kappa}_{dis} = -\sum_{\beta} \rho_{\beta} \bar{D}^{\kappa}_{\beta} \nabla X^{\kappa}_{\beta} \qquad \text{(Eq. 12)}$$

where $D_{\beta}^{\varkappa}$ is the hydrodynamic dispersion tensor given as

$$\bar{D}^{\kappa}_{\beta} = D^{\kappa}_{\beta,T} I + \frac{\left(D^{\kappa}_{\beta,L} - D^{\kappa}_{\beta,L}\right)}{u_{\beta}^{\,2}} u_{\beta} u_{\beta} \qquad \text{(Eq. 13)}$$

where

$$D^{\kappa}_{\beta,L} = \phi \tau_0 \tau_{\beta} d^{\kappa}_{\beta} + \alpha_{\beta,L} u_{\beta} \qquad D^{\kappa}_{\beta,T} = \phi \tau_0 \tau_{\beta} d^{\kappa}_{\beta} + \alpha_{\beta,T} u_{\beta} \qquad \text{(Eq. 14)}$$

are the longitudinal and transverse dispersion coefficients respectively. $D_{\beta k}$ is the molecular diffusion coefficient for component $\varkappa$ in phase β. τ_{β} is the tortuosity which includes a porous medium dependent factor τ_0 and a coefficient that depends on phase saturation S_{β}, $\tau_{\beta}=\tau_{\beta}(S_{\beta})$. a_L, a_T are the longitudinal and transverse dispersivities respectively. To simplify the equation, the hydrodynamic dispersion can be neglected in the context of carbon sequestration phenomena, while molecular diffusion should be retained. The mass flux from molecular diffusion alone is obtained by setting $a_L=a_T=0$ in Eq. 14; then the diffusive flux of component $\varkappa$ in phase b is given by

$$f^{\kappa}_{\beta} = -\phi \tau_0 \tau_{\beta} \rho_{\beta} d^{\kappa}_{\beta} \nabla X^{\kappa}_{\beta} \qquad \text{(Eq. 15)}$$

However, the mass transportation by diffusion is more dominant for the interaction of multiple components with the same phase. For instance, strong mass diffusion is

expected for enhanced gas recovery with carbon sequestration as both injected CO_2 and in situ methane are in gas phase. In contrast, a mass diffusion is likely to occur for SAGCS due to the distinct phases of injected CO_2 and pre-existing brine.

2.3 A Simple Analytical Solution for CO_2 Plume Migration

With proper assumptions, the very complicated in situ CO_2 migration process can be analytically described with reasonable accuracy. A simple analytical solution of the plume migration has been given by Bachu, Nordboten and Celia [27],[28],[29]. This simple analytical solution has been employed for validating the numerical simulations. It has also been extended in our work.

Consider an aquifer with constant thickness B, porosity Φ, and permeability k. An injection well fully penetrates the aquifer, and thus radial flow occurs. The schematic of this simple theoretical model is shown in Figure 2.4. To make the problem analytically tractable, the following simplifications and assumptions are made.

- Capillary pressure is assumed to be negligible comparing with other forces.
- Pressure is vertically averaged over the entire formation thickness. Therefore, the aquifer is in vertical equilibrium at any given time.
- Full saturation (Saturation = 1.0) is assumed in the respective regions occupied by each fluid, i.e., brine or CO_2, and a sharp interface is assumed between these two components.
- The density and viscosity of brine and CO_2 is assumed to be constant along the vertical direction and equal to the values that correspond to the in situ aquifer pressure and temperature.
- The variation of temperature with depth and CO_2 injection are neglected for the thickness of the aquifer. Therefore, the two-phase flow process is treated as isothermal.

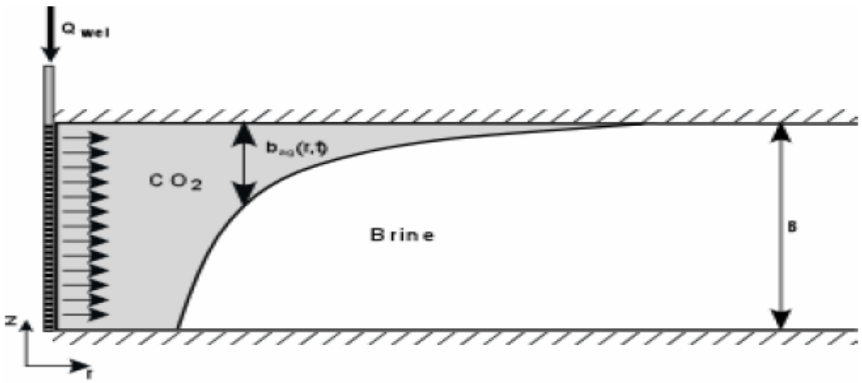

Figure 2.4 Analytical model for plume migration in a saline aquifer due to GCS

As shown in Figure 2.4, the location of the brine-CO_2 interface is a function of time and distance from the injection well. As a result, the pressure at the top of the aquifer (z=B) and bottom of the aquifer (z=0) can be related as

$$p(r,B) = p(r,0) - \rho_{ag} g b_{ag}(r) - \rho_b g[B - b_{ag}(r)] \qquad \text{(Eq. 16)}$$

where p is pressure, g is the gravitational constant, b_{ag} is plume thickness, r is distance (radius) from the injection well, and the subscripts ag and b stand for the injected CO_2 and brine respectively.

In addition, the flow flux rate of either fluid component is given by Darcy's law:

$$Q_i = -2\pi r b_i(r) \frac{k k_{ri}}{\mu_i} \frac{\partial p_i}{\partial r} \qquad \text{(Eq. 17)}$$

where $i = ag$ for CO_2, $i = b$ for brine, k_{ri} is the relative permeability of fluid i, b_i is the thickness of fluid i at location r, and Q_i is the flux of fluid i through a cylinder of radius r with the injection well in the center.

Since full saturation is assumed for each phase, we have $b_b + b_{ag} = B$, $k_{ri} = 1$, and conservation of total volume $Q_b + Q_{ag} = Q$, where Q is the volumetric CO_2 injection rate. Therefore, the change in thickness b_i for either fluid is given by the accumulation of that fluid in the cylindrical volume from the injection well to radius r according to:

$$\frac{\partial b_i}{\partial t} = -\frac{1}{2\pi\phi r} \frac{\partial}{\partial r}(r Q_i) \qquad \text{(Eq. 18)}$$

The Eq. 16, Eq. 17 and Eq. 18 form a system of equations with four unknowns: b_{ag}, Q_{ag}, $p(r,0)$ and $p(r,B)$. The solution can be sought based on the energy minimization and variational calculus principles, which say that the fluids in the system will arrange

themselves to minimize the amount of energy required to inject the given mass of fluid at any time. Two dimensionless variables are introduced in the calculation:

$$b' = \frac{b_{ag}}{B} \quad \text{and} \quad r' = r\sqrt{\frac{B\pi\phi}{V(t)}} \tag{Eq. 19}$$

where $V(t) = \int Q dt$ is the volume of the injected CO_2 since inception of injection.

Thus, the thickness of the plume of injected CO_2 is given by the solution of the resulting equation:

$$-\frac{\lambda - 1}{2r'\left[(\lambda - 1)b' + 1\right]^2} + \Gamma r' b' + \Lambda r' = 0 \tag{Eq. 20}$$

where Λ is the Lagrange multiplier defined by the solution of the following transcendental equation:

$$\Lambda(\lambda - 1)^2 - \Gamma(\lambda - 1) + \Gamma\lambda \ln\left(\frac{\Gamma + \Lambda}{\Lambda\lambda}\right) = \frac{2\lambda\left[\Lambda(\lambda - 1) - \Gamma\right]^2}{\lambda - 1} \tag{Eq. 21}$$

where λ is the mobility ratio defined as

$$\lambda = \mu_b \Big/ \mu_{ag} \tag{Eq. 22}$$

The dimensionless group in Eq. 20 and Eq. 21 represents the ratio of buoyant versus viscous and pressure forces and is given by

$$\Gamma = \frac{2\pi\Delta\rho g k k_{rb} B^2}{\mu_b Q} \tag{Eq. 23}$$

If Γ is greater than 0.5, the buoyant force will dominate; if Γ is smaller than 0.5, then the hydrodynamic force will dominate. Since in our study the involved CO_2 injection rate is fairly high, the buoyant force is negligible compared to the hydrodynamic force, i.e., Γ<0.5. In this situation, the solution provided by Eq. 21 is greatly simplified, resulting into the profile of the plume described by Eq. 24.

$$\frac{b_{ag}(r,t)}{B} = \frac{1}{\mu_b - \mu_{ag}}\left[\sqrt{\frac{\mu_b \mu_{ag} V(t)}{B\pi\phi r^2}} - \mu_{ag}\right] \tag{Eq. 24}$$

This simplified solution corresponds to the radial Buckley-Leverett solution [30]. It shows that while gravity acts to segregate the injected CO_2 at the top of the aquifer, the

dominant mechanism for energy loss is viscous dissipation, and Eq. 24 is a reasonable representation of the profile of the plume of injected CO_2. For the horizontal extent of the plume, setting $b_{ag}(r,t) = 0$ yields

$$R_{\max} = \sqrt{\frac{\mu_b V(t)}{\mu_{ag} B \pi \phi}} \qquad \text{(Eq. 25)}$$

Eq. 25 gives a quick and convenient means to estimate the maximum CO_2 plume migration when the detailed in situ flow pattern is not needed. It also serves as the theoretical baseline case in validating of CFD simulations as described in Chapter 3.

2.4 TOUGH2 - the Numerical Solver for Underground Multi-component and Multi-phase Fluid Flow

TOUGH2 is a general-purpose numerical simulation program for three-dimensional fluid and heat flows of multi-phase multi-component fluid mixtures in porous and fractured media. Major applications of TOUGH2 are in geothermal reservoir engineering, nuclear waste isolation studies, environmental assessment and remediation, and flow and transport in variably saturated media and aquifers.

The basic transport equations presented in Section 2.1 are used in TOUGH2 as governing equations. To discretize the continuous variables, TOUGH2 uses "integral finite difference" (IFD) method. The IFD encourages a "physical" view of model building, analogous to assembling a laboratory experiment. It provides a very simple conceptual basis for assigning boundary conditions, by viewing the flow system as a network of boxes that exchange mass and energy. The IFD introduces volume and area averages as follows

$$\begin{aligned} &\int_{V_n} M dV = V_n M_n \\ &\int_{\Gamma_n} \vec{F}^{\kappa} \cdot \vec{n} dV = \sum_m \int_{A_{nm}} \vec{F}^{\kappa} \cdot \vec{n} d\Gamma = \sum_m A_{nm} F_{nm} \end{aligned} \qquad \text{(Eq. 26)}$$

The discretization in IFD method corresponding to Eq. 26 is shown in Figure 2.5.

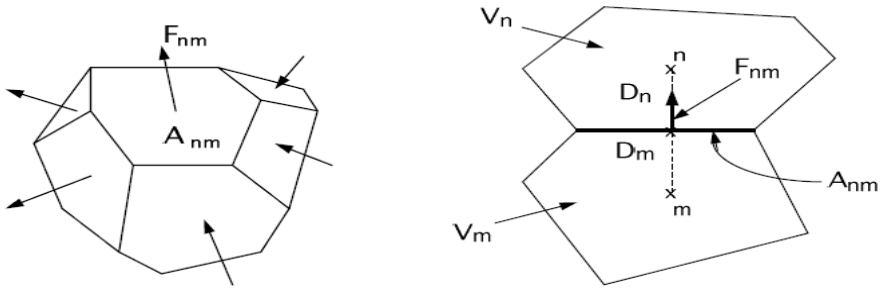

Figure 2.5 Space discretization and geometry in IFD method

More details of the IFD can be found in the TOUGH2 manual [25],[26].

2.5 Genetic Algorithm

Genetic Algorithm (GA) belongs to a class of optimization techniques that are inspired by the biological evolution [32],[32]. The algorithm begins with a set (identified as "generations") of vectors (identified as "individuals"). The individuals from one generation are used to create a new generation of individuals, which is supposed to be better than the previous generation. Individuals used to form the new individuals (identified as "offspring") for the succeeding generation are selected according to their function value of satisfying a certain criteria (identified as the "fitness function"). This process is repeated, creating the best individuals for each successive generation according to certain pre-defined criteria. Finally a generation of individuals is obtained where all the individuals in that generation produce the optimal values of the fitness function within a small tolerance; the algorithm is then considered to have achieved convergence. Implementation details of GA are described below.

1) *Initialization*: *k* individuals are randomly generated to serve as the starting generation. Each individual is consisted of *n* alleles as shown in Figure 2.6.

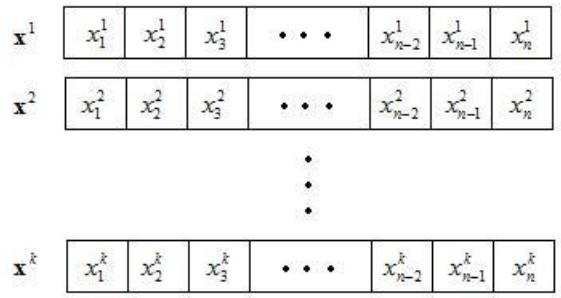

Figure 2.6 Individuals' initialization in GA

2) *Get Fitness*: Fitness function value of each individual in the generation is evaluated. The fitness function is the mathematical description of the optimization objectives, as given in Eq. 27.

$$f^k = function\left(x_1^k, x_2^k, x_3^k \cdots x_{n-2}^k, x_{n-1}^k, x_n^k\right) \qquad \text{(Eq. 27)}$$

3) *Advance Generation*: A new generation with potentially higher fitness function values is obtained by repeating the following steps:

a) *Natural Selection*: Individuals with undesired fitness function values are eliminated from the current generation. The remaining individuals in the generation (identified as "survivors") are retained with acceptable fitness function value. This process is shown schematically in Figure 2.7.

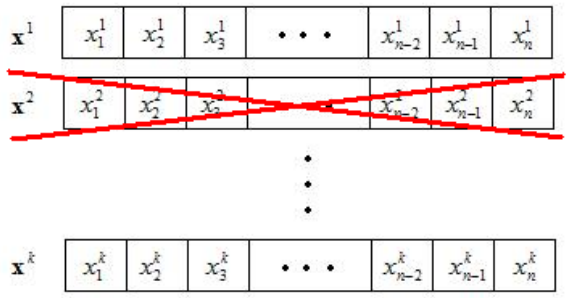

Figure 2.7 Natural selection of individuals in GA

b) *Crossover*: Using the Fitness Proportionate Selection (FPS) technique, a pair of individuals from the survivors is picked up as the "parents". The FPS is a

widely used operator for selecting potentially useful solutions for recombination and can be described as

$$p_i = \frac{f_i}{\sum_{j=1}^{n} f_j} \qquad \text{(Eq. 28)}$$

where p_i is the possibility of the i_{th} individual being chosen as a parent, f_i is the fitness value of the i_{th} individual.

As chosen for reproduction, the parents crossover with each other and generate a new individual (identified as "offspring"). The process of crossover is shown schematically in Figure 2.8. By crossover, information obtained from the parents is exchanged and passed along to the offspring.

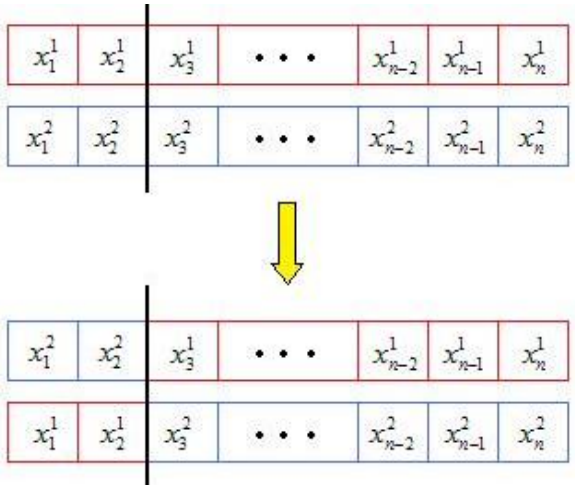

Figure 2.8 Crossover of survivors in GA

c) *Inclusion*: The newly generated offspring is included in the existing generation as a new individual.

d) *Loop*: Steps b) and c) are repeated until a new generation is obtained, i.e., all the eliminated individuals in step a) are replaced by offspring.

e) *Mutation*: In the new generation, individuals are randomly selected for mutation, i.e., change in its input variables without preserving information from the parents. The process of mutation is shown schematically in Figure 2.9. It is crucial to ensure that the solution jumps out of the local optima.

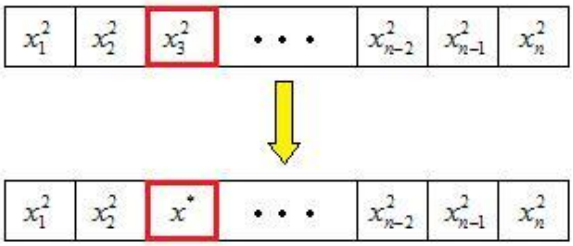

Figure 2.9 Mutation perturbs one selected allele in GA

4) *Replacement*: The old generation in step 1) is replaced by the new generation obtained from step 3). Each individual in the new generation is again evaluated for its fitness function value.

5) *Convergence Check*: Steps 1) to 4) are repeated until the convergence is achieved, i.e. a generation of individuals is obtained where all the individuals in that generation produce the optimal value of the fitness function within a small prescribed tolerance.

Steps 1) to 5) summarizes the general procedure of GA. Details need to be elaborated and GA parameters need to be tweaked for smooth and robust optimization.

2.6 GA-TOUGH2 Integrated Program

To realize the capability of numerical simulation and optimization for SAGCS, the GA optimizer is implemented into the TOUGH2 solver to obtain a simulation-optimization integrated computer program. Additional modules for pre- and post-simulation process are introduced to enable the data sharing between GA and TOUGH2. A schematic of the program architecture and data flow is presented in Figure 2.10.

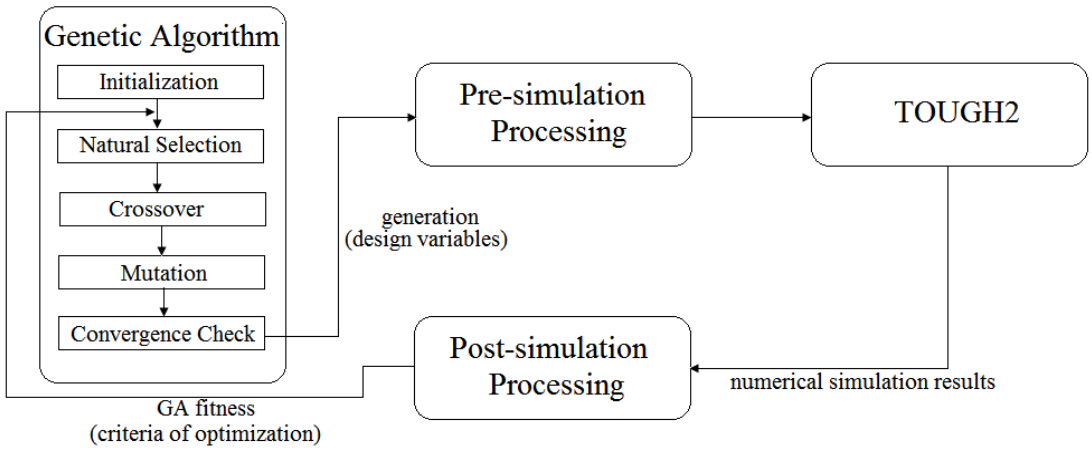

Figure 2.10 Schematic of GA-TOUGH2 integrated code

Up to this point, no specific optimization parameter or fitness function is defined. This is a result of the great effort put into the flexible development of GA-TOUGH2. To enable the potential of versatile applications on geological carbon sequestration, GA-TOUGH2 has been developed in a modular fashion. It offers a general platform that can perform optimization studies on various possible topics with relatively easy modifications of the code. As three examples of SAGCS optimizations, numerical optimization studies of 1) water-alternating-gas injection (WAG) technique for optimal CO_2 migration reduction; 2) time-dependent injection design for optimal injection pressure management; and 3) optimal injection distribution design for a multi-well injection system are conducted in this dissertation in Chapter 5.

Chapter 3

TOUGH2 Code Validation Using Analytical and Benchmark Solutions

TOUGH2 was installed on one of the machines in the CFD lab in the department of Mechanical Engineering & Materials Science at Washington University in St Louis. Since it was the first time that computer program was used in the CFD lab, a number of code validation cases were conducted. TOUGH2 was installed on a Dell Precision T7400 workstation with 8-core Intel Xeon X5450 CPUs @ 3.00 GHz, 8 GB RAM and Windows XP 64-bit operating system. This workstation is computationally powerful enough for the simulations conducted to accomplish the research objective of this dissertation.

TOUGH2 is available as source files written in Fortran77. TOUGH2 does not provide graphical user interface (GUI) of any kind. All its input files and output results are in ASCII format. TOUGH2 has very high computing efficiency when executing the large scale simulations, and it is very convenient for users to make modifications to the source code if needed. However, both the problem setup and result analysis capability in TOUGH2, such as mesh generation and contour map visualization, are not as comprehensive or straightforward as available in some newer commercial multiphase flow filed simulators. For any complex problem, the modeling process tends to be tedious and error-prone. To address such deficiency, a third-party GUI for TOUGH2 named PetraSim was also installed on the same machine with TOUGH2. PetraSim preserves the original TOUGH2 binary files to execute simulations, while providing a smooth interface for user-friendly computing environment. However, PetraSim in its

original form lacks the compatibility for integrating a new optimization module and some recently developed equation-of-state modules.

Previous validation simulations on benchmark problems have shown that the simulation results obtained by TOUGH2 and PetraSim are identical [33][34]. For our code validation purpose, we have employed three widely used benchmark problems by GCS researchers worldwide. Simulations were conducted by both TOUGH2 and PetraSim. These three benchmark problems were first defined in the Workshop on Numerical Models for Carbon Dioxide Storage in Geological Formations at the University of Stuttgart, Germany [35],[36],[37],[38],[39]. We study the benchmark problem #1 and #3 using PetraSim, while benchmark problem #2 is simulated using the original version of TOUGH2 because of limit on the availability of needed equation-of-state module in PetraSim. When simulation is performed using TOUGH2, necessary post-processing programs such as Tecplot are employed used for visualization and analysis.

3.1 Simulation of in situ CO_2 Migration and Comparison with Analytical Solution

As a first step towards code validation, simulations for CO_2 plume migration in an ideal simplified reservoir is performed; the analytical solution for this case is available (Eq. 24 in Chapter 2) and is obtained as:

$$\frac{b_{ag}(r,t)}{B} = \frac{1}{\mu_b - \mu_{ag}} \left[\sqrt{\frac{\mu_b \mu_{ag} V(t)}{B\pi\phi r^2}} - \mu_{ag} \right] \qquad \text{(Eq. 29)}$$

where t is the time lapsed since the inception of injection, r is the distance (radius) from the injection well, $b_{ag}(r,t)$ is the plume thickness as a function of r and t, B is the total thickness of the reservoir, φ is the porosity of the reservoir, μ is the dynamic viscosity, subscripts ag and b stand for the injected CO_2 and brine respectively, and $V(t) = \int Q dt$ is the volume of the injected CO_2 within time t.

For the horizontal reservoir, setting $b_{ag}(r,t) = 0$ yields Eq. 25 of Chapter 2, which gives a quick evaluation of the maximum CO_2 plume migration as:

$$R_{\max} = \sqrt{\frac{\mu_b V(t)}{\mu_{ag} B \pi \phi}} \qquad \text{(Eq. 30)}$$

In numerical simulations, a hypothetical deep saline reservoir of thickness of 100 m is assumed. A cylindrical computational domain is considered as shown in Figure 3.1. Generic hydrogeological properties are used. CO_2 injection rate is set at 1 kg per year for ten years. Detailed model parameters used in the simulations are summarized in Table 3.1. CO_2 plume migration at each year is computed by the simulation and compared with the analytical solution given by Eq. 29.

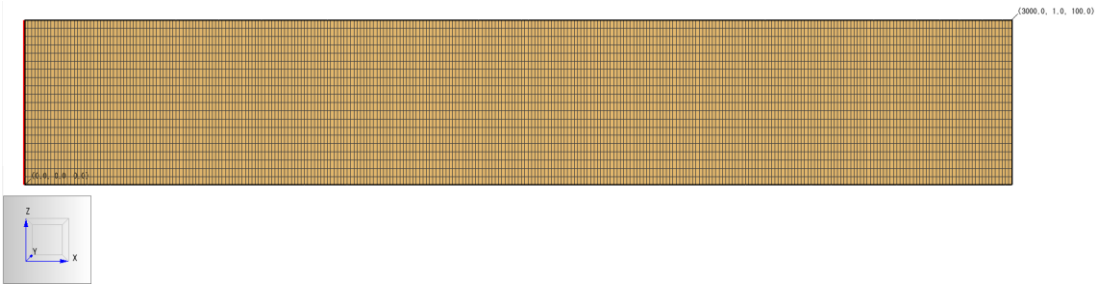

Figure 3.1 Computational domain and mesh of a generic cylindrical aquifer

Table 3.1. Geometry parameters and hydrogeological properties of the generic saline aquifer

Geometry	100 m in thickness; 3000 m in radius
Permeability	1.0×10^{-13} Darcy, isotropic
Porosity	0.3
Temperature	20 °C
Pressure	10 bar
CO_2 density	789.96 kg/m^3
CO_2 viscosity	0.0000712905 Pa·s
Brine density	1029.69 kg/m^3
Brine viscosity	0.001488427 Pa·s
Relative permeability	linear
Brine residual saturation	0
CO_2 residual saturation	0
Capillary pressure	none
Injection rate	1 kg/s
Boundary condition	Open boundary
Domain discretization	300 × 20

The simulation time is ten years and CO_2 migration within the aquifer is computed for each of the ten years. In Figure 3.2, CO_2 plume at 1st, 4th, 7th, and 10th year since the inception of injection is shown.

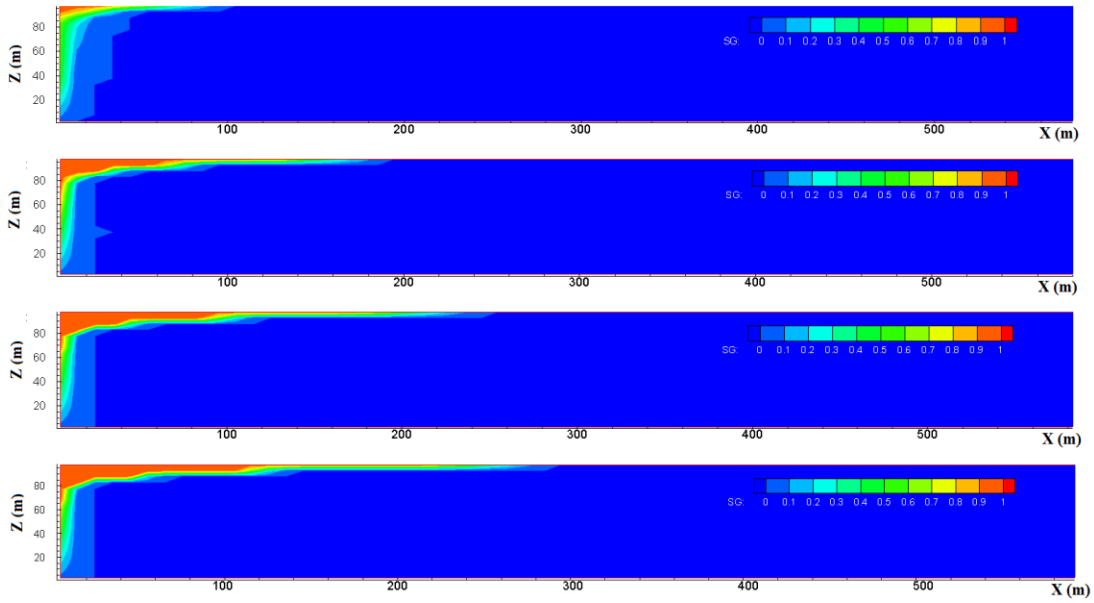

Figure 3.2 CO_2 plume at 1st, 4th, 7th, and 10th year of injection

As seen in Figure 3.2, the injected CO_2 migrates upwards very rapidly and then prominently migrates underneath the caprock. A typical plume shape is already identifiable after one year of injection, when the farthest CO_2 migration reaches about 100 m from the injection well. In the following 9 years, in situ CO_2 keeps migrating outwards and spreads to a prominent 300 m after the 10th year of injection. Physically, such a large radial migration of in situ CO_2 is caused by the gravity separation. Utilizing Eq. 30, the horizontal extent of the plume can be analytically calculated. Taking the necessary values of reservoir and fluid properties from Table 3.1 the horizontal extent of the plume predicted by Eq. 30 for the first 10 years since injection is summarized in Table 3.2. The horizontal extent of the plume given by TOUGH2 simulations is also summarized in Table 3.2 for comparison with the analytical solution.

Table 3.2 Maximum CO_2 migration underneath the caprock given by the analytical solution and TOUGH2 simulation

	Maximum Migration based on Simulation (A)	Maximum Migration based on Analytic solution (B)	Deviation based on analytic solution (A-B)
Year 1	100.75 m	95.58 m	0.054090814
Year 2	140.49 m	135.17 m	0.039357846
Year 3	168.37 m	165.55 m	0.017034129
Year 4	191.34 m	191.16 m	0.00094162

Year 5	211.27 m	213.72 m	-0.011463597
Year 6	229.23 m	234.12 m	-0.020886725
Year 7	235.34 m	252.88 m	-0.069360962
Year 8	260.81 m	270.34 m	-0.035251905
Year 9	275.70 m	286.74 m	-0.038501779
Year 10	289.36 m	302.25 m	-0.042646816

As shown in Table 3.2, TOUGH2 simulations successfully predict the maximum CO_2 plume migration underneath the caprock with excellent agreement with the analytic solutions given by Bachu, Nordbotten and Celia [27],[28],[29]. The insignificant difference between the numerical and analytical solutions can be explained by the fact that CO_2 dissolution is accounted for in TOUGH2, which is neglected in the derivation of the analytical solution. Since CO_2 dissolution is governed by the contact area between CO_2 and the ambient brine, it is expected that the rate of CO_2 dissolution into brine will gradually increase over time as larger contact area becomes available due to the development of CO_2 plume. Nevertheless, Table 3.2 validates TOUGH2 as an accurate simulation tool for predicting the migration of in situ CO_2.

3.2 Simulation of Benchmark Problem #1 - CO_2 Plume Evolution and Leakage through an Abandoned Well

A three-layered formation is modeled for the first benchmark problem [27]. CO_2 is injected into the deeper aquifer, shown schematically in Figure 3.3. It spreads in the aquifer and then rises up to a shallower aquifer upon reaching a leaky well. A quantification of the leakage rate, which depends on CO_2 plume evolution and the pressure buildup in the aquifer, is the main objective of this benchmark simulation. Figure 3.3 shows the schematic of the problem description by providing a cross-section of the formation.

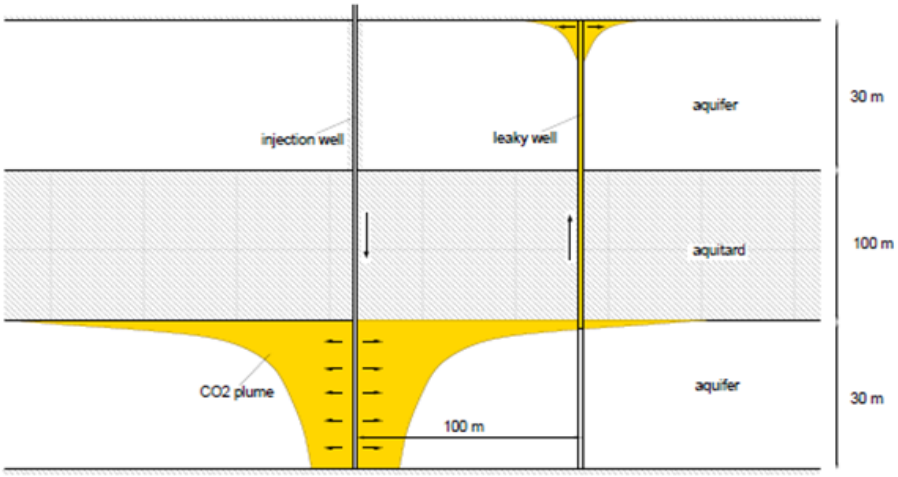

Figure 3.3 Schematic of benchmark problems #1 (cross-sectional view) [36]

The three layers in Figure 3.3 are identified as one aquitard layer and two (saline) aquifer layers. The lower aquifer layer is assumed to be 3000 m below the ground surface. Typical saline aquifer conditions and hydrogeological properties, such as temperature, salinity, permeability, are assigned to the aquifer layers. The aquitard is assumed to be impermeable to both saline and CO_2, it is considered as an ideal geological seal to flow transportation. An "abandoned well" fully penetrating the three layers is located 100 m away from the CO_2 injection well. It can be either a crack in the formation or a physical abandoned well, which served as a pathway for upward CO_2 migration.

Supercritical CO_2 is injected only into the lower aquifer through the injection well. Being less dense than brine, injected supercritical CO_2 gradually migrates to the ceiling of the lower aquifer and forms a plume. The formation and migration of the plume depends upon the geometric and hydrogeological properties of the aquifer.

Table 3.3 summarizes the geometric properties of the aquifer in benchmark problem #1. It should be noted that the actual geometry of the injection well and abandoned well is circular with a radius of 0.15 m. Since the use of an unstructured grid is not supported by PetraSim, an approximation to the circular geometry is made. Maintaining an identical cross-sectional area, the original circular injection well and the leaky well are replaced by wells of square cross-section with dimension of 0.266 m × 0.266 m. Such an approximation is acceptable since the details of the flow pattern inside the wells are not critical in achieving the objective of this simulation.

Table 3.3 Geometry parameters for benchmark problem #1

Domain dimension	1000 m × 1000 m × 160 m
Aquifer depth	2840 m ~ 3000 m
Aquifer thickness	30 m
Aquitard thickness	100 m
Distance between injection well and leaky well	100 m
Injection & leaky well geometry	0.266 m × 0.266 m

Figure 3.4 shows the simulation domain and the structured mesh inside the domain.

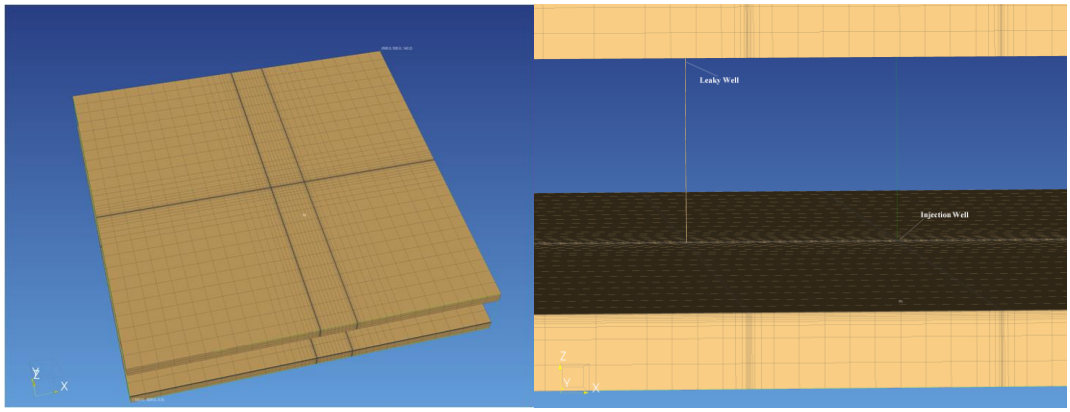

Figure 3.4 Entire computational domain (left) and the zoomed-in-view (right) for benchmark problem #1

To accurately model the small dimensions of the wells and to accurately capture the CO_2 leakage rate, mesh is highly refined in the neighborhood of the injection and leakage wells, as can be seen in the zoomed-in-view in Figure 3.4. Since high CO_2 concentration is expected at the ceiling of the lower aquifer due to gravity segregation, the mesh in this part of the lower aquifer is also refined. The mesh in the upper aquifer is not refined since it does not affect the accuracy of simulations but results in less computational efforts. The upper aquifer is uniformly discretized with vertical discretization length of 10 m, since it is assumed that the leakage amount is small and the shape of leakage plume is not of great interest. By establishing the simulation

domain and the mesh in this manner, reasonably accurate results are obtained while keeping the computational effort relatively low.

The hydrogeological properties of the simulation domain are summarized in Table 3.4.

Table 3.4 Hydrogeological parameters for benchmark problem #1

Aquifer permeability	2.0×10^{-14} m^2
Leaky path permeability	1.0×10^{-12} m^2
Porosity	0.15
Residual brine saturation	0.2
Residual CO_2 saturation	0.05
Relative permeability	linear ($k_r = S$)
Capillary pressure	Brooks-Corey
Entry pressure	1.0×10^5 Pa
Brooks-Corey parameter	2.0

Other simulation parameters such as initial conditions and boundary conditions are summarized in Table 3.5.

Table 3.5 Simulation parameters for benchmark problem #1

Thermal condition	Isothermal
Initial condition (Temperature)	Geothermal gradient: 0.03 K/m, Initial value at 800 m: 34 ^{o}C
Initial condition (Pressure)	Pressure gradient: 1045 Pa/m, 3.086×10^7 Pa at 3000 m depth
Boundary condition	Fixed-state on lateral boundaries No mass flow on top and bottom boundaries
Initial CO_2 mass fraction	X_{CO2}=0
Initial salt mass fraction	X_{sm}=0.20
Injection rate	8.87 kg/s
Simulation end time	1000 days

With properties and parameters summarized above, the numerical model of benchmark problem #1 is setup in PetraSim. A pre-injection simulation is carried out first with no injection of CO_2 to achieve equilibrium condition under gravity. The equilibrium state is

then implemented as an initial condition for the subsequent simulation with CO_2 injection. The equilibrium simulation is critical to provide the simulation with CO_2 injection with realistic initial condition; this is a prerequisite procedure for all the simulations reported in this dissertation. For this benchmark problem, it takes about five minutes of CPU time on the workstation for the simulation to complete. The leakage flux, pressure perturbation, and CO_2 saturation distribution throughout the aquifer after 80 days of CO_2 injection are examined and compared with the simulations of other investigators [39]. The leakage flux is a non-dimensional quantity defined as the ratio of CO_2 leakage rate to CO_2 injection rate. Detailed comparisons using various simulation codes are shown in Figure 3.5, Figure 3.6 and Figure 3.7, and are summarized in Table 3.6.

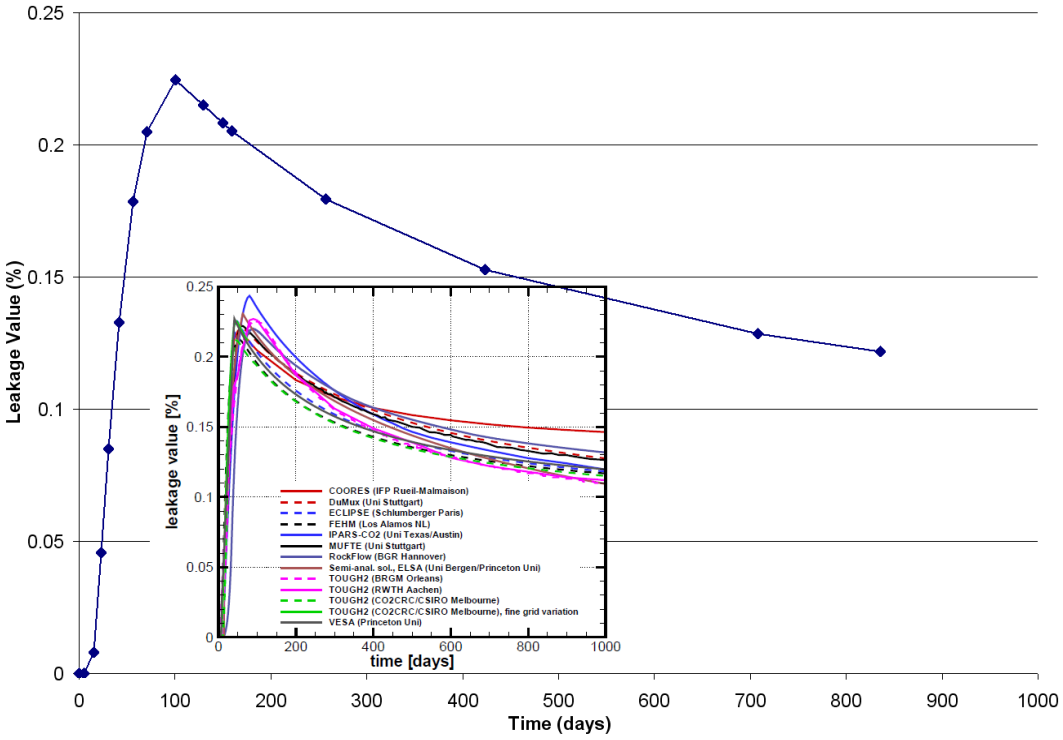

Figure 3.5 CO_2 leakage flux value obtained with WUSTL-TOUGH2 and other simulation codes

In Figure 3.5, our result (WUSTL-TOUGH2) is shown by the large graph, while comparisons with other simulation codes are shown in the inner box.

Table 3.6 Simulation results and comparisons for benchmark problem #1

	Max. Leakage	Time at max. leakage	Leakage at 1000 days	Arrival time
TOUGH2 (WUSTL)	0.225 %	100 days	0.115 %	11 days
TOUGH2 (BRGM)	0.226 %	93 days	0.110 %	4 days
TOUGH2 (Aachen)	0.227 %	89 days	0.112 %	9 days
MUFTE (U. Stuttgart)	0.222 %	58 days	0.126 %	8 days

As additional comparisons, the pressure perturbation and CO_2 saturation distribution after 80 days of injection is also computed and compared with those from the MUFTE numerical solver [39]. Excellent agreement is obtained as shown in Figure 3.6 and Figure 3.7.

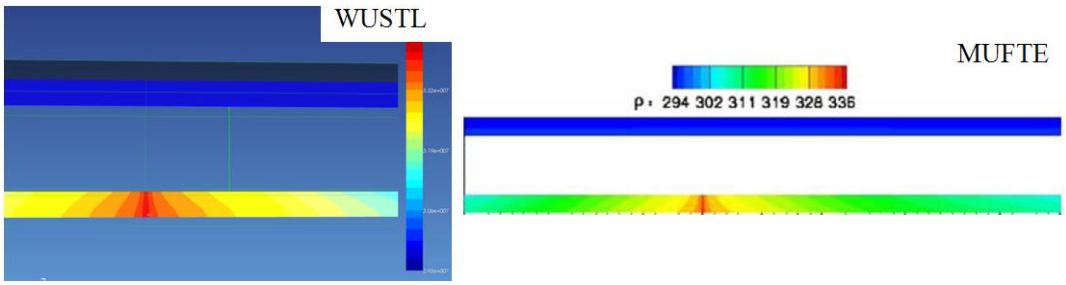

Figure 3.6 Pressure perturbation within the aquifer after 80 days of injection (left: WUSTL-TOUGH2; right: MUFTE)

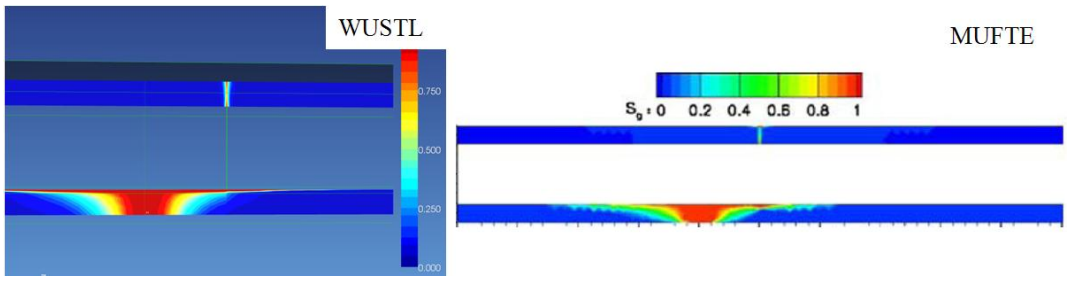

Figure 3.7 CO_2 distribution within the aquifer after 80 days of injection (left: WUSTL-TOUGH2; right: MUFTE)

As seen in Figure 3.7, CO_2 plume is nicely captured in the simulation. A schematic of the CO_2 plume flow is shown in Figure 3.8. Although based on a simplified analytical

model, Figure 3.8 shows in situ CO_2 migration due to the combined pressure-driven Darcy flow and the buoyancy-drive CO_2 transport. With the injection well located on the left side of Figure 3.8, CO_2 plume can be identified as consisting of two distinct regions. The first region is a smaller region on the left adjacent to the injection well, marked as region (1) in Figure 3.8. In this region CO_2 is distributed uniformly through the entire period of the injection interval. This implies strong hydrodynamic force caused by the pressure difference between the pressurized injection well and the un-affected aquifer. Within this region, lateral pressure gradient dominates the movement of CO_2 and Darcy flow occurs, causing CO_2 to migrate more radially through the aquifer. The second region is marked as region (2) in Figure 3.8 where CO_2 plume fully develops. In this region, buoyancy due to the density difference between CO_2 and brine becomes dominant and drives the upward movement of CO_2 along with lateral migration. In this region, the vertical movement of CO_2 becomes dominant and results into plume flow. Being the phenomena of fundamental concern in SAGCS, understanding the development of plume flow is critical for the success of SAGCS. The size of the two regions in Figure 3.8 may vary depending upon the properties of the actual aquifer, but under most conditions region (2) becomes dominant in size, which influences the safety and efficiency of SAGCS operations. Therefore, every effort should be made to either increase the size of region (1) or decrease the size of region (2) for successful and desirable implementation of SAGCS.

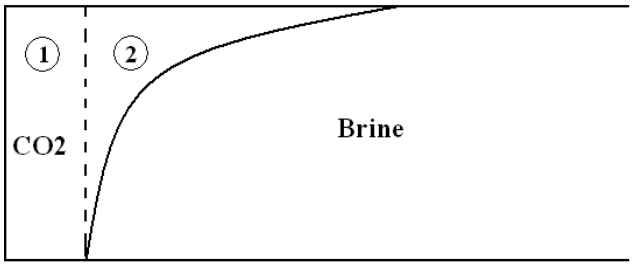

Figure 3.8 Schematic of the shape of in situ CO_2 plume

The simulation of benchmark problem #1 is very instructive. Three conclusions can be made. 1) small variations among the results from different numerical simulators with different users are un-avoidable. Such variations are expected because some parameters

are intentionally left un-specified; 2) our results are in satisfactory agreement with the results of other investigators; and 3) the most important CO_2 behavior under reservoir condition, i.e. the plume flow is well captured and understood by the simulations. This simulation and others for benchmark problem #2 and #3 nor only validate our numerical solver but also provide insights needed for optimization studies reported in Chapter 5.

3.2 Simulation of Benchmark Problem #2 - Enhanced CH_4 Recovery in Combination with CO_2 Sequestration in Depleted Gas Reservoirs

For decades, oil and gas industry has been using a reservoir engineering technique to increase the oil/gas production from matured reservoirs, known as the enhanced oil/gas recovery (EOR/EGR). As the original formation fluid (oil or natural gas) gets extracted, pressure in the reservoir gradually decreases. Such de-pressurization process makes it increasing difficult to maintain the desired production rate. The reservoir needs to be re-pressurized to mitigate the drop of oil/gas production. One of the means to do this is to inject CO_2 into the matured reservoir. With void space being occupied by the injected CO_2, remaining oil/gas is pushed out of the reservoir. Meanwhile, the depleted reservoir becomes an ideal carbon sink for long-term storage. EOR/EGR with CO_2 sequestration, also known as CSEOR/CSEGR, has been frequently used by the industry due to its strong economic merits.

In benchmark problem #2, a five-spot pattern domain is considered for modeling. The five-spot pattern is a common configuration for oil/gas production. A schematic of the reservoir is shown in Figure 3.9.

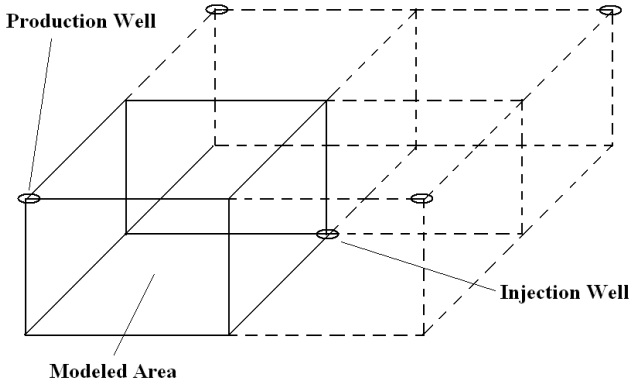

Figure 3.9 Schematic of the 3-D five-spot pattern for benchmark problem #2

Natural gas is produced at the four upper corners of the reservoir, while CO_2 is injected in the middle of the domain at the bottom-most part. This is a direct result of CO_2 being heavier than CH_4 under the reservoir conditions. Injection of CO_2 at the bottom avoids gas mixing and creates better sweep efficiency. The main goal of this benchmark simulation is to identify the gas recovery factor, defined as the ratio of enhanced CH_4 production to the original remaining CH_4 amount until the shutdown of production well. Additionally, the time to shut down the production, which is defined as the time when the production contains up to 20% of CO_2 by mass, needs to be determined.

Due to symmetry only a quarter of the domain is modeled, as shown in Figure 3.9 as the volume bounded by the solid lines. Table 3.7 gives the geometry parameters. Due to relatively strong diffusion, discretization length has strong influence on the gas mixing [37]. It is therefore strictly specified as 4.572 m for both vertical and horizontal direction.

Table 3.7 Geometry parameters of the domain for benchmark problem #2

Quarter model of five-spot pattern	201.19 m × 201.19 m
Thickness	45.72 m
Discretization length	4.572 m

Figure 3.10 shows the CFD model and its mesh of the quarter five-spot reservoir.

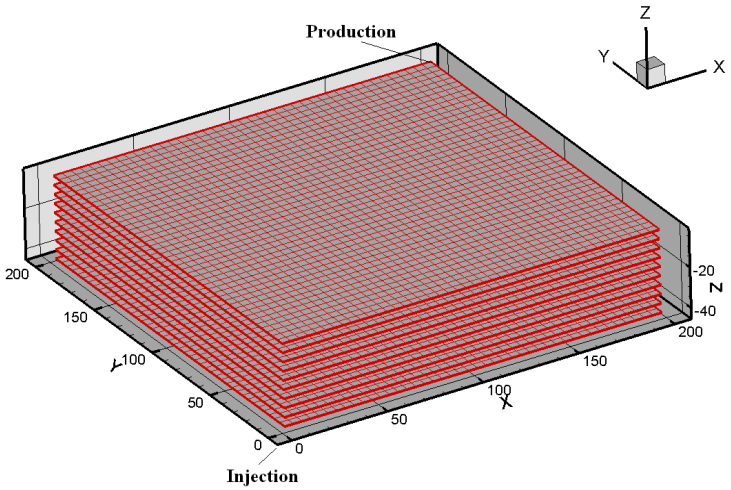

Figure 3.10 CFD model and its mesh in the quarter 5-spot domain for benchmark problem #2

The hydrogeological properties assigned to the model are summarized in Table 3.8.

Table 3.8 Hydrogeological properties of the domain for benchmark problem #2

Permeability	Horizontal: 50×10^{-15} m^2, Vertical: 5×10^{-15} m^2
Porosity	0.23
Residual brine saturation	0
Relative permeability	Liquid: Immobile, Gas: Linear ($k_r = S$)
Capillary pressure	Not considered

Initial conditions and boundary conditions and some other parameters of the domain are given in Table 3.9.

Table 3.9 Simulation parameters for benchmark problem #2

Thermal condition	Isothermal
Initial condition (Temperature)	66.7 ^{o}C
Initial condition (Pressure)	3.55×10^{6} Pa
Boundary conditions	No mass flow at all boundaries; Constant pressure at CH_4 production well
Initial CO_2 mass fraction	$X_{CO2} = 0$
Initial CH_4 mass fraction	$X_{sm} = 1$
Injection rate	0.1 kg/s until shut-down

The termination of the simulation depends solely on the mass fraction of CO_2 in the reservoir. It takes about 30 minutes of CPU time to run 2,000 days of simulation before major CO_2 contamination occurs. The recovery factor, production shut-down time, pressure and CO_2 saturation distribution in the reservoir are investigated and compared with the results of other investigators.

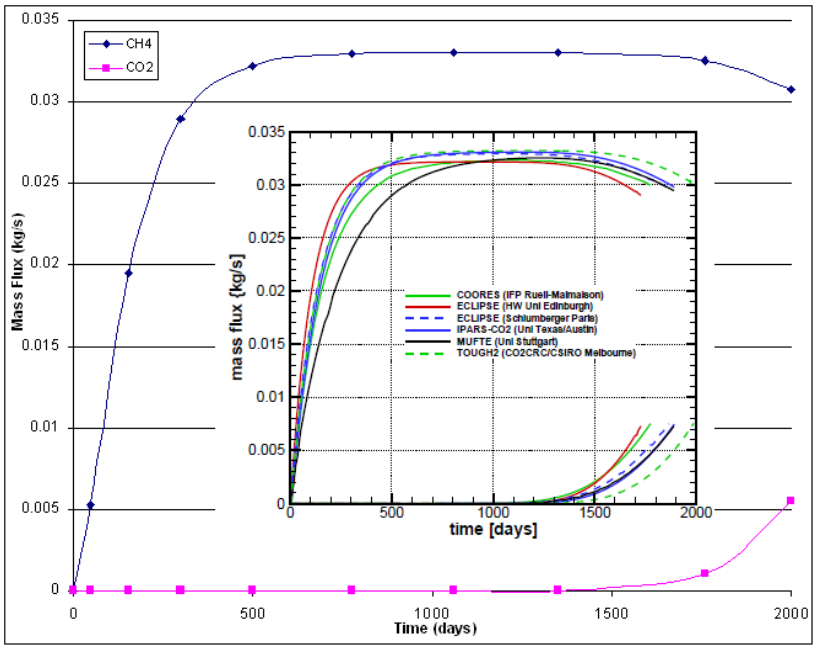

Figure 3.11 History of enhanced CH_4 recovery for benchmark problem #2

In Figure 3.11, our results using TOUGH2 are shown as the large graph, while results of simulations from other investigators are shown in the inner box. Table 3.10 provides comparisons for recovery factor and production well shut-down time with other investigators' simulations [39].

Table 3.10 Comparisons of recovery factor and production shut-down time

	Recovery Factor	Production Well Shut-down Time
TOUGH2 (WUSTL)	61.4 %	2063 days
TOUGH2 (CO_2/CRC)	58 %	1987 days
MUFTE (U. Stuttgart)	53 %	1894 days
IPARS (U. Texas)	55 %	1891 days

To visualized how the displacement process of CH_4 by CO_2 works, the density and CO_2 mass fraction profiles at production shut-down are examined in Figure 3.12.

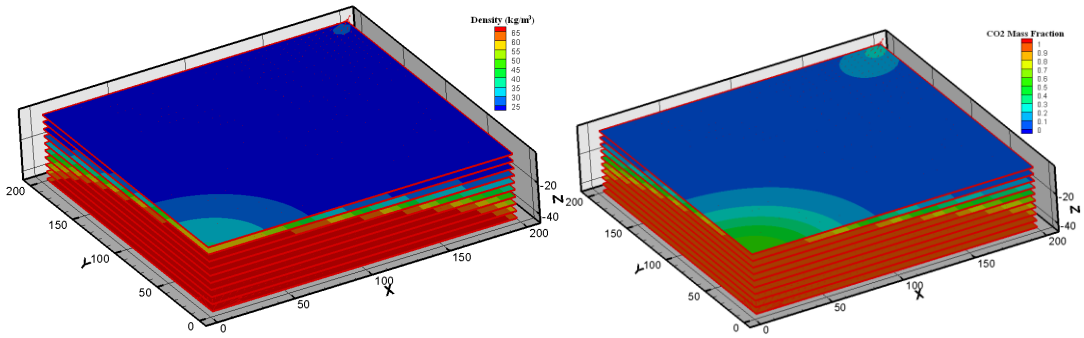

Figure 3.12 (a) Density profile (b) CO_2 mass fraction profile at production shut-down for benchmark problem #2

Figure 3.11, Table 3.10, and Figure 3.12 lead to the following four conclusions. 1) small variations in the results among different simulations with different users are un-avoidable. Such variations are expected because some parameters are intentionally left un-specified; 2) our results are in satisfactory agreement with those of other investigators; 3) it can be seen that the injected CO_2 migrates from the near lower corner to the far upper corner in a semi-spherical fashion. Unlike SAGCS, in situ CO_2 tends to sink to the bottom of the reservoir. It indicates strong gravity segregation caused by the density difference; and 4) production gas contamination caused by upward movement of CO_2 occurs at the production well despite the gravity segregation. It is due to the strong convective flow near the production well and mass diffusion.

3.3 Simulation of Benchmark Problem #3 - CO_2 Injection in a Heterogeneous Geological Formation

Accurate estimation of in situ CO_2 dissolution into the ambient brine is another important aspect of SAGCS simulation, since CO_2 becomes securely sequestrated once

dissolved. Overestimation of CO_2 dissolution could lead to underestimation of possibility of potential leakage; on the other hand, underestimation of CO_2 dissolution would result into inefficient utilization of the formation's storage potential. In the meantime, it is instructive to model a realistic geological reservoir with heterogeneous hydrogeological properties for more realistic estimation of CO_2 storage capacity. In benchmark problem #3, part of the Johansen formation off the Norwegian coast is modeled for SAGCS [38]. Johansen formation is a highly heterogeneous formation, especially in its porosity and permeability, as shown in Figure 3.13. CO_2 is injected in the middle of the modeled formation at 50 m from the bottom. The injection lasts for 25 years before it is shut down, and the total simulation time is 50 years. The goal of this benchmark study is to identify the amount of dissolved CO_2, the amount of CO_2 still in gaseous phase, and how these amounts evolve with respect to time. This study is very instructive to understand the dissolution process of injected CO_2 under reservoir conditions.

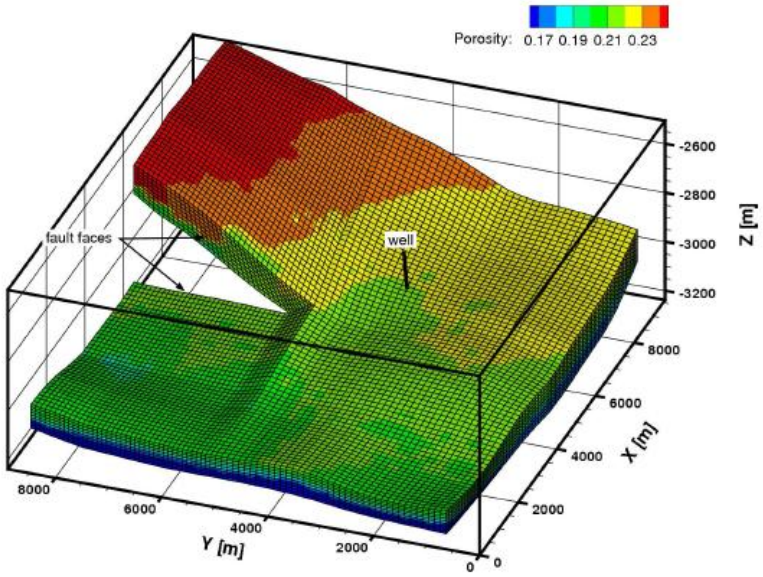

Figure 3.13 Johanson formation's porosity heterogeneity for benchmark problem #3 [38]

The geometry of the modeled portion of the Johanson formation is given in Figure 3.13. The coordinates of vertices of 54756 hexahedral cells in Cartesian system have been provided for geometry construction [38]. At each vertex, information of permeability and porosity is given. The geometry and hydrogeological properties are

available only in ASCII format, which cannot be read directly by either PetraSim or TOUGH2. Pre-processing of this information is needed as a prerequisite for simulation. The most fundamental unit of a CFD model is a single computational cell in a computational domain. With the number of computation cells given for this benchmark study, directly following the raw data of Johanson formation introduces complicated averaging scheme and impractical tedious properties assignment for each cell. Contour-mapping technique is therefore used to address these problems. To be more specific, the partial Johanson formation is first uniformly discretized into thirteen vertical layers of computational cells. Then, contour maps of porosity and permeability are drawn for each layer. Computer software Surfer 8, a contouring and mapping program developed by Golden Software, is used for this purpose. Once the contour maps are generated, areas bounded by the contours are treated as individual units with identical and uniform hydrogeological properties. Following this philosophy, the partial Johanson formation can be considered as a total of 37 units, each with its distinct porosity and permeability. A schematic of the data flow for the pre-processing described above is shown in Figure 3.14.

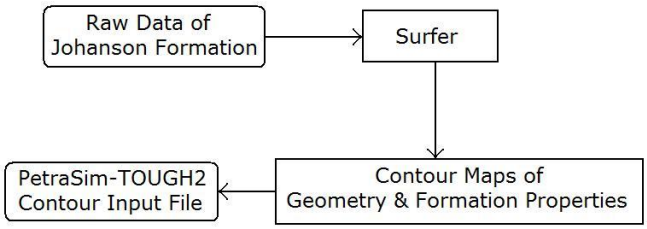

Figure 3.14 Schematic of the data flow in the pre-processing for benchmark problem #3

Table 3.11 gives the geometry parameters for benchmark problem #3.

Table 3.11 Geometry parameters for benchmark problem #3

Domain size	9600 m × 8900 m
Thickness	between 50 m and 150 m
Injection well location	x = 5440 m, y = 3300 m, bottom 50 m of the formation

Figure 3.15 shows the final CFD model of the Johanson formation.

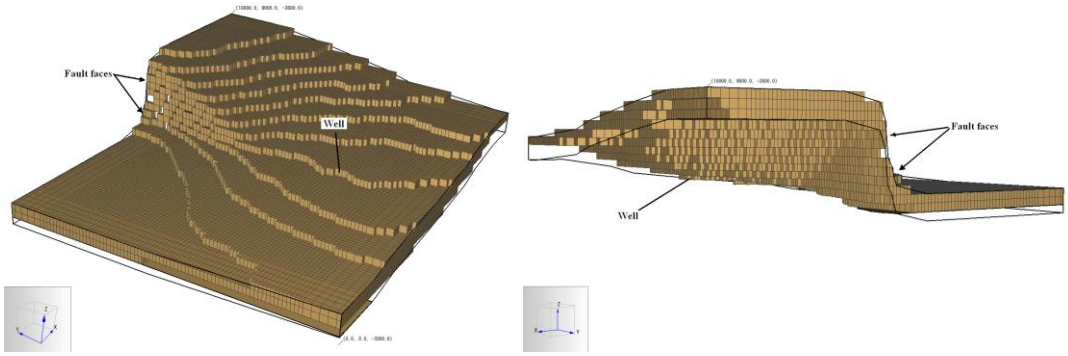

Figure 3.15 (a) Front view and (b) Rear view of the modeled Johanson formation

The porosity and permeability of the modeled Johanson formation is shown in Figure 3.16.

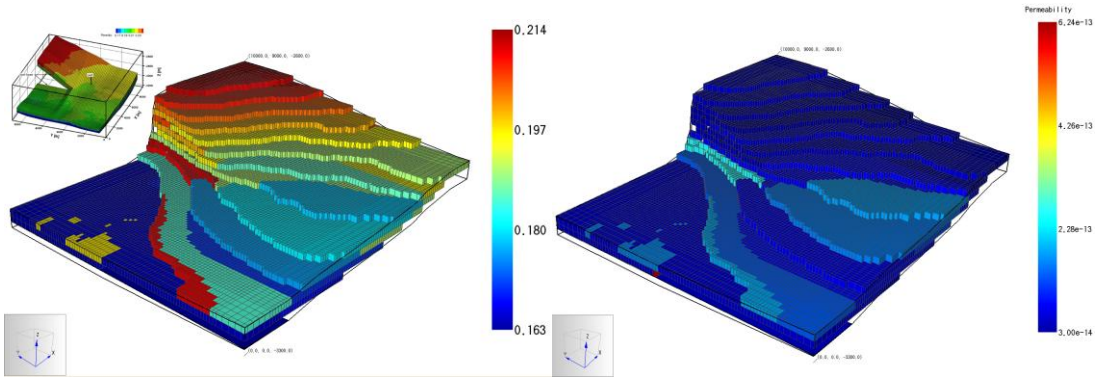

Figure 3.16 (a) Porosity and (b) Permeability of the modeled Johanson formation

Hydrogeological properties of modeled Johanson formation are summarized in Table 3.12.

Table 3.12 Hydrogeological properties of the modeled Johanson formation

Permeability	varies
Porosity	varies
Residual brine saturation	0.2
Residual CO_2 saturation	0.05
Relative permeability	Brooks-Corey
Capillary pressure	Brooks-Corey

Entry pressure	1.0×10^4 Pa
Brooks-Corey parameter	2.0

Initial conditions, boundary conditions and other parameters of the modeled Johanson formation are summarized in Table 3.13.

Table 3.13 Simulation parameters for the modeled Johanson formation

Thermal condition	Isothermal
Initial Temperature	0.03 °C/m; 100 °C at 3000 m depth
Initial Pressure	1075 Pa/m, 3.086×10^7 Pa at 3000 m depth
Boundary conditions	Fixed-state on lateral boundaries No mass flow on fault, top and bottom boundaries
Initial CO_2 mass fraction	$X_{CO2} = 0$
Initial salt mass fraction	$X_{sm} = 0.1$
Injection rate	15kg/s (for 25 years), 0 kg/s thereafter
Discretization	Number of computational grids: 18804 Non-uniform for *x*-, *y*-, *z*-directions

Both gashouse and aqueous CO_2 accumulations after 50 years are considered as benchmark criteria for making comparisons with the simulations of other investigators. In Figure 3.17 our results using TOUGH2 are shown as the large graph, while results from other simulations are shown in the inner box.

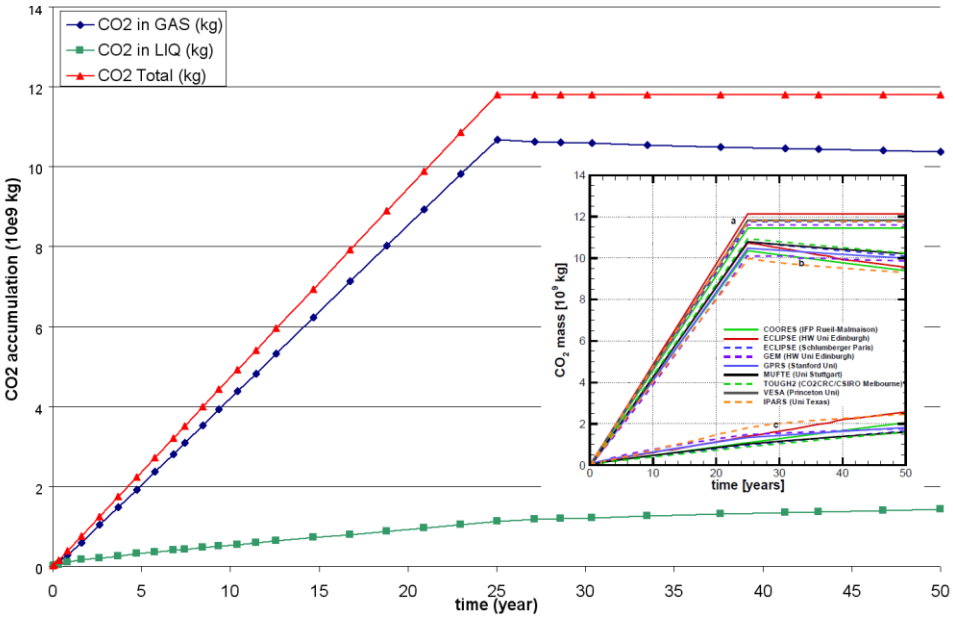

Figure 3.17 Gashouse and aqueous CO_2 accumulations for 50 years

Table 4.12 provides additional quantitative comparisons [39].

Table 3.14 Comparisons of gaseous and aqueous CO_2 accumulations at 50th year

	Gashouse CO_2 at 50th year	Dissolved CO_2 at 50th year
TOUGH2 (WUSTL)	87.9 %	12.1 %
TOUGH2 (CO_2/CRC)	86.5 %	13.5 %
IPARS (U. Texas)	79.1 %	20.9 %

A comparison of the CO_2 migration at 50 years is given in Figure 3.18.

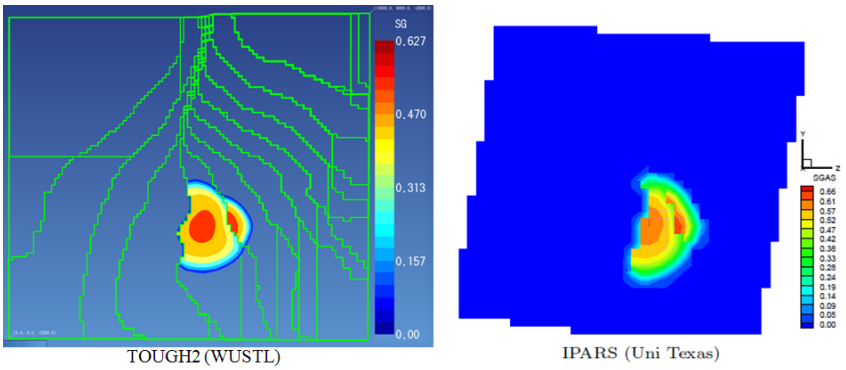

Figure 3.18 CO_2 saturation in the formation at 50th year, plan-view

Figure 3.18 and Table 3.14 lead to four conclusions. 1) small variations in the results among different simulations with different users are un-avoidable. Such variations are expected because some parameters are intentionally left un-specified; 2) our results are in satisfactory agreement with the results of other investigators; 3) CO_2 dissolution into the ambient porewater is a process that takes place very slowly; and 4) the greater slope of aqueous CO_2 during the first 25 years (when injection continues) implies the enhanced carbon dissolution due to convection during first 25 years.

3.4 Conclusions

From the benchmark simulations presented in this chapter, it is demonstrated that TOUGH2 numerical simulator is capable of producing accurate and consistent results for various types of problems related to GCS. These simulations allow us to conduct simulations of large scale SAGCS in identified saline formations with confidence, and proceed towards the development of numerical optimization module for TOUGH2 and perform optimization designs of innovative reservoir engineering techniques for enhanced SAGCS safety and storage efficiency.

Chapter 4

Simulation of GCS in Identified Large Scale Saline Aquifers

The accurate large scale simulations of existing SAGCS projects for identified aquifers are crucial to the future deployment of SAGCS projects. Although detailed history-matching simulations of existing SAGCS projects are challenging due to various uncertainties, e.g. in the reservoir topography and hydrogeology, the simulations can still provide informative insights in several aspects of SAGCS, such as the variance in multiphase flow properties, integrity of the geological seals, and the mechanism of CO_2 trapping. Such insights are essential for better understanding of the nature of SAGCS and its best practices for deployment. Detailed history-matching simulations have always been an important part in the SAGCS research activity.

In our research, we have considered the simulations for three identified saline aquifers, among which two are for the purpose of history-matching and one for cross-comparison since the actual injection has recently begun. These three identified saline aquifers are, Mt. Simon formation located in the Midwest region of the US, Frio formation located in the Gulf region of the US, and the Utsira formation located in the North Sea by the Norwegian coast. Some brief descriptions of these three aquifers have been covered in Section II. More details on the recent studies of these three aquifers, including field tests and numerical simulations are provided in the following sections.

4.1 SAGCS Simulation for Mt. Simon Formation

Located at Illinois basin, Mt. Simon sandstone formation is a huge saline aquifer that covers most of Illinois, southwestern Indiana, southern Ohio, and western Kentucky. The estimated storage capacity of Mt. Simon formation ranges from 27000 to 109000 million tons of CO_2 [40],[41]. Midwest Geological Sequestration Consortium (MGSC) is the regional consortium conducting studies of the possibility of large scale GCS throughout the Illinois basin. Decatur GCS Project and FutureGen 2.0 Project are two most well-known SAGCS projects being currently carried out at Mt. Simon formation.

The depth of Mt. Simon formation varies significantly throughout its coverage [41][42]. In the southern part, it reaches as deep as 4300 m below the mean sea level (MSL); while it increases to 80 m below the MSL in the north. Consequently a south-north geological slope of approximately 8 m/km has been estimated. The thickness of Mt. Simon formation also changes significantly. A maximum thickness of 800 m in the north has been measured while it diminishes to zero in the further south. Other than the variance in topography, analysis of rock samples has suggested strong anisotropy in the formation's hydrogeological properties, with porosity ranging from 0.062 to 0.2 and permeability ranging from 5 mDarcy to 1000 mDarcy. Low permeable Eau Claire shale which sits above the Mt. Simon formation serves as the caprock. Except for some small regions near Mississippi river, Eau Claire shale is considerably thick (more than 90 m) throughout most of the Illinois basin. The security of SAGCS over Mt. Simon formation is therefore greatly assured by the continuous coverage of Eau Claire shale. Precambrian granite formation stretches beneath Mt. Simon saline aquifer.

Recent geological survey has suggested an area in the center of the Mt. Simon formation to be the core injection area – an area in which future storage sites are likely to be located. This core injection area is indicated as the area compressed by white boundary in Figure 4.1, along with the elevation information of Mt. Simon formation. As can be seen from Figure 4.1, both ADM project and FutureGen 2.0 project are located in the core injection area.

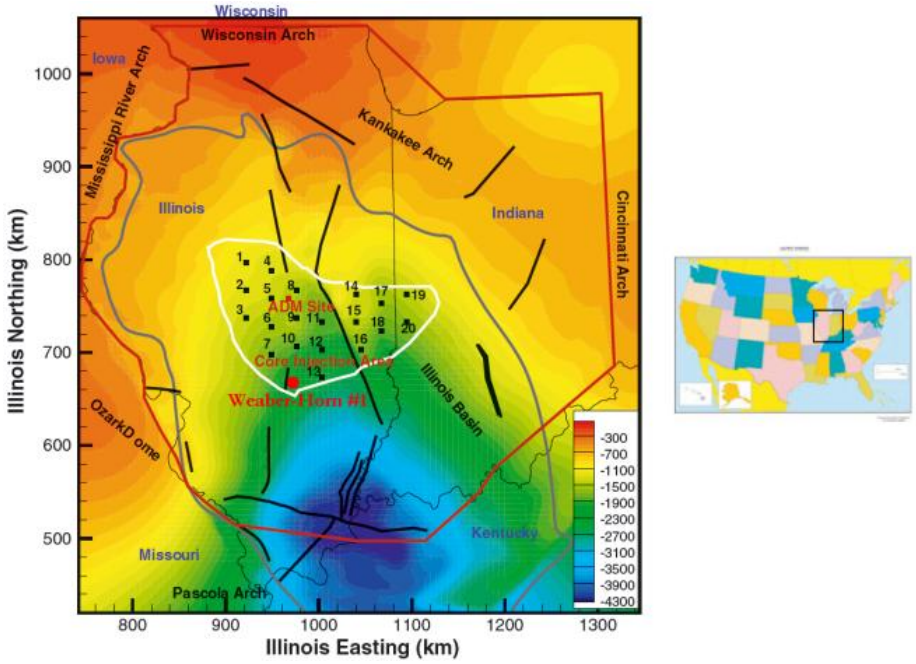

Figure 4.1 Core injection area and elevation of Mt. Simon Sandstone

ADM SAGCS project, which targets to store 1 million tons of CO_2 over three years, is the first large scale SAGCS demonstration being conducted at Mt. Simon formation. This demonstration project is carried out at the Archer Daniels Midland Company (ADM) plant site in Decatur, Illinois. Drilling of a 2,200 m injection well was completed in May 2009, a second geophysical well was completed in September 2009 for enhanced data recovery during repeat walk-away vertical seismic profiles planned throughout the project, and a third deep in-zone monitoring well was completed in April 2011. CO_2 Injection has begun since 2012. The numerical simulation study of the ADM SAGCS project is of great interest. Nevertheless, detailed field data of reservoir performance, such as reservoir pressure perturbation and seismic imagines of the CO_2 distribution, has not been made available yet due to the relatively short-period since the beginning of injection. With the consideration of data availability, a candidate site for future sequestration project, the Weaber-Horn #1 well (WH #1 well shown as the red dot in Figure 4.1), has been chosen for our simulation study.

Mt. Simon sandstone is a typical stratified saline formation. According to the geological survey, strong anisotropy in porosity, permeability, and capillary pressure exists through the entire depth of the formation. Based on variance of porosity, Mt. Simon formation can be distinguished as four subunits, namely an upper unit with sandstone and shale tidally influenced and deposited, a middle unit with relatively clean sandstone, an Arkosic unit with highly porous and permeable sandstone, and a lower unit with decreased porosity and permeability. The high porosity and permeability of Arkosic unit makes it an ideal candidate for the injection to take place. When modeling, these four subunits of Mt. Simon are further divided into 24 layers, each of which has a layer-averaged porosity and permeability value (Figure 4.2) [40],[43]. The detailed well log of WH #1 well is shown in Figure 4.2 and summarized in Table 4.1. It is desired to model the anisotropy of hydrogeological properties as accurately as possible to capture its effect on in situ CO_2 transport. It should be noted that the lower unit of Mt. Simon formation is not considered in the modeling due to its absence near WH #1 well. Both Eau Claire shale and Precambrian granite are modeled as impermeable formations.

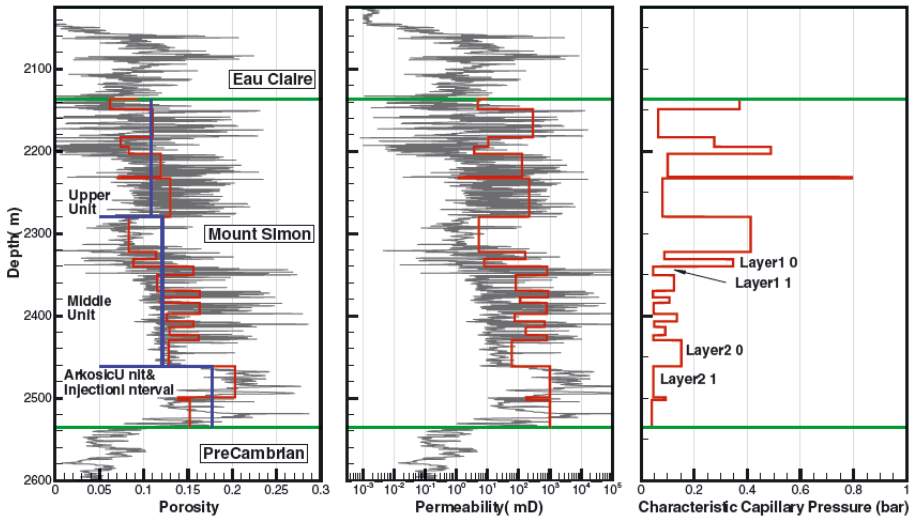

Figure 4.2 Layer properties (in red line) of measured porosity, calculated permeability, and scaled characteristic capillary pressure for the 24 layers of the Mt. Simon and the Eau Claire and the Precambrian granite at WH #1 well. Also shown is the division (in blue line) of the four hydrogeological units of the Mt. Simon Sandstone, as well as the core-scale (0.15 m) porosity and permeability (in gray line).

Table 4.1 Porosity, permeability, and characteristic capillary pressure of the 24 layers of Mt. Simon at injection site WH #1

Sub-Unit	Sub-Layer	Layer Depth (m)	Mean Porosity	Mean Permeability (mDarcy)	Characteristic Capillary Pressure (bar)
Upper Unit	1	2140 – 2150	0.061	5	0.37
	2	2150 – 2182	0.109	300	0.06
	3	2182 – 2197	0.074	10	0.28
	4	2197 – 2203	0.083	3.6	0.4875
	5	2203 – 2230	0.195	110	0.1
	6	2230 – 2232	0.071	1.1	0.8
	7	2232 – 2280	0.13	210	0.083
Middle Unit	8	2280 – 2322	0.083	5.4	0.4125
	9	2322 – 2331	0.24	150	0.0875
	10	2331 – 2340	0.088	8	0.35
	11	2340 – 2350	0.156	800	0.095
	12	2350 – 2370	0.25	80	0.125
	13	2370 – 2378	0.163	900	0.095
	14	2378 – 2385	0.195	105	0.1007
	15	2385 – 2399	0.163	800	0.05
	16	2399 – 2406	0.136	72	0.1167
	17	2406 – 2412	0.156	700	0.05
	18	2412 – 2424	0.129	160	0.09
	19	2424 – 2430	0.161	850	0.05
	20	2430 – 2462	0.128	60	0.15
Arkosic Unit	21	2462 – 2500	0.202	1000	0.05
	22	2500 – 2502	0.14	190	0.09
	23	2502 – 2537	0.151	1000	0.04

A cylindrical model of Mt. Simon formation is constructed. For thermal condition the model uses calculated values with a thermal gradient of 9.2 ^{o}C/km. The reservoir pressure is assumed to be hydrostatic pressure with a gradient of approximately 10.8 MPa/km from the ground surface. Salinity is assumed to increase with the depth, starting from 235 mg/L at 450 m below ground surface with a gradient of 12.8 mg/L per meter in depth. A north-south geological gradient of 0.008 m/km is also considered in the modeling. "No-flux" boundary condition is applied at top and bottom of the model, representing the impermeable upper and lower bounding formations. "Fixed-state" boundary condition is imposed at the lateral boundary to represent an essentially "open" reservoir. The permeability and porosity of the 24 sublayers can be seen in Figure 4.3.

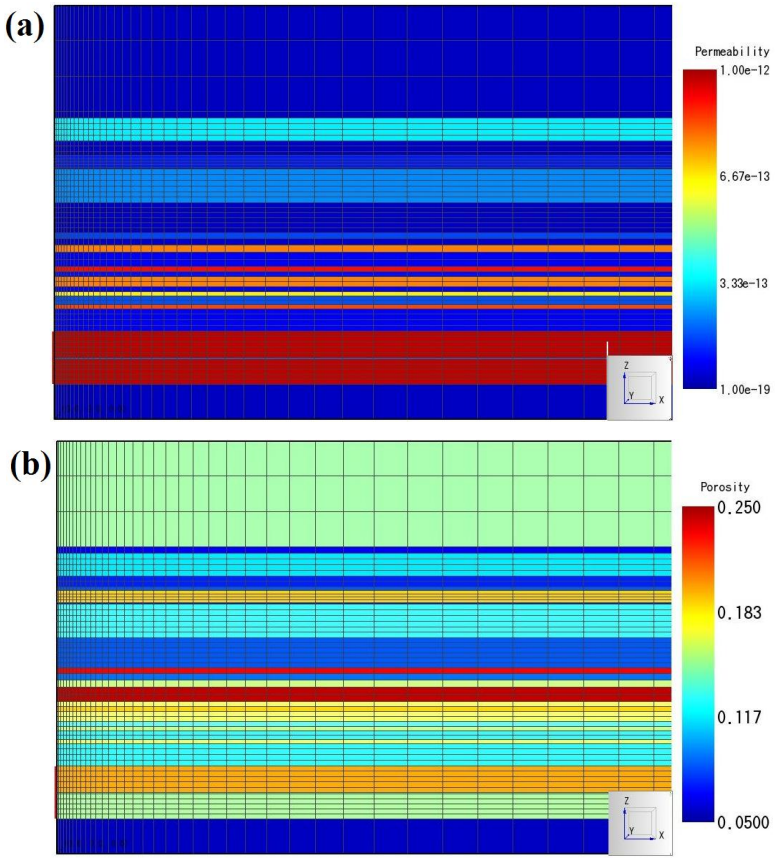

Figure 4.3 (a) Permeability, (b) porosity, and computational mesh of the 24 sublayers of the Mt. Simon formation model at WH #1 well

Due to the relatively high porosity and permeability, CO_2 injection is assigned at the bottom Arkosic unit (bottom three sub-layers). The injection rate is assigned to be 5 million tons per year and injection lasts for 50 years. CO_2 footprint at 5^{th} year, 25^{th} year, and 50^{th} year since the beginning of injection is examined. Zhou et al.'s work [43] for Site#10 (shown in Figure 4.1) is also presented for reference. It should be noted that our results and Zhou et al.'s results are not strictly comparable due to the inconsistent site locations.

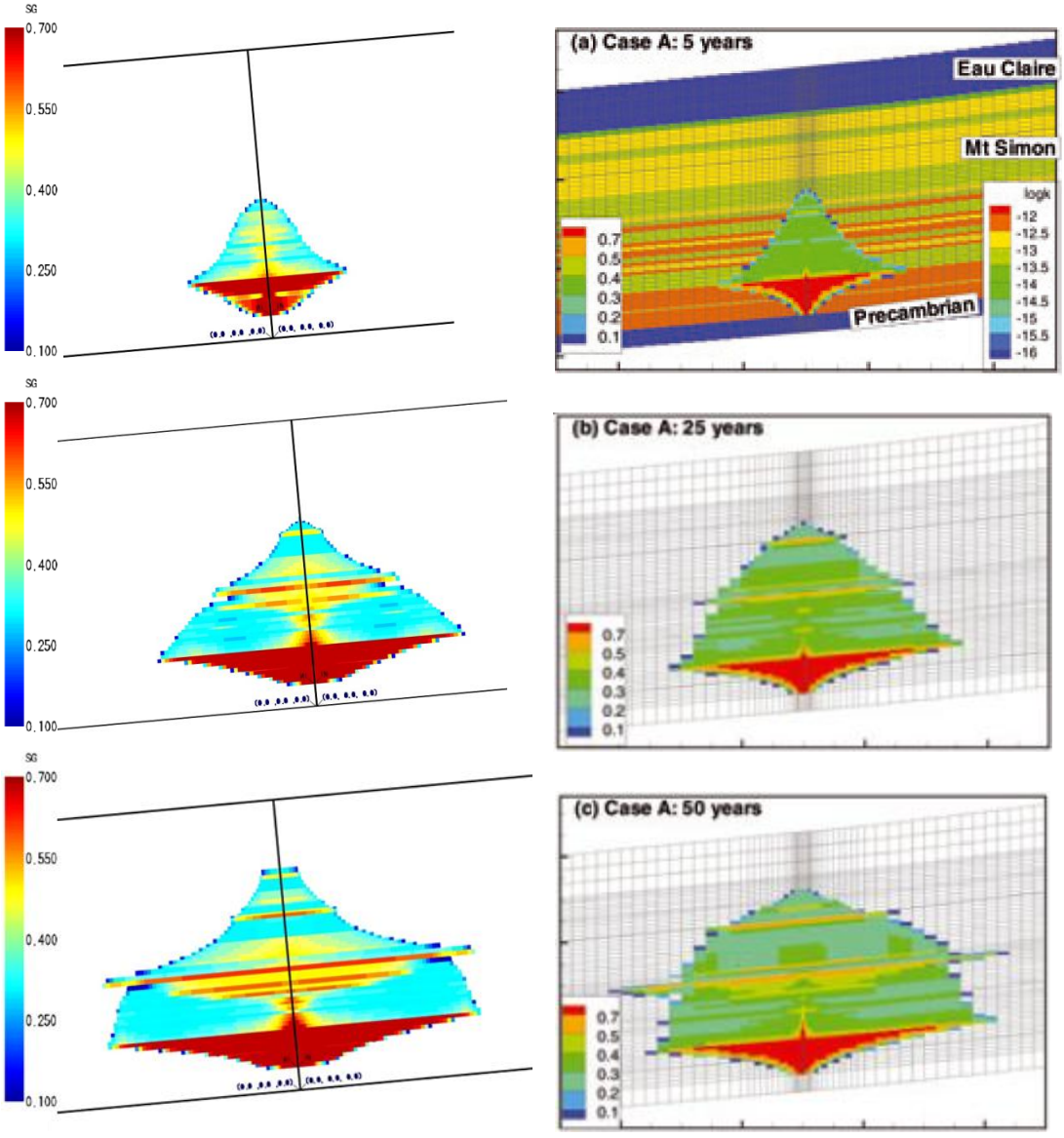

Figure 4.4 Saturation of gaseous CO_2 at (a) 5th (b) 25th and (c) 50th year of injection

As seen in Figure 4.4, CO_2 plume evolves with a complex spatial pattern during the 50 years of injection. Within the Arkosic unit where the injector is located, extensive lateral migration with relatively higher concentration of gaseous CO_2 is observed. In the overlying sub-layers, however, strong secondary sealing effect that retards the vertical migration of gaseous CO_2 is observed as the pyramid-shaped subplume. Detailed analysis of secondary sealing effect is made as follows.

As shown in Figure 4.4(a), the injected CO_2 migrates laterally away from the injector within the highly permeable Arkosic unit in the first 5 years since the beginning of injection. Simultaneously, buoyancy also leads to upward movement of CO_2 until it encounters the immediately overlying low permeability sublayer (sublayer #20). The low permeability of sublayer #20 directly results into higher capillary pressure experienced by mobile CO_2, and thus stronger vertical pressure gradient is required for mobile CO_2 to penetrate sublayer #20. When the capillary pressure is greater than the phase pressure of CO_2, sublayer #20 appears to be "impermeable" to the underlying CO_2 plume. Consequently, gaseous CO_2 accumulates under this layer and continues spreading out laterally, finally reaching a maximum extent of approximately 3000 m. Meanwhile, the increased CO_2 column under sublayer #20 brings up its phase pressure. Once the phase pressure of CO_2 exceeds the entry pressure of the sublayer #20, mobile CO_2 breaks the capillary barrier of its overlying layer and starts to penetrate it. Such accumulation-penetration-breakthrough behavior of gaseous CO_2 occurs each time the upward migrating CO_2 encounters an overlying sublayer with lower permeability. Because the high capillary entry pressure of the overlying layer temporarily prevents CO_2 migrating upwards, such phenomenon is identified as secondary sealing effect. As can be seem from Figure 4.4, secondary sealing effect is a very effective means to retard the upward migration of in situ CO_2. Its contribution makes gaseous CO_2 barely reach the Eau Clair shale even after 50 years of injection.136

A quick formulation of the criteria for the capillary barrier breakthrough can be achieved in the following fashion. Let ΔCP be the difference in capillary pressure on both sides of the layer interface with sharp changes in rock properties, h_{CO2} be the column height of CO_2 underneath the overlying layer, S_a be the residual saturation of porewater, and ΔF_b be the buoyancy driving force. Then the buoyancy driving force can be evaluated as

$$\Delta F_b = \left(\rho_w - \rho_{CO_2}\right) \cdot (1 - S_a) \cdot h_{CO_2} \qquad \text{(Eq. 31)}$$

Since ΔCP and ΔF_b are competing forces, to allow the sub-caprock breakthrough, it requires $\Delta F_b > \Delta CP$. Therefore, the critical column height of CO_2 to trigger this breakthrough can be determined as

$$h_{CO_2,critical} = \frac{\Delta CP}{(1-S_a)\left(\rho_w - \rho_{CO_2}\right)} \quad \text{(Eq. 32)}$$

For Mt. Simon, the representative values of in situ fluid density are brine density ρ_w=1100 kg/m^3 and supercritical CO_2 density ρ_{CO2}=900 kg/m^3. Capillary pressure difference between sublayer #20 and sublayer #21 can be evaluated as $\Delta CP \approx 0.11$ bar, which is approximately the difference of the entry pressure between the two sublayers. The residual saturation of porewater is set at 0.15. Therefore, one can determine that CO_2 would start penetrating from the Arkosic unit into its overlying sublayer #20 when the CO_2 column height exceeds 6.47 m. Because CO_2 column height decreases radially from the injection well, the strength of upward migration also decreases radially. A direct result is the pyramid-shaped CO_2 distribution over sublayer #20 in the formation. Comparing our results with those of Zhou et al., following conclusions can be made. (1) Overall both sets of results are in good match in capturing the characteristics of Mt. Simon formation, such as the shape of the plume, tendency of migration, and maximum lateral extent. (2) Secondary sealing effect is very effective in retarding the upward migration of in situ mobile CO_2. (3) The geological updip appears to have insignificant effect on CO_2 migration as no prominent asymmetric plume can be observed. Similar conclusions can also be drawn from Zhou et al.'s work that is based on a nearby injection site. (4) Taking the maximum lateral extent of CO_2 plume in the Arkosic unit to be r_{max}, CO_2 migrates laterally from the injection well without prominent evidence of gravity-override up to about $r_{max}/2$ in our simulation, indicating strong injection-induced Darcy flow. Away from this region, buoyancy starts to dominate and thus shows significant gravity-override. However, Zhou et al.'s work suggests buoyancy-dominated CO_2 plume developing immediately from the injection well. The discrepancy in the plume shapes in the two simulations can be explained by the inconsistent hydrogeological properties applied for the two different locations (WH #1 well in our study and Site #10 well in Zhou et al.'s study).

4.2 SAGCS Simulation of Frio Formation

The SAGCS pilot project for Frio deep saline formation near the Gulf coast is the subject of study in this section. The Frio project has two characteristics that make it attractive for numerical study. First, it is a completed pilot project with detailed field data available; secondly, hysteresis information of relative permeability and capillary pressure has been obtained from the core sample of Frio saline formation. The hysteresis effect is an important factor in to obtaining accurate estimation of CO_2 migration and dissolution for full-term SAGCS simulation. A full-term simulation refers to a simulation that investigates the fate of in situ CO_2 through the entire life cycle of a SAGCS project, which usually consists of both injection and post-injection periods.

The Frio SAGCS pilot project was conducted at the South Liberty oil field operated by Texas American Resources in Dayton, Texas (shown in Figure 4.5). Starting from October 4 in 2004, 1600 tons of CO_2 was injected into the Frio formation about 1500 m below the ground surface within 10 days. The Frio formation consists of brine-bearing sandstone with high permeability beneath the Gulf Coast. It is a relatively thin sandstone layer of only 23 m in thickness. Steep geological updip of 16^o from south to north has been identified for Frio formation [44]. The Frio pilot project employed one injection well and one observation well about 33 m to its north. Other than the conventional pre-injection geological surveys, laboratory analysis of core samples has suggested the hysteresis behavior of relative permeability and capillary pressure in Frio formation. The hysteresis has been considered in our simulations.

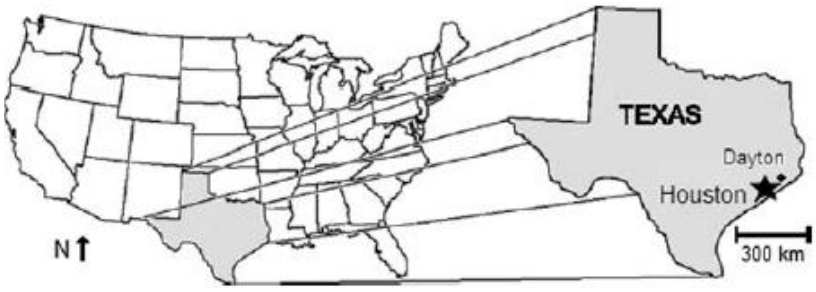

Figure 4.5 Location of the Frio pilot SAGCS project [45]

The reservoir geometry, hydrogeological parameters, and simulation parameters of the modeled Frio formation are summarized in Table 4.2.

Table 4.2 Geometry and hydrogeological parameters Frio formation

Geometry	800 m × 2500 m × 23 m
Geological updip	16 ^{o}
Injection Interval	5.5 m from the caprock
Permeability	isotropic 1.0×10^{-12} m^2
Porosity	0.28
Residual brine saturation	0.15
Residual CO_2 saturation	0.2
Relative permeability	van Genuchten-Mualem
Capillary pressure	van Genuchten-Mualem
Thermal condition	Isothermal
Boundary conditions	Northwest, southwest and southeast: closed boundary Northeast: open boundary
Initial conditions	P = 152 bar, T = 59 ^{o}C for equilibrium simulation
Initial CO_2 mass fraction	$X_{CO2} = 0$
Initial salt mass fraction	$X_{sm} = 0.093$

Characteristics of capillary pressure and relative permeability have been obtained from mercury-injection laboratory experiments on core samples from Frio formation, given in Figure 4.6. Hysteresis in both capillary pressure and relative permeability can be clearly observed. Drainage (of porewater) curves are marked red and imbibition (of porewater) curves are marked blue. When multiple drainage-imbibition cycles occur, different imbibition curves represent different orders of drainage-imbibition cycles. The primary imbibition curve, i.e. when brine imbibition occurs for the first time, is depicted as a bold solid curve. Since only one drainage-imbibition cycle takes place when continuous CO_2 injection is imposed before it is permanently shut down, only the primary imbibition curve needs to be considered in the modeling.

The consideration of hysteresis introduces an additional degree of freedom to the modeling. Not only the current conditions, but also those in the previous time step

determine the relative permeability and capillary pressure at the current time. That is, time domain solution needs to be considered in the determination of relative permeability and capillary pressure when hysteresis is enabled. The fundamental approach for including hysteresis in the modeling is as follows. First, drainage and imbibition characteristic curves with respect to aqueous phase saturation are modeled separately using the information obtained from the laboratory experiments. Secondly, change in saturation of each phase is evaluated at each time-step to determine which curve, drainage or imbibition, should be used. If the saturation of a certain phase at current time-step is smaller than that at the previous time-step, it means drainage (of such phase) occurs, and capillary pressure and relative permeability should be determined from the drainage curve (of such phase); on the other hand, if the saturation of a certain phase at current time-step is greater than that at the previous time-step, it means imbibition (of such phase) occurs, and the imbibition curve (of such phase) should be used. It should be noted that brine acts as aqueous phase and supercritical CO_2 acts as gaseous phase in the context of SAGCS, and the sum of their saturation should be unity at any time.

The hysteresis modules of capillary pressure and relative permeability have already been developed for Frio formation by Doughty et al. using a similar technical approach [45]. The modules have been incorporated into the iTOUGH simulator, which is a variation of TOUGH2 for inverse simulation ("i" stands for "inverse"). Uncertain hydrogeological properties can be inversely obtained by feeding iTOUGH with necessary field/experiment data. Although primarily developed for inverse simulations, the functionality of conventional forward simulation has been preserved in iTOUGH. When performing the forward simulation, iTOUGH is identical to the original TOUGH2 solver with additional capability of accounting for the hysteresis effect. Therefore, iTOUGH has been used for the simulation study of Frio SAGCS project.

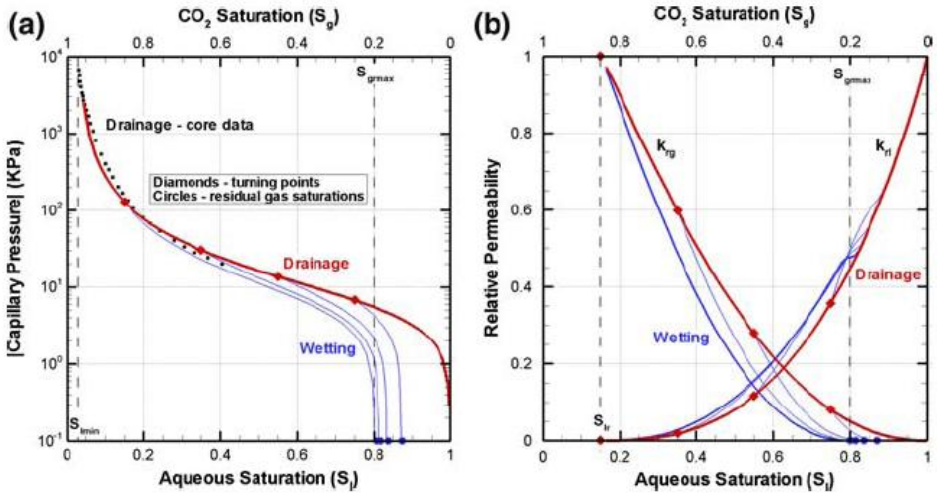

Figure 4.6 Capillary pressure and relative permeability characteristics of Frio formation [45],[46]

According to Doughty et al.'s suggestions, a rectangular portion of Frio formation with dimension of 2500 m northwest-southwest, 800 m northeast-southeast, and 23 m thickness is modeled, as shown in Figure 4.7. The injection well is located at a point with coordinate (x=560 m , y=800 m) from the lower left corner of the computational domain. Although the formation is 23 m in thickness, injection only takes place over the first 8 m from the caprock. An observation well is located 33 m to the north. Because flow transport is most intense near the injection and observation wells, they are evolved in a computational domain dimension 30 m × 30 m is refined to accurate capture of follow pattern. The injection and observation well locations, well depth, computational mesh, and north-south updip of the numerical model are all shown in Figure 4.7 and Figure 4.8.

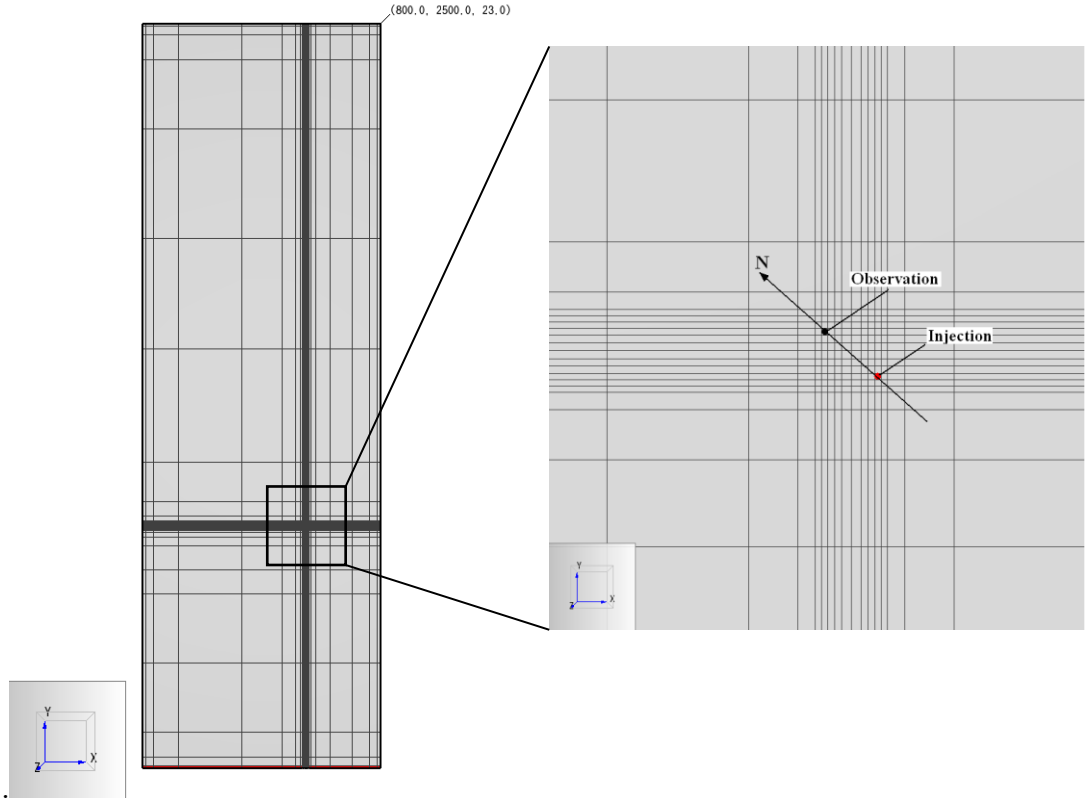

Figure 4.7 Model geometry and mesh in a portion of Frio formation

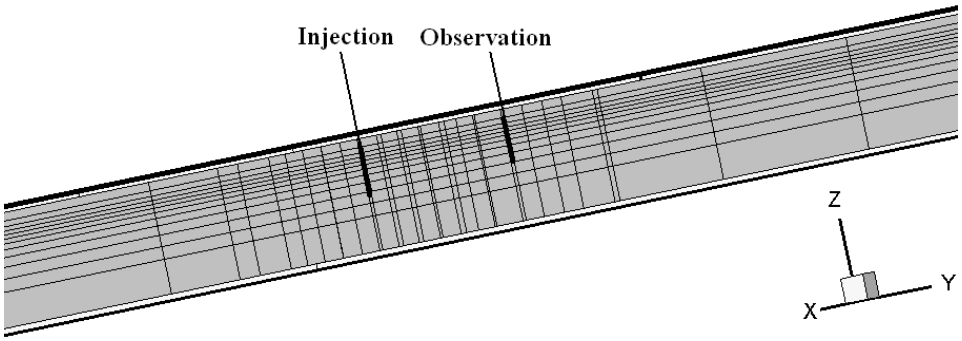

Figure 4.8 Zoom-in side view of the injection and observation wells

The simulation time is set at 10 days to match the actual duration of injection. It takes approximately 12 hours of CPU time for the simulation to complete. The profiles of gaseous phase CO_2 at the end of injection in the vertical cross-section containing both injection and observation wells are shown in Figure 4.9. Doughty et al.'s result is also shown in Figure 4.9 for comparison purpose.

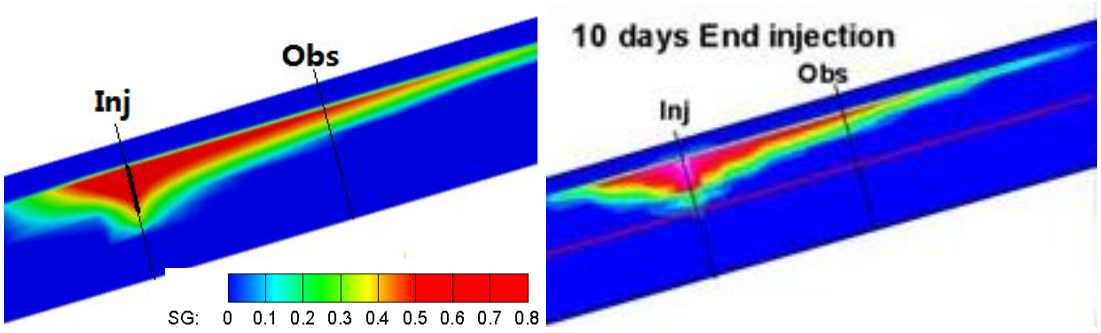

Figure 4.9 CO_2 footprint at 10th day when injection stops (comparison with Doughty et al.'s work)

Additionally, Figure 4.10 shows the CO_2 saturation profile at injection and observation wells obtained by our simulation; it is compared with that given by Doughty et al.'s work and the reservoir saturation tool (RST) logs [45]. The RST well logs are actual measurements in the field during the pilot project.

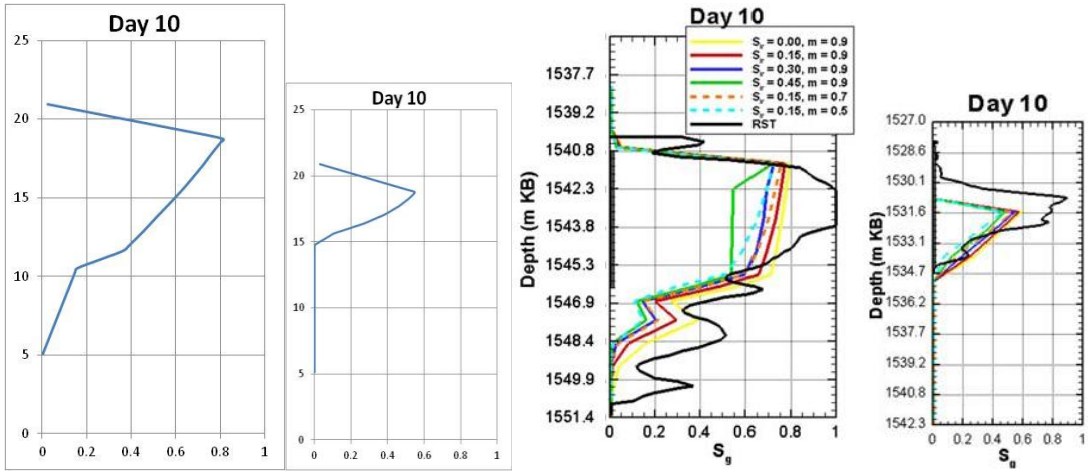

Figure 4.10 CO_2 saturation profiles given by simulations and RST logs

As seen from Figure 4.9, highly asymmetric CO_2 plume suggests strong tendency of moving up toward the geological updip. Unlike the case of Mt. Simon SAGCS, CO_2 plume of Frio project shows a shape of a down-side pyramid, which implies the lack of secondary sealing effect. Both the asymmetric migration and down-side pyramid-shaped plume indicate strong evidence of the dominant role of gravity segregation in determining the in situ CO_2 migration. Considering the relatively short-term injection (10 days) for Frio SAGCS project, it implies that in situ CO_2 migrates mostly

convectively. Furthermore it has been demonstrated that the poor permeability caprock layer above the injection well serves quite well as the CO_2 barrier.

Comparing our results with those from Doughty et al. [45], following conclusions can be made. (1) Overall our results are in good agreement with those of Doughty et al. for the plume shape, tendency of migration induced by the updip, distance of migration, gaseous CO_2 saturation, etc. (2) Discrepancy still exists at detailed simulation level. The results show that in our simulations, CO_2 saturation at the injection well reaches a maximum of 0.8 by the 10^{th} day of injection. Though being consistent with Doughty et al.'s work, it differs from the field data. Results from the RST measurement suggest a CO_2 saturation value of 1.0, i.e. dry-out of brine, occurs adjacent to the injection well. The occurrence of brine dry-out is fairly common near the injection well due to the strong pressure gradient. However, the absence of brine dry-out in both our and Doughty et al.'s simulations can be explained by the designated brine residual saturation value. In our TOUGH2 simulations, a brine residual saturation value of 0.15 is pre-assigned to the entire computational grid including that gridding the injection wells. Since residual saturation describes the minimum saturation value of a certain phase being displaced, it means that minimally 15% of the pore space will remain occupied by brine regardless of the pressure gradient. A direct result is the capped CO_2 saturation value at 0.85 and the absence of brine dry-out. (3) Our simulation shows quicker decrease in gas saturation during the injection interval. In Doughty et al.'s work, the gas saturation only drops from 0.8 to 0.65 for the upper 5 m of injection depth. In contrast, it drops from 0.8 to 0.4 in our simulation. This implies stronger buoyancy in our simulation, and thus results in a steeper inclined CO_2-brine interface. This also explains the slight overshoot in the plume migration to the north in our simulation.

4.3 SAGCS Simulation for Utsira Formation

The Sleipner project near the Norwegian coast at North Sea is probably the most prestigious, important and successful SAGCS demonstration so far. It has the most complete topographic description, industrial-scale injection amount, and long-term

monitoring data. Nevertheless, great uncertainties still exist for accurate reservoir-scale simulation of the Sleipner SAGCS project. Simulation studies of this project can provide helpful insights in understanding the transport behavior of in situ CO_2 and the reservoir performance.

Starting from 1996, the Sleipner field in the North Sea (Figure 4.11) has been the host of the world's first commercial SAGCS project. CO_2 is captured from the gas mixture produced from a nearby deeper natural gas reservoir. Until today, approximately 1 million tons of supercritical CO_2 has been sequestered annually.

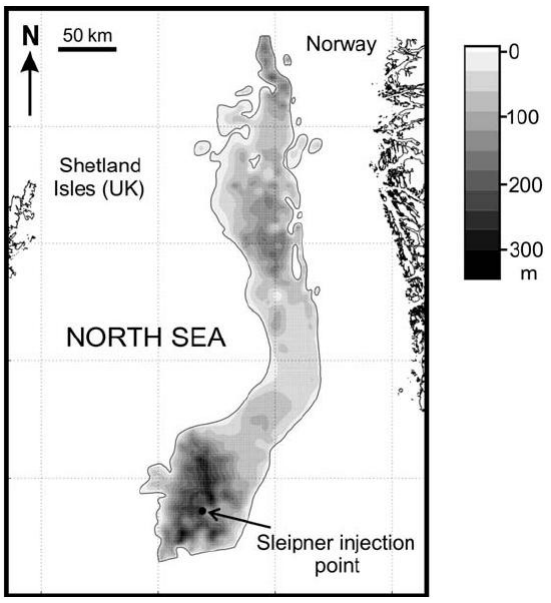

Figure 4.11 Utsira formation location and thickness of the Sleipner SAGCS [47]

Utsira saline aquifer is the target formation for permanent carbon sequestration for the Sleipner SAGCS project. Utsira formation is located at a depth of 800 m – 1100 m from the seabed with thickness of about 200 m – 250 m. The injection site is located at the southern portion of Utsira formation as shown in Figure 4.11. A 250 m – 330 m thick shale layer known as the Nordland Formation serves as the caprock, and core testing has suggested its potential of bearing CO_2 column of at least 100 m but perhaps up to 400 m (depending on the in situ conditions). It is estimated that Utsria formation has permeability of about 1 Darcy – 8 Darcy, porosity of about 0.35 – 0.4, and temperature

of about 34 °C – 37 °C. It is also estimated that the reservoir bears hydrostatic pressure from its overburden formations. Similar to Mt. Simon formation, Utsira formation is also highly stratified, consisting of sublayers with high-permeability sandstone and low-permeability shale. Therefore, it is expected that secondary sealing effect will occur. Figure 4.12 shows a 2-D seismic image taken in 2008 revealing CO_2 plume in Utsira formation. Multiple layers can be distinctly identified from the seismic image.

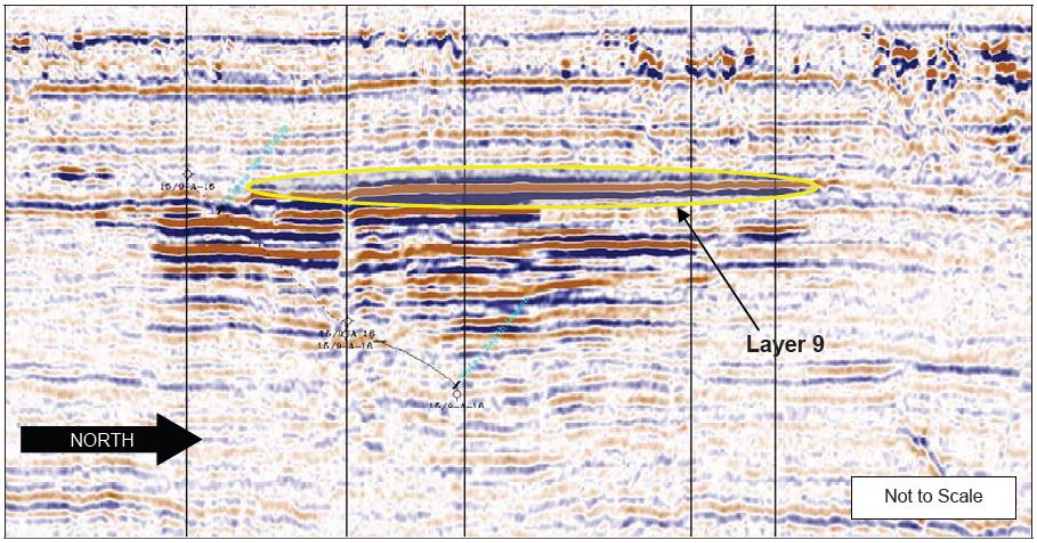

Figure 4.12 Seismic image of Utsira formation after 9-years of injection, S-N cross-section [47]

Two numerical models have been constructed for the study of Sleipner SAGCS project. The first model is a generalized axisymmetric layered model for estimating the ballpark migration of in situ CO_2. The purpose of this simulation is to determine the secondary sealing effect and gain an overview of the plume migration within Utsira formation. The second model describers a total of 48 km^2 area of detailed topmost sandstone layer (marked as Layer #9 in Figure 4.12). Layer #9 is of particular interest regarding the safety of the sequestration project, as it is the layer within which highest concentration of gaseous CO_2 exists and most significant plume migration occurs. Detailed topography of Layer #9 is shown in Model #2, making it a complicated 3D model. The 3D Layer #9 model is introduced to investigate the effect of actual topography on in

situ CO_2 migration, while avoid intensive computational effort associated with full 3D modeling and simulation of the entire Utsira formation.

4.3.1 Model #1 – Generalized Stratified Model of Utsira Formation

Pre-injection geological survey has unveiled the layered structure of Utsira formation. The majority of Utsira formation can be identified as an 8-layered structure, however, one extra layer needs to be added to the structure near the injection site due to the existence of a sand wedge as shown in Figure 4.13 [47].

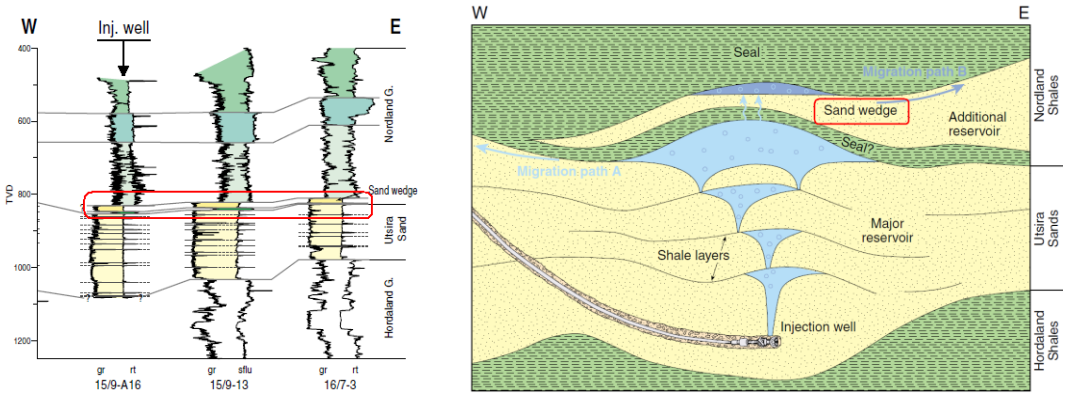

Figure 4.13 Wireline log profile and conceptual schematic of Utsira formation [47]

Therefore, a cylindrical domain with nine alternating sandstone and shale layers is constructed. According to the seismic survey, it is assumed that all four shale layers have identical thickness of 5 m, four shallower sandstone layers have identical thickness of 25 m, and the bottom sandstone layer has a thickness of 60 m. It adds up to a total 180 m thickness for the modeled Utsira formation. Lateral radius of the generalized cylindrical model reaches 100 km, which is about the same as the actual extent of the southern part of Utsira formation as shown in Figure 4.11. Figure 4.14 illustrates the layered structure of the modeled Utsira formation.

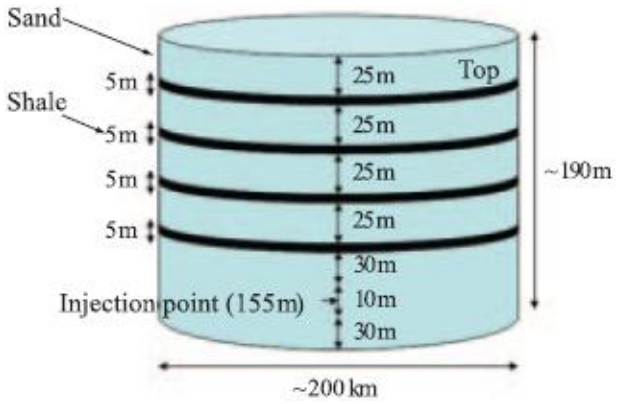

Figure 4.14 Schematic of the generalized 9-layered model of Utsira formation [48]

According to Audigane et al. [48], all sandstone layers have identical and isotropic hydrogeological properties, and so do the shale layers. Table 4.3 summarizes the hydrogeological properties used for the generalized cylindrical model.

Table 4.3 Hydrogeological properties of the generalized 9-layered model of Utsira formation

Number of layers (sand)	5
Number of layers (shale)	4
Layer thickness (sand)	Bottom layer: 70 m; other layers: 25 m
Layer thickness (shale)	5 m
Permeability (sand)	3 Darcy
Permeability (shale)	10 mDarcy
Porosity (sand)	0.42
Porosity (shale)	0.1025
Temperature	37°C
Pressure	110 bars
Injection rate	30 kg/s
Relative permeability	van Genuchten-Mualem
Liquid phase residual saturation	0.2
Gaseous phase residual saturation	0.05
van Genuchten exponent	0.4
Capillary pressure	van Genuchten-Mualem
Entry pressure	3.58 kPa

The parameters used to setup the computational domain are summarized in Table 4.4

Table 4.4 Simulation parameters for the generalized 9-layered model

Vertical discretization type	Successively decrease with ratio 1.1 from 5 m for the bottom sandstone layer; 5 m uniform for the others
Boundary conditions	"No flow " condition on all boundaries

CO_2 injection is assigned as a point source at the middle of the bottom-most sand layer. Figure 4.15 shows the layered structure and computational mesh of the modeled Utsira formation as well as the location of CO_2 injection.

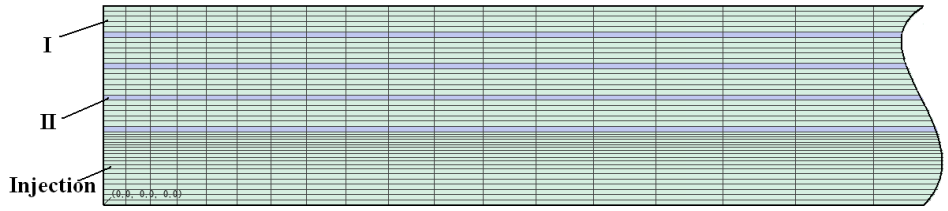

Figure 4.15 Computational mesh and layered structure of the generalized 9-layered model of Utsira formation

A steady-state simulation is first completed to provide initial conditions of equilibrium for successive simulations. The simulation time is set at 15 years and CO_2 plume profile is examined for each year. Figure 4.16 shows the cross-sectional view of gaseous CO_2 in the reservoir for 10 consecutive years since the inception of the injection.

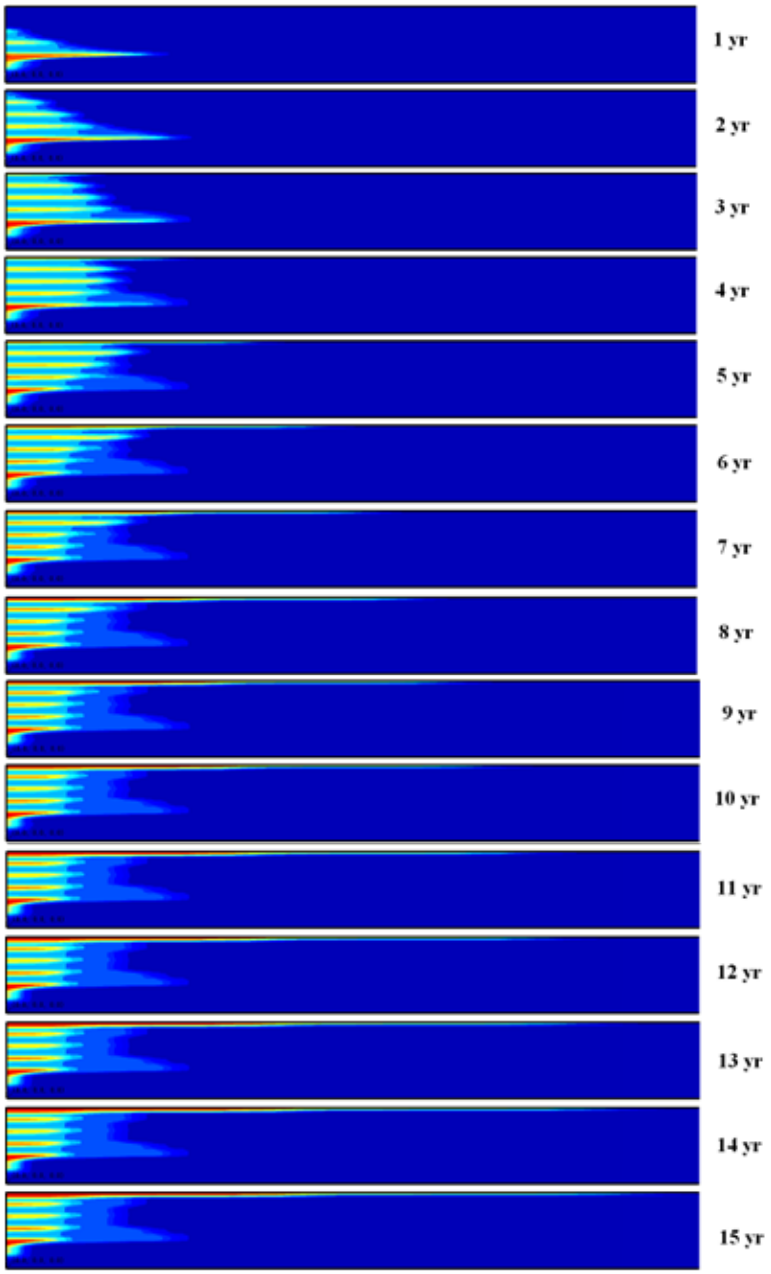

Figure 4.16 In situ CO_2 distribution for 15 years of injection

Results shown in Figure 4.16 provide evidence of strong secondary sealing effect for migration of in situ CO_2. Similar to the case of Mt. Simon SAGCS, the injected CO_2 first migrates upwards driven by buoyancy until it gets in contact with the first shale layer. Due to the low permeability and high capillary entry pressure, CO_2 is confined by this shale layer and is forced to migrate radially. Simultaneously, CO_2 concentration

builds up beneath the shale layer and finally breaks through the capillary barrier upon sustaining sufficient CO_2 column height. The accumulation-penetration-breakthrough takes place each time the CO_2 plume encounters a new shale layer and forms an upside-down pyramid shaped sub-plume as documented clearly by the first and second year plume shapes in Figure 4.16. Due to the secondary sealing effect, in situ CO_2 has very limited contact with the caprock of Utsira formation by the third year of injection. These results are generally consistent with the field seismic images of Sleipner project shown in Figure 4.17.

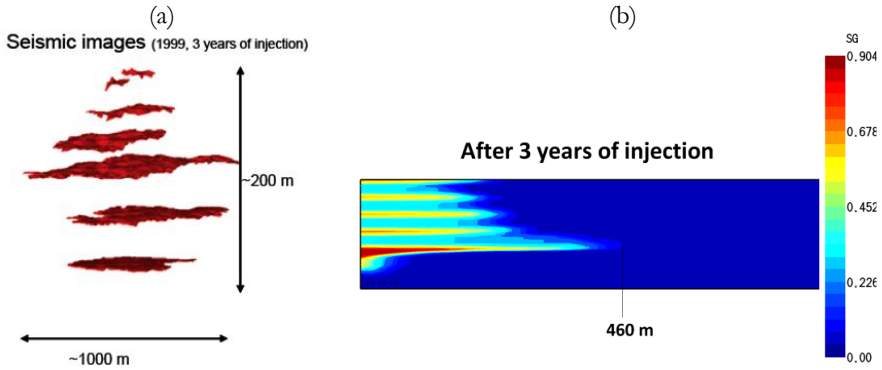

Figure 4.17 CO_2 distribution in Utsira formation after 3 years of injection, a) seismic image [48], b) TOUGH2 simulation

From the seismic image, it can be seen that the radius of the largest CO_2 subplume is approximately 500 m. It also shows the upside-down pyramid-shaped plume, and very limited CO_2 concentration in the topmost sandstone layer. Similar to the seismic image, our simulation also shows a 460 m in radius of the largest CO_2 sub-plume, and very limited existence of CO_2 in the topmost sandstone layer at the end of three years of injection. However, it should be noted that our simulation gives slight overestimation of upward migration of in situ CO_2, resulting in the oversized plume in the topmost layer. This is probably an unavoidable result due to the simplification of employing axisymmetric cylindrical model. Such overestimation in the early years can also be explained by recalling that the actual injection rate has increased from a lower value at the beginning to a relative steady rate of 1 Mton/year in later years [49], while in our

simulation a uniform injection rate of 1 Mton/year is implemented from the beginning of the simulation.

Additionally, ten-year CO_2 flux analysis has been made for the topmost sandstone layer (Layer #9) since it is critical to identify the accumulation of CO_2 underneath the caprock. As shown in Figure 4.18, excellent agreement between our simulation and the seismic amplitudes analysis [49] is observed, suggesting the overall accuracy of our modeling despite some of the discrepancy at detailed level. The flux analysis shown in Figure 4.18 also implies that the accumulation rate of CO_2 in the topmost sandstone layer tends to increase until it becomes stabilized. The fact can be explained by the mechanism of secondary sealing effect.

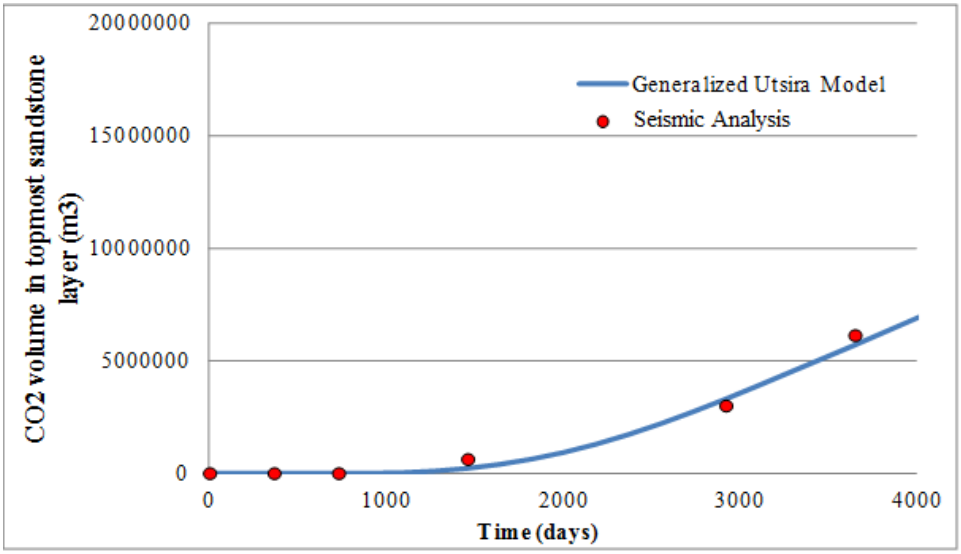

Figure 4.18 Gaseous CO_2 accumulation in the topmost sandstone layer

4.3.2 Model #2 – Detailed 3D Model of Utsira Layer #9 Formation

In situ CO_2 possesses strong potential to migrate upward due to buoyancy, and thus accumulates under the caprock unless capillary barrier is compromised. Previous experience has demonstrated that the accumulation of CO_2 under the caprock occurs in a relatively short period compared to the entire time span of SAGCS project, and it is a

major concern for storage security. Therefore, it is critical for a SAGCS project to identify the accumulation of CO_2 and its tendency of migration underneath the caprock. With such information available, precautionary treatments could be deployed to avoid potential leakage. Utsira formation near the injection site has been identified as a 9-layer structure as shown in Figure 4.12. The topmost sandstone layer, Layer #9, is of most interest since it has the highest concentration of gaseous CO_2 and has direct contact with the overlying caprock formation. Seismic survey has shown striking growth of CO_2 accumulation in Layer #9 between 1999 and 2006 as shown in Figure 4.19.

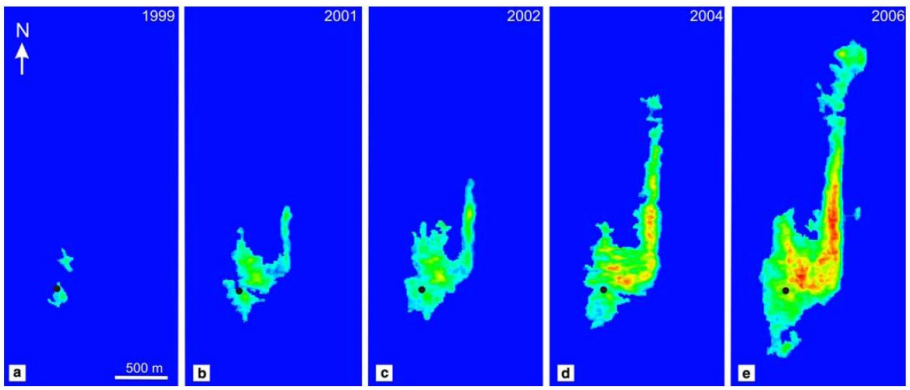

Figure 4.19 Amplitude maps of Layer #9 from 1999 to 2006 [47]

The black dot in Figure 4.19 marks the location of the injection well, which is roughly 200 m under Layer #9. Two distinct local CO_2 accumulations appeared after about three years of injection (recall that injection began in 1996), indicating CO_2 began to accumulate under the caprock. However, CO_2 migration in Layer #9 was not symmetric due to the topography of the caprock. The northward migration of initially impacted CO_2, seen as the "body" of the plume in Figure 4.19, implies a local topographic dome; a prominent north-trending migration, seen as the "finger" of the plume in Figure 4.19, implies the spill of locally structural trapped CO_2 along a north-tending topographic ridge. CO_2 migration along the north-tending ridge was rather fast at about 1 m/day between 2001 and 2004 [47].

In order to examine the plume evolution within the topmost layer more closely, a 3D model of Utsira Layer #9 is created with detailed topography. It should be noted that

only Layer #9, not the entire depth, is modeled because of the following considerations. To ensure the accurate capture of topographic effect on plume shaping, computational domain with considerable fine mesh resolution has to be modeled based on geological survey data. The computational effort and thus the feasibility of highly detailed model of the entire Utsira formation is very intensive and time consuming. Secondly, CO_2 has to breakthrough several layers of relatively low permeability shale prior to reaching the topmost layer. While it is difficult to questionable to quantify the breakthrough of gaseous CO_2, the quantification of CO_2 feeding into the topmost layer (Layer #9) is rather reliable. Therefore, a model of only the topmost layer (Layer #9) could provide an ideal platform to investigate the effect of various parameters such as topography on the shaping of CO_2 plume, as well as for optimization for high efficiency sequestration while maintaining an affordable computational cost.

A reservoir model with dimension of 1600 m × 4900 m and varying thickness was constructed. It covers the portion of Utsira formation where the plume shown in Figure 4.19 resides. As mentioned earlier, the topography of this portion of Utsira formation is accurately modeled based on seismic geological survey data (provided by Zhu and Lu of the University of Indiana [50],[51]) with 50 m × 50 m mesh resolution. Because only Layer #9 is modeled, the thickness of computational domain varies from 3.5 m to 26.3 m with an average thickness of 11.3 m. However to accurately capture the accumulation and upward and lateral movement of CO_2, 37 layers are used along the thickness. The topmost layer and the bottom two layers are designated to represent the low permeability shale, while the 34 layers in the middle are assigned the properties of mudstone. In the 3D Layer #9 model, permeability anisotropy is considered with west-east permeability of 2 Darcy, north-south permeability of 10 Darcy, and vertical permeability of 200 mDarcy. 3D overview of the Layer#9 model is shown in Figure 4.20.

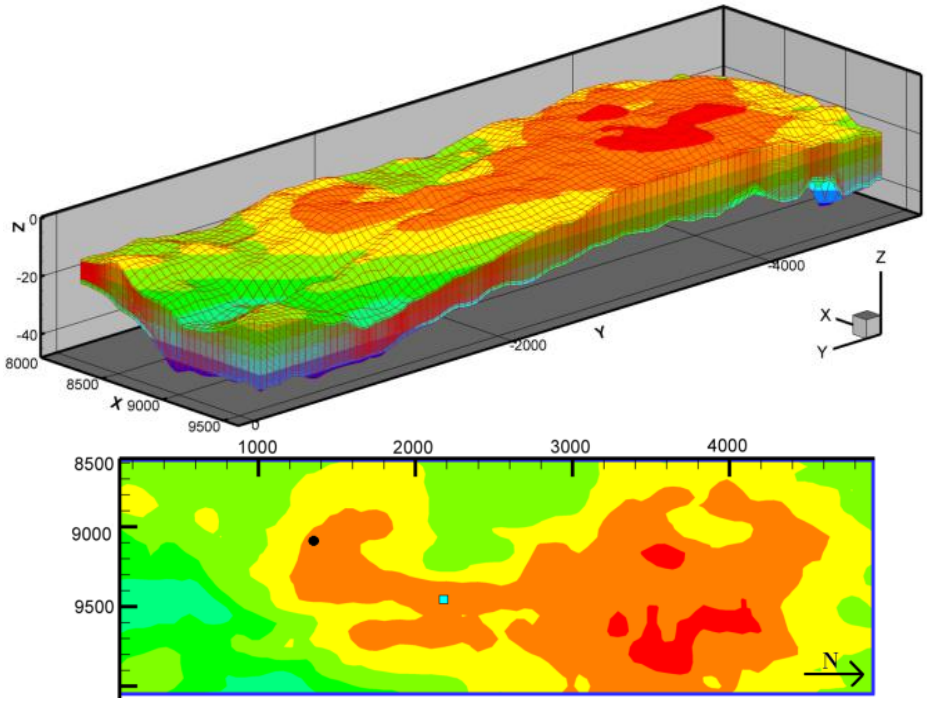

Figure 4.20 3D overview and plan-view of the 3D Layer #9 model of Utsira indicating feeder locations (black dot: main feeder; cyan square: secondary feeder)

Table 4.5 summarizes hydrogeological properties of the Layer #9 model.

Table 4.5 Hydrogeological properties for the Utsira Layer#9 model

Temperature	33 °C
Pressure	8.6×10^7 Pa
Total Utsira formation area	26100 km^2
Total Utsira formation thickness	50 m ~ 300 m
Layer#9 area	1600 m × 4900 m
Layer#9 thickness	3.5 m ~ 26.3m
Shale permeability	W-E: 0.001 mDarcy, N-S: 0.001 mDarcy, Vertical: 0.0001 mDarcy
Mudstone permeability	W-E: 2 Darcy, N-S: 10 Darcy, Vertical: 200 mDarcy
Utsira porosity (shale/mudstone)	35.7 %
Residual CO_2 saturation	0.02
Residual brine saturation	0.11
Relative permeability type	Corey/van Gunochen-Muller

Capillary pressure	none
Porewater salinity	3.3 %
North-south geological gradient	0.0082 m/km, 0.0058 m/km
CO_2 feeder location	Main feeder: W-E: 516 m, N-S: 1210 m, Bottom mudstone Secondary feeder: W-E: 925 m, N-S: 2250 m, Bottom mudstone
Boundary conditions	No flow on top and bottom boundaries, Fixed state on four lateral boundaries

It should be noted that in the 3D Layer #9 model, the source of CO_2 is identified as "feeder" but not "injector" to emphasize that CO_2 is supplied from the lower aquifer through leakage pathways rather than by direct injection. Since the actual CO_2 injector is located at about 200 m under Layer #9, information of injection rate recorded at the injector is not applicable for the CO_2 feeders in Layer #9 model. To determine the CO_2 feeding rate to Layer#9, seismic surveys of CO_2 distribution are used to obtain its volume under in situ conditions, and then converted to mass flow rate. Information of CO_2 accumulative mass provided by Zhu and Lu [51] is summarized in Table 4.6.

Table 4.6 Accumulative CO2 mass in Layer #9, 1999-2008

Year	Accumulative Mass (kg)	Yearly Feeding Mass (kg)	Feeding rate (kg/s)
1999	0.00	0.00	0.00
2000	1.82×10^7	1.82×10^7	0.577
2001	5.52×10^7	3.70×10^7	1.17
2002	9.49×10^7	3.97×10^7	1.26
2003	1.45×10^8	5.01×10^7	1.59
2004	2.13×10^8	6.80×10^7	2.16
2005	3.07×10^8	9.40×10^7	2.98
2006	4.34×10^8	1.27×10^8	4.03
2007	6.03×10^8	1.69×10^8	5.36
2008	8.20×10^8	2.17×10^8	6.88

Table 4.6 gives the CO_2 accumulation in Layer #9 from 1999 to 2008. It can be seen that CO_2 feeding rate to Layer #9 keeps on increasing for the recorded nine years as shown in Figure 4.21. Recalling the analysis of secondary sealing effect given for the previous cases, it is the pressure gradient between the gaseous CO_2 phase pressure at lower aquifer and the capillary pressure of the overlying shale layer that determines the

breakthrough of CO_2 and its flow rate. When breakthrough first occurs, the pressure gradient just breaks the equilibrium state, resulting in relatively low breakthrough mass flux to Layer #9. However, as more CO_2 accumulates, the pressure gradient gradually increases and leads to increasing breakthrough mass flux as depicted in Table 4.6 and Figure 4.21. A nine-year average feeding rate of about 2.89 kg/s can be obtained from Table 4.6 and Figure 4.21. In the following simulations both the nine-year average value and the values in Table 4.6 have been used.

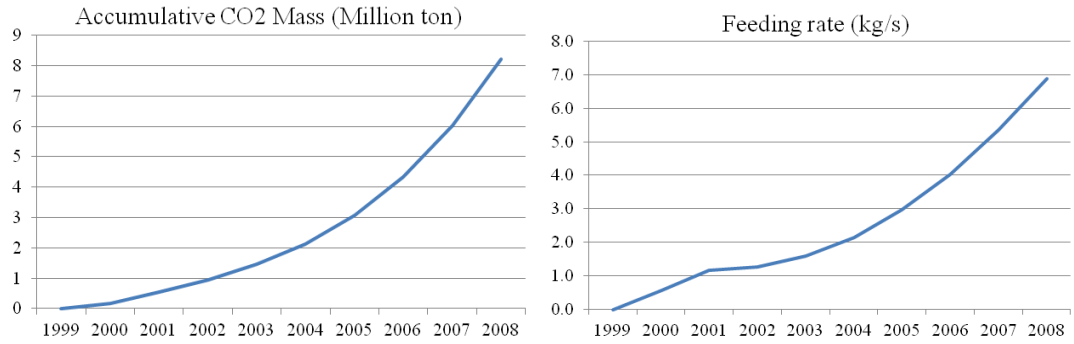

Figure 4.21 CO_2 mass accumulation and feeding rate in Layer #9

The significant north-tending plume finger is rather perplexing for regular pressure-gradient driven Darcy flow. Analysis suggests three possible explanations to the cause of prominent north-tending CO_2 fingering along the ridge, which are: 1) significantly higher permeability applied to the ridge; 2) existence of north-south geological updip which enhances the buoyancy-drive migration along the ridge; and 3) existence of a secondary (or even multiple) CO_2 pathway under the ridge. The hypothesis of significantly higher permeability at the ridge can be easily ruled out since no such evidence is obtained from the geological survey. It is still under debate whether geological updip should be considered when analyzing the CO_2 migration in Utsira formation. Chadwick and Noy's work [47] has suggested two possible geological gradient values based on the detailed seismic image of the cross-section of the Utsira formation (Figure 4.22). By looking at the feeder chimney impact point A1 and a local topographic culmination north of the ridge, point A2, an average gradient value of 8.2 m/km can be evaluated. A more conservative estimate of caprock dip may be obtained

by comparing the relative elevations of the southernmost and northernmost extremities of the layer, points B1 and B2 respectively, which gives an average gradient value of 5.8 m/km.

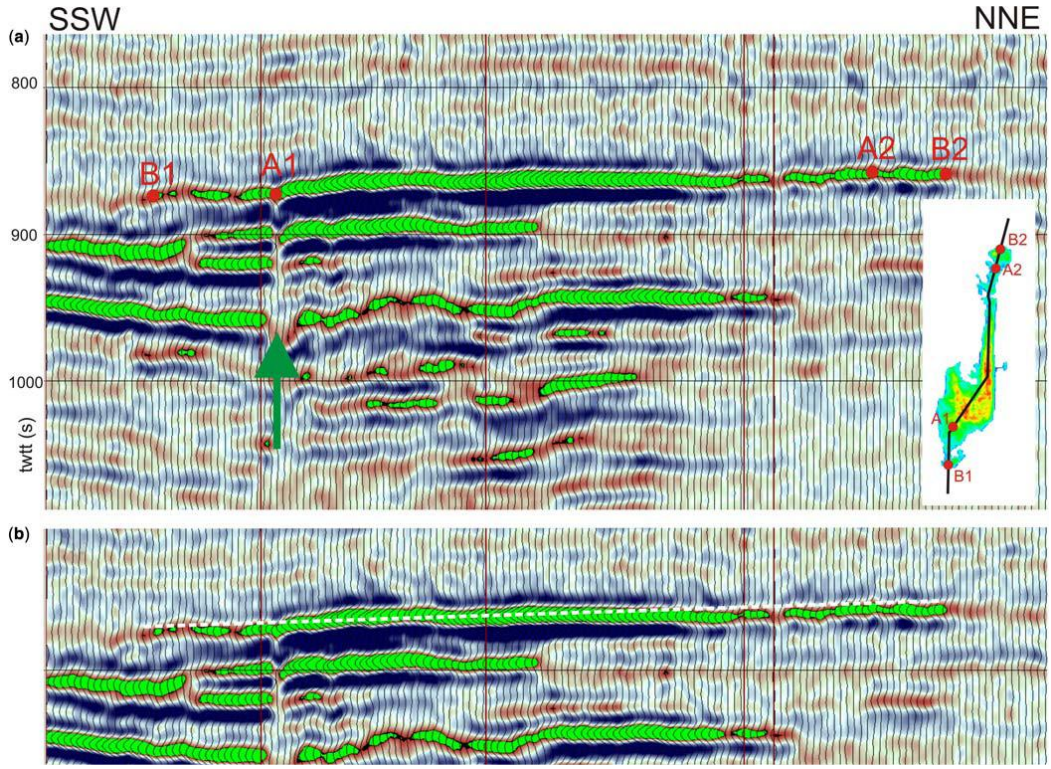

Figure 4.22 Seismic line through the CO_2 plume (a) detailed geometry in two-way travel-time. The main feeder chimney (arrowed) supplies the layer at point A1; (b) deviation of the topmost layer from planar geometry (white dots). Reflective CO_2 layers in green.

Considering all the uncertainties mentioned above, a total of nine simulations are performed as summarized in Table 4.7. The simulation time is set at nine years, which corresponds to the injection period of 1999~2008. CO_2 plume migration at the topmost layer is examined for each year. The objective of the series of nine simulation runs is to obtain the best history matching to the filed seismic images, and therefore to provide insights into modeling uncertainties. In addition, the case with best history matching is used for optimization studies in Chapter 5.

Table 4.7 Nine simulation runs for the 3D Layer #9 model of Utsira

	Feeder(s)	Feeding rate	Updip	Boundary Cond.	Reservoir Temp.
1	Single	9-year average	No	Open	33 °C
2	Single	Time-dependent	No	Open	33 °C
3	Single	Time-dependent	0.0058	Open	33 °C
4	Single	Time-dependent	0.0082	Open	33 °C
5	Two	9-year average	No	Open	33 °C
6	Two	Time-dependent	No	Open	33 °C
7	Two	Time-dependent	No	Semi-open	33 °C
8	Two	Time-dependent	No	Semi-open	36 °C
9	Two*	Time-dependent	No	Semi-open	36 °C

*: main feeder location modified

The seismic images of CO_2 migration within Layer #9 from 1999 to 2008 are provided by Chadwick and Noy (Figure 4.19 [47]) and Singh et al. (Figure 4.23 [49]).

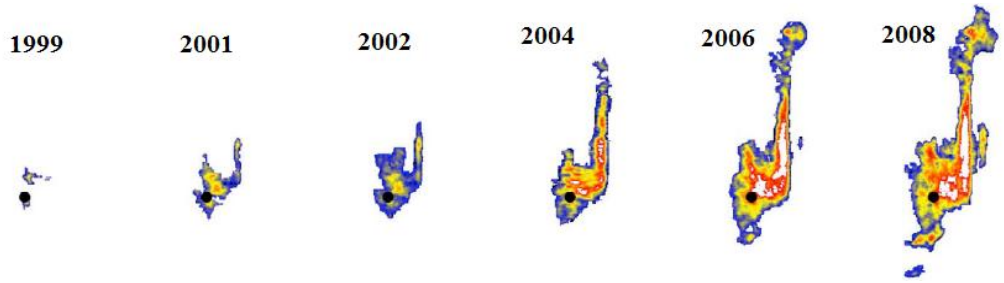

Figure 4.23 CO_2 migration in Layer #9, 1999-2008 [49]

Because Zhu and Lu group has conducted simulation studies over the same domain with similar hydrogeological properties, their simulation results as presented in Figure 4.24 are also considered for cross-comparison purpose.

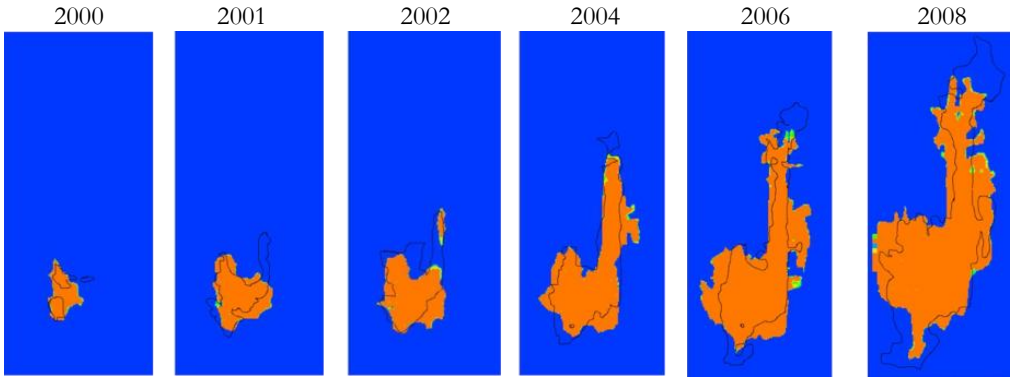

Figure 4.24 CO_2 migration simulation in Layer #9, 2000-2008 [51]

As motioned above, a total of nine cases have been considered before satisfactory history-matching can be obtained.

Case#1: Single feeder with 9-year average feeding rate, no geological updip

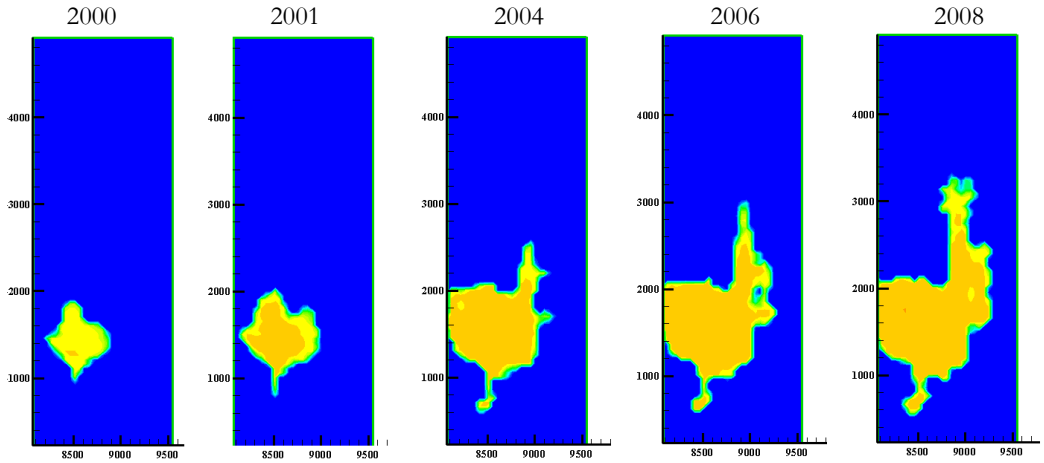

Figure 4.25 CO_2 migration in Layer #9, 2000 ~ 2008, case #1

In Figure 4.25, the CO_2 plume migration develops in a seemingly isotropic fashion at early stage. Then local migration of CO_2 along the north-trending ridge is captured in the simulations, as well as the small amount of spill southward. However, two major issues need to be addressed. First, plume size is significantly overestimated, especially for 2000 and 2001. Secondly, northward CO_2 migration along the ridge, which just reaches y = 3000 m by 2008 in the simulation, is greatly underestimated. This is over 10% under estimation comparing to the 3400 m migration captured by seismic imagine. In addition, CO_2 plume also appears to migrate too fast along the east-west direction.

Case#2: Single feeder with Zhu's feeding rate, no geological updip

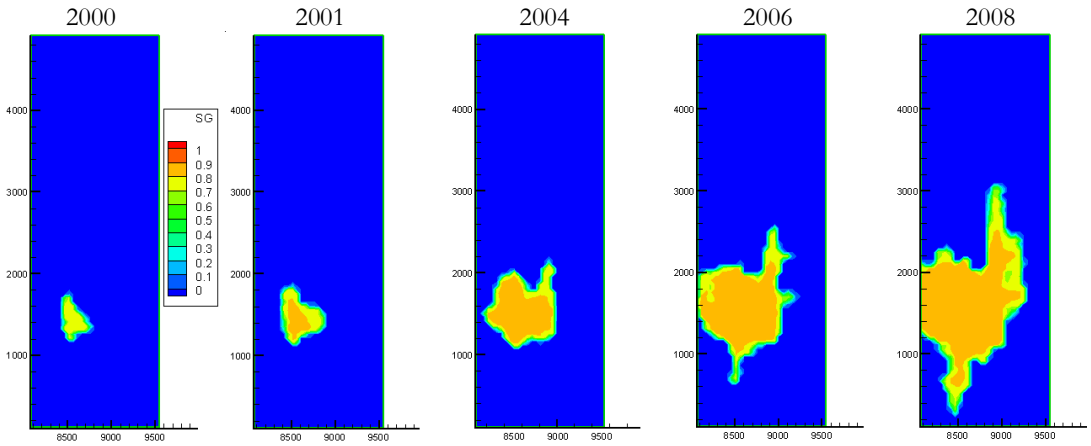

Figure 4.26 CO_2 migration in Layer #9, 2000 ~ 2008, case #2

Time-dependent injection scenario is introduced to the simulation in case#2. Because of the more realistic injection scenario, plume size at early stage is greatly improved, resulting into good match with the history data. However, the issue of underestimation of CO_2 northward migration along the ridge becomes worse, due to the essentially lowered major driving force of CO_2 migration – the pressure gradient between the feeder and the ambient aquifer. Therefore, less amount of CO_2 is "pushed" to the north-trending split ridge in the same given time. Although the pressure gradient gradually escalades with the increase of feeding rate, the migration along the ridge is still compromised due to insufficient migration duration. Additionally, the southern CO_2 spill seems to be overestimated for year 2008. Exaggerated east-west migration still remains.

Comparison of Figure 4.25 and Figure 4.26 implies the necessarity of implementing the time-dependent CO_2 feeding rate for match plume migration at the early years. However, the issues of underestimation of north-trending split and overestimation of the southern split remain unaddressed.

Case#3: Single feeder with Zhu's feeding rate, 5.8 m/km geological updip

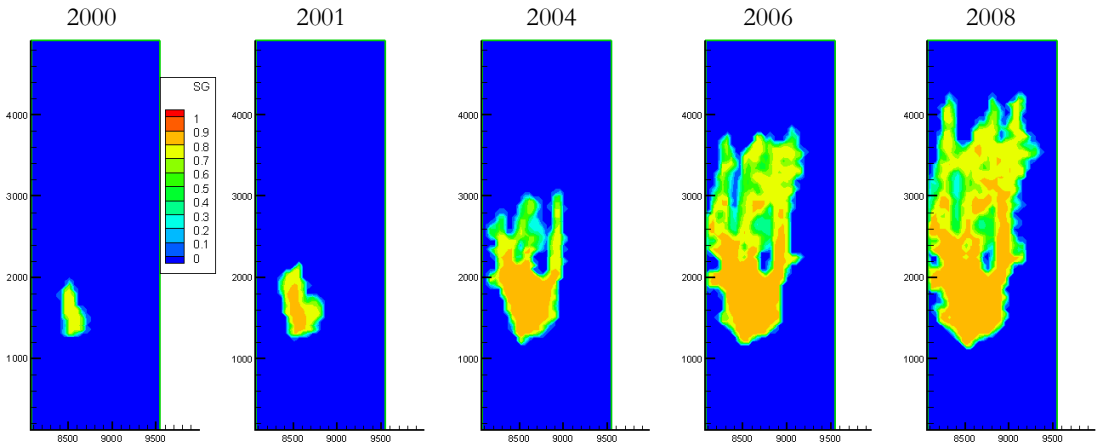

Figure 4.27 CO_2 migration in Layer #9, 2000 ~ 2008, case #3

Case#3 provides some insights of plume migration under the consideration of possible geological gradient. In this simulation, a conservative north-south gradient of 5.8 m/km is applied while all other conditions are kept identical to those for case#2. As seen in Figure 4.27, the plume differs drastically from the seismic imagine and previous simulation results since 2004. Instead of being spilt along the north-trending ridge, majority of CO_2 is split out of the local dome, where the feeder locates, directly to the north. It suggests that the variance in depth of the caprock is relatively small (actually in the order of centimeter per meter span) of Utsira formation, and thus the CO_2-water contour can be easily altered by other parameters, such as small geological updip or higher feeding rate, as demonstrated in case#4.

Case#4: Single feeder with 9-year average feeding rate, 8.2 m/km geological updip

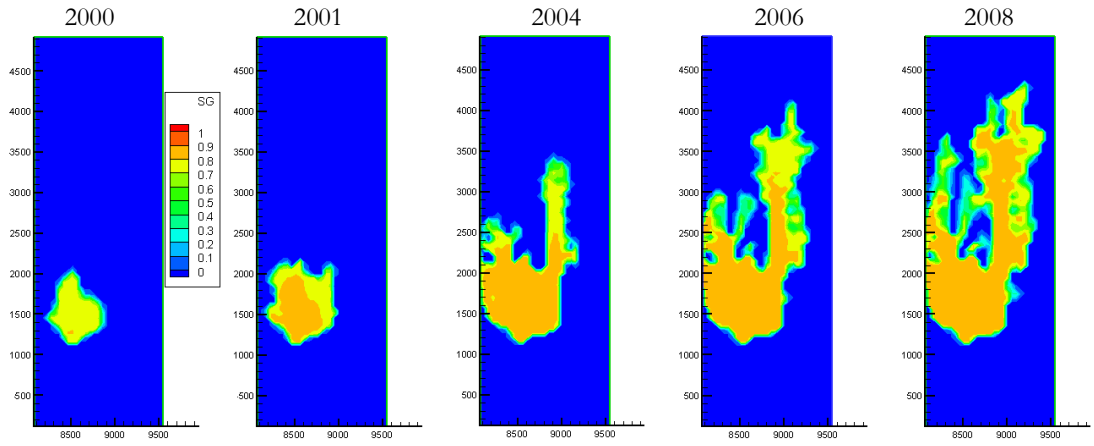

Figure 4.28 CO_2 migration in Layer #9, 2000 ~ 2008, case #4

Case#4 serves as a comparison of case#3 and demonstration of its conclusions. A more aggressive geological updip of 8.2 m/km is applied to the model. In addition, the 9-year average injection rate, which is considerably higher than the time-dependent injection scenario for early years, is used. From Figure 4.28 great enhancement of plume migration along the north-trending ridge can be observed. However, the direct CO_2 split on the north side of the local dome also gets worse. Although under steeper north-south dip, such unrealistic split is still improved a bit by the greater eastward movement of plume induced by the greater feeding rate. The results of case#3 and case#4 suggest that the inclusion of geological updip could potentially help a lot to enhance the plume migration along the north-trending ridge. Nevertheless, it is critical of carefully tuning up modeling parameters, such as gradient of updip, feeder location, feeding rate, computational mesh resolution, to avoid unrealistic local split of CO_2. Since the existence of geological updip is not strongly supported either from geology surveys or corresponding simulations, such scenario is ruled out in further simulations.

Case#1 through case#4 suggest that a single feeder is not likely to lead to sufficient plume migration along the north-tending ridge due to the lack of driving force. Moreover, the assumption of north-south geological gradient tends to cause unrealistic over flow of CO_2 and failed to predict the moderate southern split. Therefore, the

possibility of having an additional feeder near the ridge is investigated. According to Zhu and Lu's suggestion [51], the location of the secondary feeder is set as x=8925 m, y=2210 m, as shown in Figure 4.20. Additionally, it is assumed that 100% of CO_2 is distributed by the main feeder during 1999 to 2001; 85% of CO_2 is distributed by the main feeder while the rest 15% is distributed by the secondary feeder for 2001 and on. It is worth noticing that the assumption of having two CO_2 feeders is theoretically sound. Since CO_2 enters Layer #9 by breakthrough the capillary barrier of lower formations, there remains good chance of having multiple CO_2 pathways from the lower aquifers due to the heterogeneity in formation properties. As the third hypothesis of enhancing CO_2 northward migration along the ridge, having a second feeder right under the north-trending ridge is investigated in case #5 to case #9. Geological updip is no longer considered for all the following cases due to the induced regional over-spill.

Case#5: Two feeders with 9-year average feeding rate, no geological updip

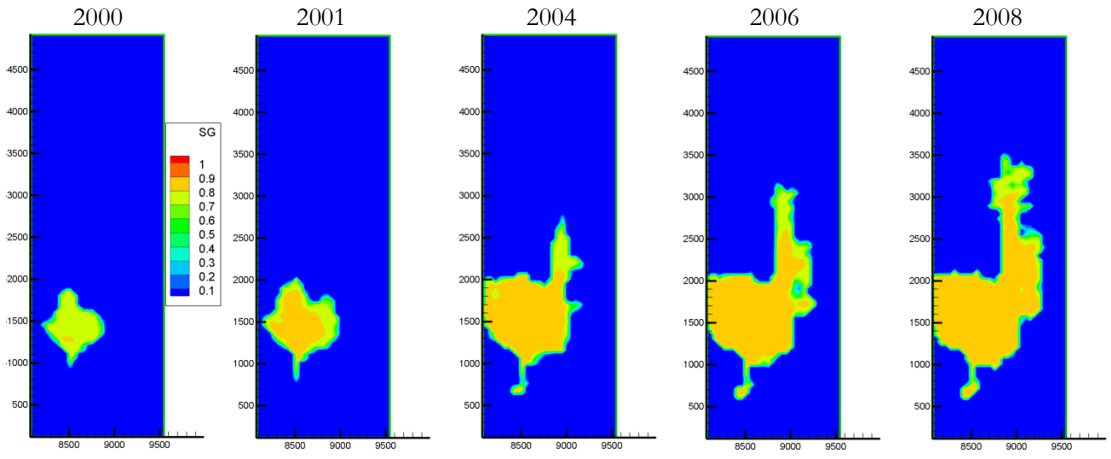

Figure 4.29 CO_2 migration in Layer #9, 2000 ~ 2008, case #5

Figure 4.29 gives the simulation results under two feeder scenario with 9-year average feeding rate. Comparing to single feeder scenarios, plume migration along the north-trending ridge has been improved as expected. However, overestimation of plume migration at early stage still occurs, as CO_2 feeding from the secondary feeder is inactive during the early stage. Additionally, the overestimated west-east plume movement still persists.

Case#6: Two feeders with time-dependent feeding rate, no geological updip

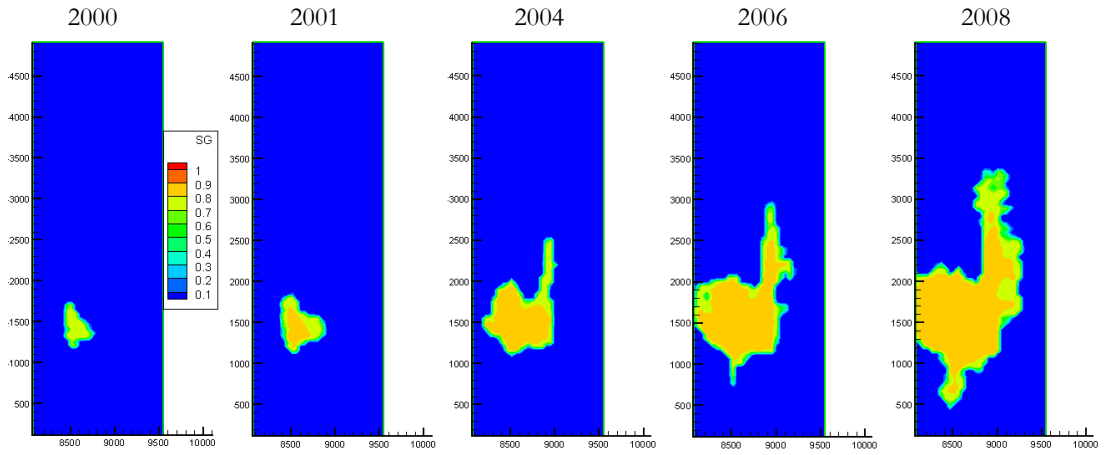

Figure 4.30 CO_2 migration in Layer #9, 2000 ~ 2008, case #6

Time-dependent feeding scenario is applied for the two feeder case #6 as its crucial role to accurate capture of CO_2 migration at early years has been demonstrated in case#2. In Figure 4.30, early stage migration is well captured, and plume along the north-trending ridge at later years has been greatly improved comparing to that of case#2. Nevertheless, a close comparison with the field data suggests additional work need to be done to treat the overestimated west-east migration and further enhancement of the northward migration along the ridge. To address these issues, first the boundary condition is modified. Closed boundary condition is applied to the western and eastern lateral boundaries, while open condition is maintained at northern and southern lateral boundaries. Such modification makes the reservoir model semi-open, and it is expected to lead to less west-east migration since pressure gradient in that direction is reduced. Recalling that the total amount of CO_2 feeding is identical, reduced migration along east-west direction will force more CO_2 to migration along the north-south direction.

Case#7: Two feeders with time-dependent feeding rate, no geological updip, semi-open boundary condition

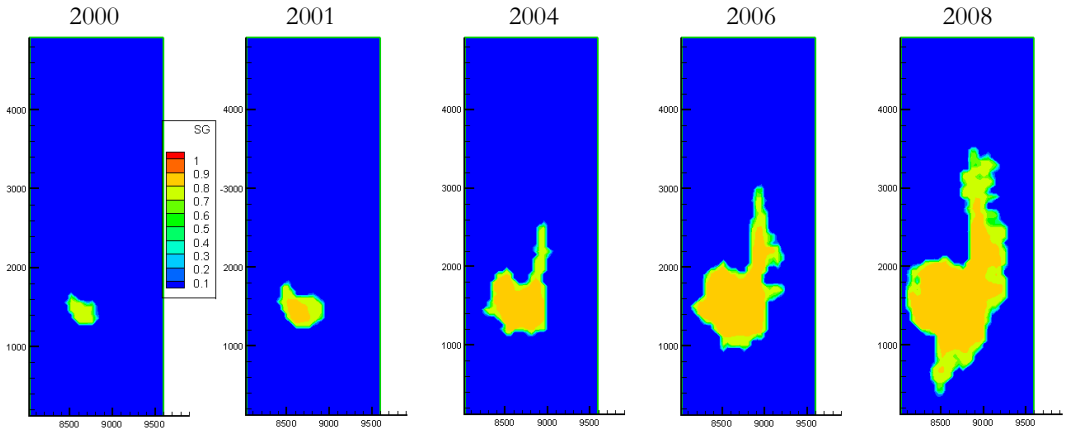

Figure 4.31 CO_2 migration in Layer #9, 2000 ~ 2008, case #7

As can be seen in Figure 4.31 the implementation of semi-open boundary condition reduces east-west plume migration effectively, and simultaneously enhances northward migration along the ridge. However, its attempt of close matching with the seismic imagines still remains unsuccessful, implying the missing of some other key aspects in modeling.

As analyzed earlier, the only two types of driving force for plume migration are pressure gradient and buoyancy. Applying semi-open boundary condition is essentially to enhance pressure gradient. On the other hand, a more intuitive way to enhance buoyancy is to decrease CO_2 density. In the previous simulations, given reservoir conditions lead to pure supercritical CO_2 density of about 630~650 kg/m^3. However, an interesting fact comes to our attention when reviewing the literature. The injected gas for Sleipner SAGCS project is not pure supercritical CO_2, but a 98% CO_2 and 2% methane mixture [49]. Because methane is significantly lighter than CO_2, it is expected to migrate up and concentrate in the Layer #9 faster than CO_2. With the concentration of methane, it will effectively lower the density and increases the buoyancy of the CO_2-methane mixture. Since TOUGH2 does not possess the capability of modeling CO_2-methane mixture in saline aquifer, a workaround of compensating the density lost of pure CO_2 is to increase the reservoir temperature. According to Zhu and Lu's

suggestions the density of CO_2-methane mixture falls into the range of 600 kg/m^3 [51]. Retaining other reservoir conditions, it requires a raise of 3 °C in reservoir temperature to give a pure CO_2 density comparable with that of the CO_2-methane (2%) mixture at actual reservoir conditions. The increased reservoir temperature will also cause drop of porewater's density and viscosity, which, however, is negligible comparing to that of CO_2. Therefore, reservoir temperature is increased from 33 °C to 36 °C to enhance the mobility of in situ CO_2.

Case#8: Two feeders, time-dependent feeding rate, no geological updip, semi-open boundary condition, increased reservoir temperature

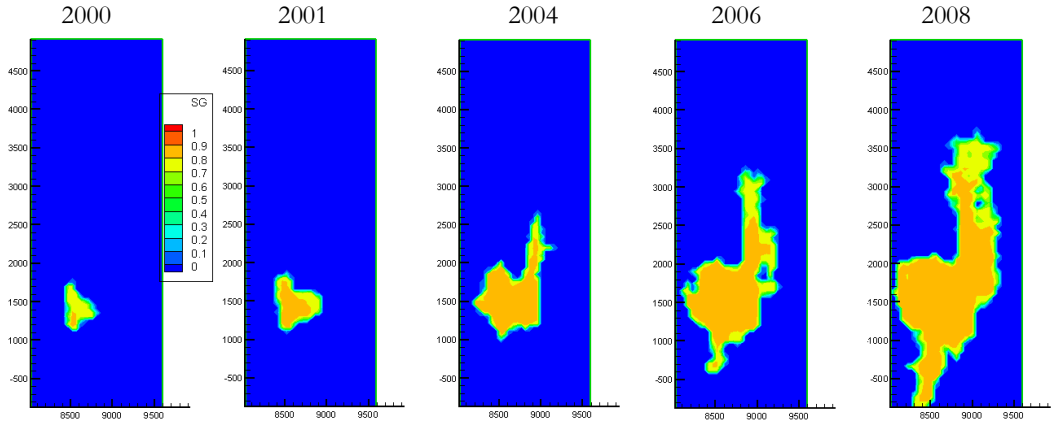

Figure 4.32 CO_2 migration in Layer #9, 2000 ~ 2008, case #8

Seen from Figure 4.32, the increased reservoir temperature greatly enhanced plume migration in north-south direction as expected. Meanwhile, east-west migration is still well confined by the semi-open boundary condition. In Figure 4.32, the plume shape at each time matches very well with the corresponding seismic imagine. The northeast migration reaches about y = 3300 m at 2006, which is the same ballpark as the seismic imagine. The only concern is that the southward migration seems to be overestimated at 2008. It is possibly that increased buoyancy leads to the over-spill to the south.

Case#9: Two feeders, time-dependent feeding rate, no geological updip, semi-open boundary condition, increased reservoir temperature, modified main feeder location

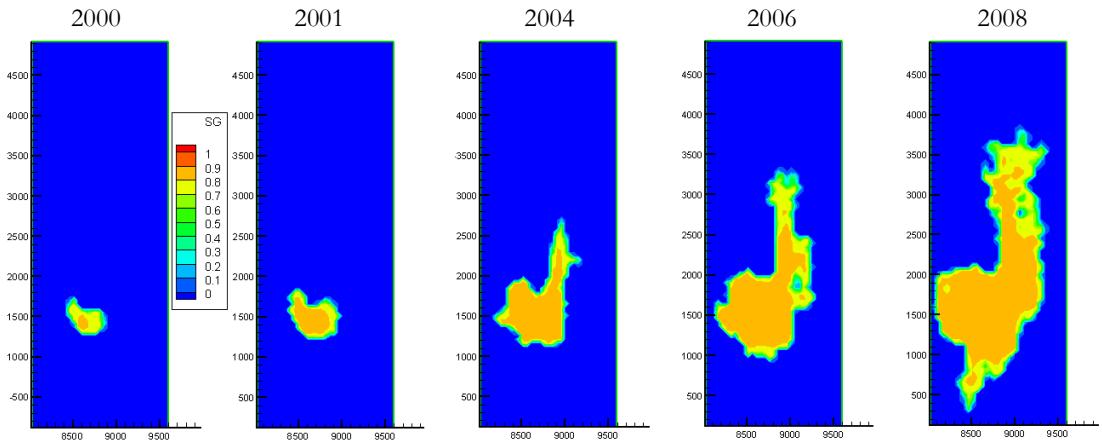

Figure 4.33 CO_2 migration in Layer #9, 2000 ~ 2008, case #9

To treat the over-split of CO_2 to the south after 2006, the main feeder is relocated 100 m to the east and 200 m to the north. As seen in Figure 4.33, CO_2 over-split to the south is avoided by the slightly modified main feeder location. Case#9 gives satisfactory results to match both the seismic imagines (Figure 4.19 and Figure 4.23) and other group's simulations (Figure 4.24).

Both the 2D generalized Utsira formation model and the 3D detailed Layer #9 model have generated satisfactory simulation results for history-matching. As summary, five major implications can be made as follows. First, it shows that permeability anisotropy should to be accurately modeled. Vertical-to-horizontal anisotropy of 10:1 has to be modeled to accurately capture the upward migration of CO_2. Horizontal anisotropy of 2:10 has to be modeled to capture the northern split of CO_2 into the north-tending ridge. Secondly, a secondary feeder is likely to exist directly under the north-tending ridge to generate sufficient plume migration along the ridge. It suggests multiple pathways of CO_2 breakthrough from the lower aquifer structure. Thirdly, the fact that injection gas being CO_2-methane mixture is very important in modeling since the presence of methane essentially enhances the buoyancy. Fourthly, it is critical that time-dependent CO_2 injection is modeled. This is consistent with the behavior of CO_2 path

flow breaking the capillary pressure barrier, as is noted for the secondary-sealing effect in case of Mt. Simon formation. And last, simulation results suggest strong mobility of gaseous CO_2 under the caprock (shale) without major leakage into it, implying that the caprock serves well as non-permeable CO_2 barrier while exerting little resistance on the lateral flow beneath it.

The simulation studies of the three identified deep saline aquifers conclude the first part of this dissertation. Asides the important insights and implications obtained by these simulations, it is also encouraging to implementing innovative reservoir technique and its optimization for more efficient and secured SAGCS operations. Such work is to be presented in the following sections of this dissertation.

Chapter 5

Geological Carbon Sequestration Optimization in Saline Aquifer

The development of GA-TOUGH2 code and the successful simulation studies of GCS in large scale saline formations has encouraged us to study the optimization of some promising reservoir engineering techniques for more efficient and secured SAGCS practices. These optimization study include (but not limited to) the optimization of the constant-gas-injection rate for maximum CO_2 dissolution, the optimal design of water-alternating-gas (WAG) injection scheme (pattern) for maximum storage efficiency, the design of optimum injection scenario for optimal pressure management, and the optimal placement of well in a multi-well injection system.

5.1 Optimization of CO_2 Dissolution for Constant Gas Injection Rate: Validation of GA-TOUGH2 against the Brute-force Approach

It is a conventional practice to inject supercritical CO_2 into the saline aquifer at some constant volumetric flow rate. Variation in CO_2 density within the saline aquifer is usually negligible due to the relatively small thickness of the aquifer compared to its depth. Therefore, constant volume CO_2 injection can also be treated as constant mass CO_2 injection known as the constant-gas-injection (CGI). It is intuitive that CO_2

injection rate should be as high as possible to obtain a time-efficient operation. However, it has been noted in the literature that the quantity of short-term CO_2 dissolution is strongly affected by the injection rate; there is an optimal injection rate beyond which a larger injection rate may even lead to lesser amount of short-term CO_2 dissolution. The existence of an optimal injection rate is evident from a series of three simulations with low, moderate, and high injection rates as shown in Figure 5.1. A possible explanation for the decreased CO_2 dissolution associated with the high-rate injection is the high injection-induced pressure.

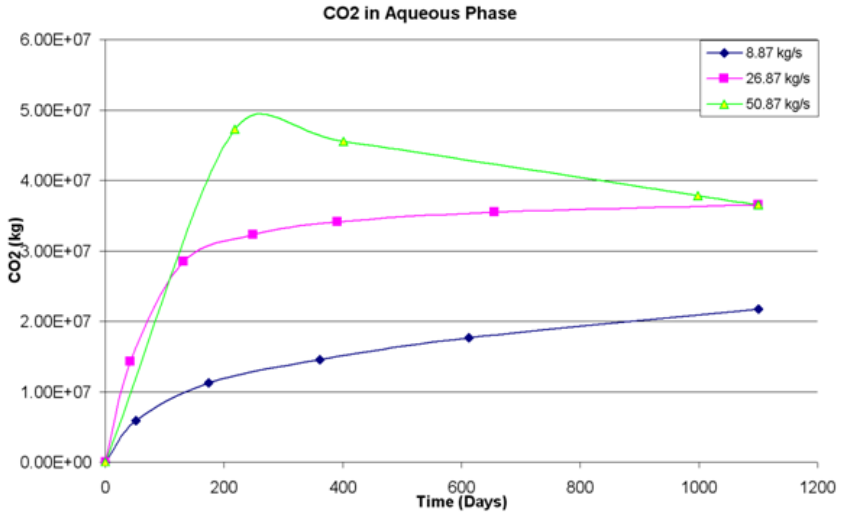

Figure 5.1 Short-term CO_2 dissolution for three injection rates

An optimization task for a generic aquifer model is conducted to validate GA-TOUGH2. In this task, the goal has been to optimize the amount of dissolved CO_2 in the aquifer after 2.5 years of injection by varying the injection rate. The domain dimensions are 100 m × 100 m × 60 m. The initial conditions are P=10^7 Pa and T=65 ^oC and closed boundary conditions are assumed. CO_2 injection is located at the bottom center of the aquifer. The search space for optimal injection rate is set between 0.01 kg/s to 2 kg/s. The optimization objective or the fitness function is the optimal amount of dissolved CO_2 in the aquifer after 926 days of injection. Since the only parameter allowed to change is the CO_2 injection rate, it is essentially a one-dimensional optimization problem.

The computational domain, GA-TOUGH2 optimization results with GA convergence history, and the brute-force results are shown in Figure 5.2.

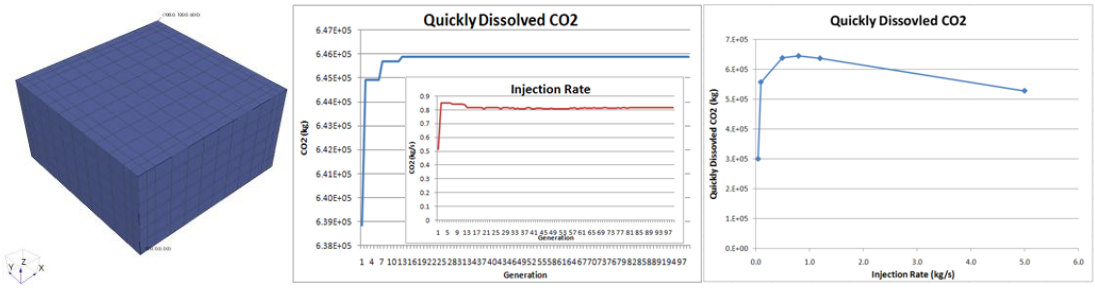

Figure 5.2 Computational domain, GA optimization convergence history, and brute-force method results for optimization of quickly dissolved CO_2

It can be seen from Figure 5.2 that GA optimization achieves its convergence after about 13 generations. For validation, brute-force optimization is manually performed. Table 5.1 provides comparison between the GA-TOUGH2 results and brute-force results; this simulation clearly validates the accurate optimization capability of GA-TOUGH2.

Table 5.1 Comparison of results between GA-TOUGH2 and brute-force method

	GA-TOUGH2	**Brute-force**
Max. short-term dissolved CO_2 after 926 days	645897 kg	645450 kg (at 0.8 kg/s injection)
Corresponding CO_2 Injection Rate	0.815 kg/s	~ to 0.8 kg/s

5.2 Optimization of CO_2 Plume Migration for Water-Alternating-Gas (WAG) Injection Scheme

A reservoir engineering technique known as water-alternating-gas (WAG) scheme is considered for SAGCS for improving the sequestration efficiency, although an additional injection of water with CO_2 will inevitably increase the cost. GA-TOUGH2 is employed to determine the optimal WAG operation for maximum CO_2 sequestration efficiency while minimizing the water usage.

5.2.1 Background of WAG Operation

The idea of WAG operation was originally introduced in the oil industry to improve the sweeping efficiency during gas flooding of the oil reservoir. A significant amount of remaining oil could be recovered by regularly injecting intermittent slugs of water and gas (usually CO_2), as shown in Figure 5.3. WAG operation has been widely applied to enhanced oil recovery since late 1950's.

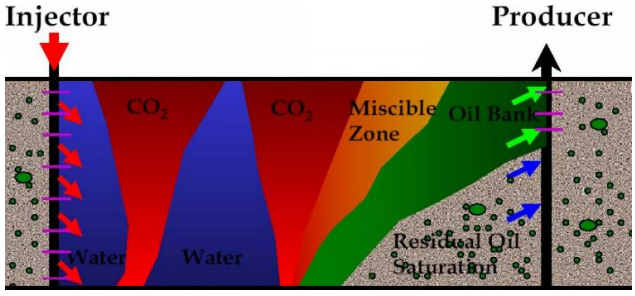

Figure 5.3 Schematic of the WAG injection for an oil reservoir

5.2.2 WAG Operation for SAGCS

Inspired by the practice in oil industry, it has been surmised by several investigators that intermittent injection of CO_2 and water could lead to better CO_2 storage efficiency by reducing the migration of CO_2 plume [52],[53], enhancing residual trapping [54], and accelerating the CO_2 dissolution [55],[57]. Figure 5.4 illustrates the schematic of various WAG operation schemes. The key idea is intermittent slugs of water and CO_2 injection.

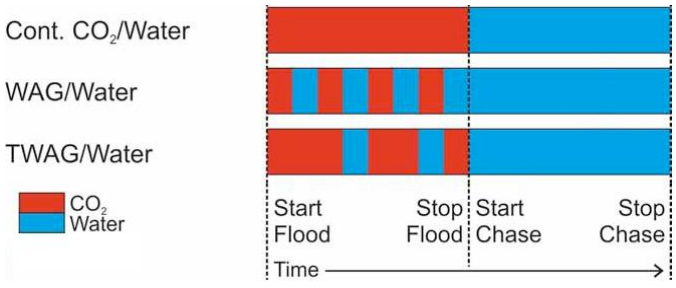

Figure 5.4 Schematic of various WAG operations

Improved (reduced) CO_2-brine mobility ratio and accelerated CO_2 dissolution are the two important characteristics that motivate the adoption of WAG operation to SAGCS. In multiphase flow, the non-wetting phase to wetting phase mobility ratio is defined as:

$$M = \frac{m_n}{m_w} = \frac{\mu_w \cdot k_{rn}}{\mu_n \cdot k_{rw}} \quad \text{(Eq. 33)}$$

where μ_w is the wetting phase viscosity, k_{rw} is the wetting phase relative permeability, μ_{nw} is the non-wetting phase viscosity, and k_{rn} is the non-wetting phase relative permeability. In the context of SAGCS, the pre-existing brine is considered as wetting phase and injected supercritical CO_2 is considered as non-wetting phase. If the intermittent CO_2-water injection is treated as quasi-mixture entering the aquifer, it will effectively bring down the mobility ratio compared to that of pure CO_2 injection. The effective mobility ratio is crucial for SAGCS efficiency due to the following reasons.

1) Mobility ratio determines if the displacement of the reservoir fluid is stable. If $M < 1$, stable displacement occurs, i.e. the displacement of brine acts in a piston-like fashion; if $M > 1$, unstable displacement occurs resulting in inefficient displacement of brine due to the formation of water/gas fingers. Figure 5.5 shows the stability of brine displacement under different mobility ratio.

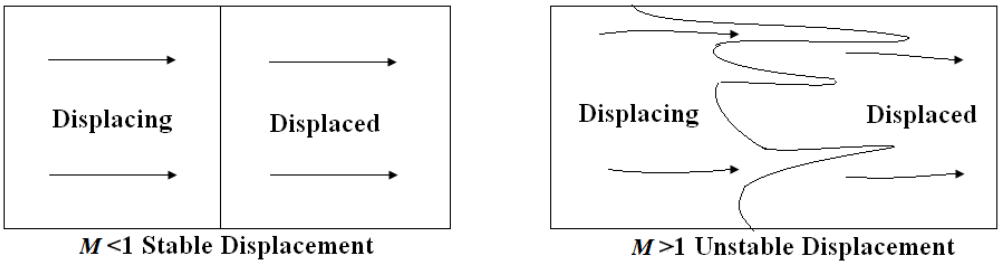

Figure 5.5 Stability of reservoir fluid displacement

2) Mobility ratio determines the speed of buoyancy-driven CO_2 migration. An investigation of the vertical migration of CO_2 plumes in porous media has shown that the front-end speed of a 1-D plume changes as the mobility ratio varies: CO_2 plume front travels faster with higher mobility ratio and vice versa as shown in Figure 5.6 [52]. Since the buoyancy-driven upward motion is the main cause of the excessive lateral

migration of in situ CO_2, it implies that in situ CO_2 will rise and spread slowly by reducing the mobility ratio, resulting into smaller environmental footprint.

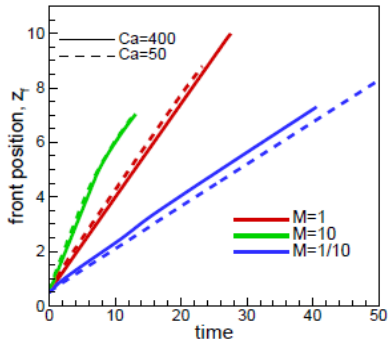

Figure 5.6 Front-end speed of a 1D CO_2 plume for different mobility ratio [52]

Another key aspect of WAG operation is the enhanced CO_2 dissolution. In literature, reservoir engineering techniques of injecting brine into the aquifer after the completion of CO_2 injection for achieving accelerated CO_2 dissolution have been studied by Leonenko and Keith [55]. Orr has [53] and Bryant et al. [54] also claimed that CO_2-chasing water injection can expedite the process of residual trapping. Promising results have been obtained from both numerical simulations and feasibility analysis. The fundamental mechanism of accelerating CO_2 dissolution by water injection is the enhanced convective mixing of CO_2 and brine/water. Since WAG operation consists of repeated cycles of CO_2-chasing water injection, it is expected that the CO_2 dissolution will be enhanced with the deployment of WAG. Considering these facts, optimal design of WAG operation for SAGCS is investigated below.

5.2.3 WAG Setup and GA-TOUGH2 Model

The WAG operation is studied for GCS in various saline aquifers (generic and identified large scale) and for different injection well orientations (vertical and horizontal). First, WAG operation for a generic saline aquifer with generic hydrogeological properties is investigated by considering both the vertical and horizontal injection wells. Vertical injection well is the most common type of well with mature and economical well completion technology. Nevertheless, SAGCS with horizontal injection well injection is

worth investigating since there are potential benefits of horizontal well injection as has been noted by Jikich and Sams [56] and Hassanzadeh et al. [57]. Next, WAG optimization is considered for identified large saline aquifers. Frio formation and Utsira formation are considered in our study. For these formations, all simulation parameters are retained from the history-matching simulations described in Chapter 4 for different injection schemes considered.

One complete cycle of CO_2-water injection is identified as a WAG cycle. A complete WAG operation is constituted of a series of such basic WAG cycles. For simplicity, it is assumed that WAG cycles are identical to each other. A schematic of the considered WAG operation is shown in Figure 5.7, with red blocks and blue blocks representing CO_2 injection and water injection respectively. The width of the blocks represents the duration of injection.

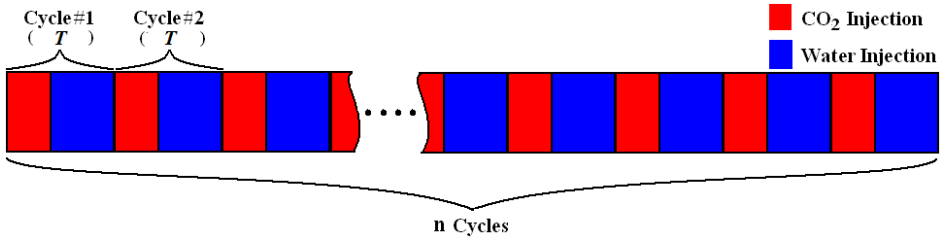

Figure 5.7 Schematic of the considered WAG operation

A set of four basic variables determines a unique cycle pattern, identified as: CO_2 injection rate I_{CO2}, water injection rate I_{water}, WAG ratio r_{WAG} (the ratio of injected CO_2 mass to injected water mass per cycle), and cycle duration T. Assuming the duration of CO_2 injection in one WAG cycle as t_{CO2}, the WAG ratio us defined by Eq. 34.

$$r_{WAG} = \frac{m_{CO2}}{m_{water}} = \frac{I_{CO2} t_{CO2}}{I_{water} t_{water}} = \frac{I_{CO2} t_{CO2}}{I_{water}\left(T - t_{CO2}\right)} \qquad \text{(Eq. 34)}$$

Rearranging Eq. 34, the duration of CO_2 injection can be expressed as Eq. 35.

$$t_{CO2} = \frac{r_{WAG} \cdot I_{water} T}{r_{WAG} \cdot I_{water} + I_{CO2}} \qquad \text{(Eq. 35)}$$

Eq. 35 suggests that a WAG operation can be uniquely defined if the four basic variables are given. Optimization of these four independent variables become a four-

dimension design problem, which can be computationally very expensive. To make the optimization more tractable, WAG cycle duration T defined be determined prior to the simulation. It is rather tricky to determine the value of T a priori. Nasir and Chong [58] have claimed that differences in WAG cycle duration time do not lead to significant differences in recovery efficiency for enhanced oil recovery. However, we have found in our research that WAG cycle duration time can significantly affect the performance of WAG operation under certain conditions. In our simulations/optimizations, we have set T at 30 days, which is an economically-feasible and performance-acceptable choice. The effect of WAG cycle duration time on sequestration efficiency will be discussed in a later section.

With above simplifications, the number of independent variables that uniquely determines a WAG operation reduces by two. Since WAG cycle duration time T is pre-determined, any two variables from I_{CO2}, I_{water}, or r_{WAG} can be picked as the basic optimization variables for designing a WAG operation. There is no constraint or preference as to which of these two parameters should be chosen as the optimization design variables. Picking I_{CO2} and I_{water} as the two design variables, the remaining variable r_{WAG} is determined by Eq. 36

$$r_{WAG} = \frac{m_{CO2}}{m_{water}} = \frac{M_{CO2}/n}{I_{water} t_{water}} = \frac{M_{CO2}}{nI_{water}\left(T - M_{CO2}/nI_{CO2}\right)} = \frac{M_{CO2}}{I_{water}\left(nT - M_{CO2}/I_{CO2}\right)} = \frac{M_{CO2} I_{CO2}}{I_{water}\left(I_{CO2} nT - M_{CO2}\right)} \quad \text{(Eq.36)}$$

where M_{CO2} is the total amount of CO_2 to be sequestered and n is the total number of WAG cycles.

A given amount of CO_2 to be sequestrated is usually known as the sequestration target of a given SAGCS project. A medium-size coal-fired power plant typically generates approximately 1 million tons of CO_2 annually. For the purpose of our investigation, it is reasonable to assume a 50% CCS efficiency, i.e. capture and sequestration of half million tons of CO_2 for a proposed WAG operation in a hypothetical generic aquifer. For WAG operation on identified large aquifers, the target sequestration amount is set identical to that for the actual project.

Eq. 35 and Eq. 36 determine unique WAG patterns. Simulations of non-optimized WAG operations are performed first to demonstrate the reduced CO_2 migration. Recalling that gaseous CO_2 reaches the caprock relatively fast under buoyancy and then migrates underneath the caprock, it is the radial migration of gaseous CO_2 that causes enormous land use as well as the leakage risk. Therefore, the saturation of gaseous phase CO_2 (SG) directly underneath the caprock, originating from the injection well along the migration direction, should serve as an ideal indicator of storage efficiency. SG is the percentage of void space in the formation occupied by gaseous CO_2; thus it varies from 0 to 1. It becomes greater than zero when CO_2 displacement of brine occurs, and remains zero in CO_2 free zones. Therefore, the maximum migration of in situ CO_2 can be effectively determined by examining SG profile underneath the caprock. Additionally, cross-sectional SG contours can also indicate the migration and dissolution of in situ CO_2.

5.2.3.1 WAG Operation with Vertical Injection Well over a Hypothetical Generic Saline Formation

A hypothetical generic cylindrical domain with thickness of 100 m is considered as the target aquifer as shown in Figure 5.8. The radius of the aquifer is set at 3000 m to minimize the influence of the boundary conditions. For generalization purpose, typical hydrogeological properties of the deep saline aquifers are applied to the domain. CO_2 and water are injected at the center of the domain by an injection well fully perforating the aquifer. No water pumping is included in the simulation domain, with the assumption that water production is either far away from the storage site or it comes from a nearby water reservoir. The WAG operation is assumed to consist of 20 WAG cycles each lasting for 30 days. The injection operation therefore lasts for 600 days. CO_2 migration is examined 50 years after the inception of injection. Figure 5.8 shows the computational model and the mesh. Due to symmetry, only a radial slice of the aquifer is modeled. The computational mesh is highly refined near the injection well and near the caprock to accurately capture the migration of in situ CO_2 in those regions.

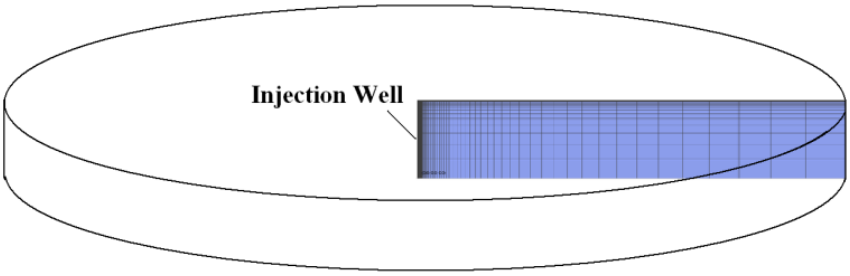

Figure 5.8 Generic domain for optimization of WAG operation

Table 5.2 summarizes the details of the model geometry, the hydrogeological properties and the simulation parameters.

Table 5.2 Hydrogeological properties, initial conditions and boundary conditions for the cylindrical domain considered for optimization study of WAG operation

Permeability (isotropic)	1.0×10^{-13} m^2
Porosity	0.12
Residual brine saturation	0.2
Residual CO_2 saturation	0.05
Relative permeability	van Genuchten-Mualem
Capillary pressure	van Genuchten-Mualem
Thermal condition	Isothermal
Boundary conditions	***For vertical injection well case***: fixed-state on circumference lateral boundary; ***For horizontal injection well case***: fixed-state on the outer two lateral boundaries, no mass flow on the inner two lateral boundaries; ***Both cases***: no mass flux on ceiling and floor
Initial conditions	P = 12 MPa, T = 45 ^{o}C for gravity-capillary equilibrium simulation
Initial CO_2 mass fraction	$X_{CO2} = 0$
Initial salt mass fraction	$X_{sm} = 0.15$

Half a million tons of CO_2 is to be sequestered annually, which consequently leads to a total of 0.822 million tons of CO_2 injection for the 600-day WAG operation. For the purpose of demonstrations, three simulation cases with arbitrary chosen WAG ratio r_{WAG} = 0.8, 1.5, and infinity (equivalent to CGI case) are performed. Figure 5.9 shows

CO_2 migration under the caprock after 50 years of injection for these three injection scenarios.

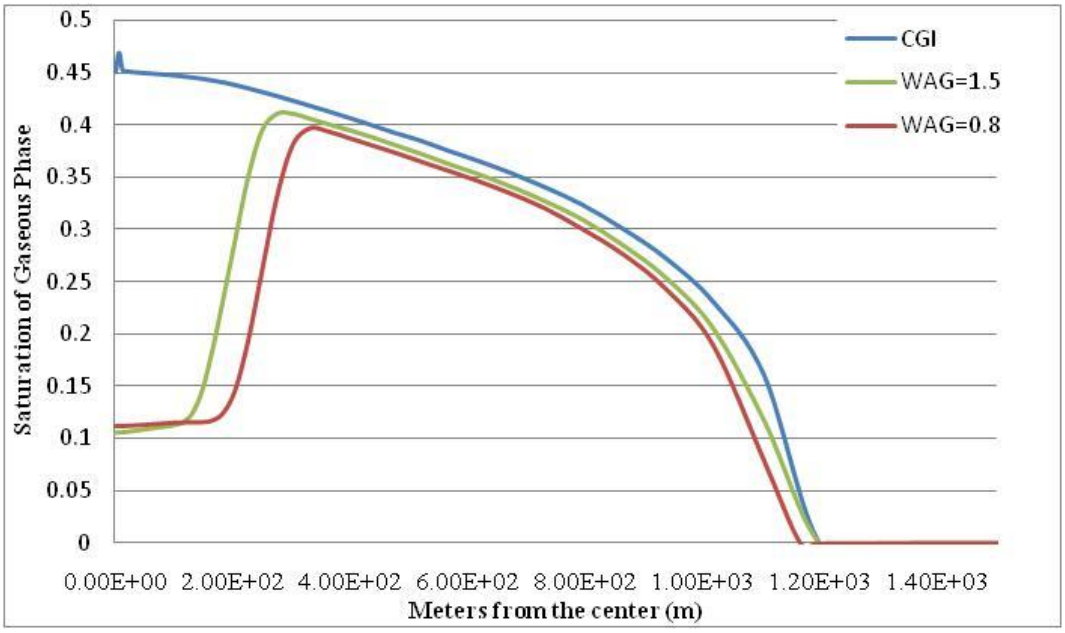

Figure 5.9 CO_2 saturation underneath the caprock at 50th year for CGI and two WAG operations

Figure 5.9 gives the SG profiles at the top of the aquifer, i.e. h = 100 m. The intersection of the SG curve with the x-axis (where SG = 0) indicates the location of the front-end of CO_2 plume, indicating the maximum distance of CO_2 migration. The area within this location can be identified as the CO_2 impact area where the leakage/contamination may occur. Further examination of Figure 5.9 leads to the following conclusions.

1) Less radial CO_2 migration is observed under WAG operation in comparison to the CGI operation.
2) WAG ratio (r_{WAG}) plays an important role in the performance of WAG operation. The case of r_{WAG}=0.8 results into roughly 3.5% reduction of plume migration, while reduction is the barely noticeable in case of r_{WAG}=1.5. It can also be noted that smaller WAG ratio *(*i.e. more water*)* is likely to make greater reduction in CO_2 migration.

3) Water injection also brings down the mean saturation of gaseous CO_2 under the caprock, as a combined effect of the retarded upward CO_2 migration and the enhanced CO_2 dissolution.

4) The simulations successfully demonstrate the potential benefits of WAG operation for improving the storage efficiency and safety of SAGCS.

With the successful demonstration of technical benefits provided by WAG operation, GA-TOUGH2 code is employed to obtain the optimal pattern for WAG operation. The fitness function of the optimization, i.e. the criteria of evaluating the performance of a certain WAG operation, is defined as the ratio of CO_2 migration reduction (with respect to that of CGI operation) to the total amount of water injection. It is mathematically represented by Eq. 37. This choice of fitness function arise from the consideration of the economical feasibility of implementing the WAG operation, since the transportation and pumping of water is likely to consume additional energy. It is obvious that a trade-off exists between the water consumption and the CO_2 migration reduction. Therefore, it is clear that the WAG operation leading to the maximum value of the fitness function would provide the optimal balance between the plume migration reduction and the water requirement.

$$fitness = \frac{R_{CGI} - R_{WAG}}{m_{water}} \qquad \text{(Eq. 37)}$$

As mentioned earlier, I_{CO2} and I_{water} have been chosen as the two optimization design variables. The search space is [30 kg/s,100 kg/s] for both I_{CO2} and I_{water}, resulting in the search space for r_{WAG} as [0.19 , 1.18]. Parameters for the GA optimizer are summarized in Table 5.2. A post-processing computational module has also been developed for determination of the migration reduction.

Table 5.3 GA optimizer setup for WAG design vertical injection well

Number of Individuals per Generation	8
Maximum Number of Generations	500
Natural Selection Algorithm	Bubble Sort, 50% Elimination
Mutation Rate	8 %
Cross-over Algorithm	Semi-Random Combination of Parents

The convergence history of fitness function is recorded and is shown in Figure 5.10.

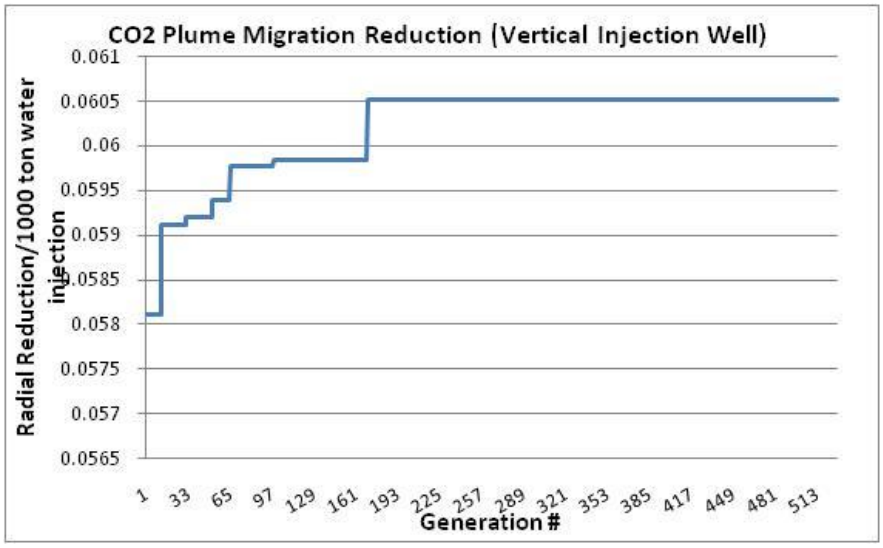

Figure 5.10 Optimization history of fitness function for WAG with vertical injection

The values of design variables corresponding to optimal WAG operation and the optimal fitness function value are summarized in Table 5.4.

Table 5.4 Optimal WAG operation and its fitness value for WAG with vertical injection

	I_{CO2} (kg/s)	I_{water} (kg/s)	r_{WAG}	Fitness (m/10^3 tons of water)
Optimal Value	55.26	39.19	0.567	0.0605

Recalling Eq.31 and definitions of the design variables, the durations of CO_2 and water injection in one WAG cycle can be calculated as

$$t_{CO2} = \frac{WAG \cdot I_{water} T}{WAG \cdot I_{water} + I_{CO2}} = \frac{0.567 \times 39.19 \times 2592000}{0.567 \times 39.19 + 55.26} = 743361 \text{ s} = 206 \text{ hr} = 8.6 \text{ days}$$

$$t_{water} = T - t_{CO2} = 30 - 8.6 = 21.4 \ days$$

Thus in each WAG cycle, CO_2 injection lasts for 8.6 days with an injection rate of 55.26 kg/s before it is cut off; then water injection begins with an injection rate of 39.19 kg/s until the 30-day cycle duration is completed. Identical WAG cycles repeat twenty times to complete the 600-day injection operation. Figure 5.11 shows the schematic of the optimal WAG operation.

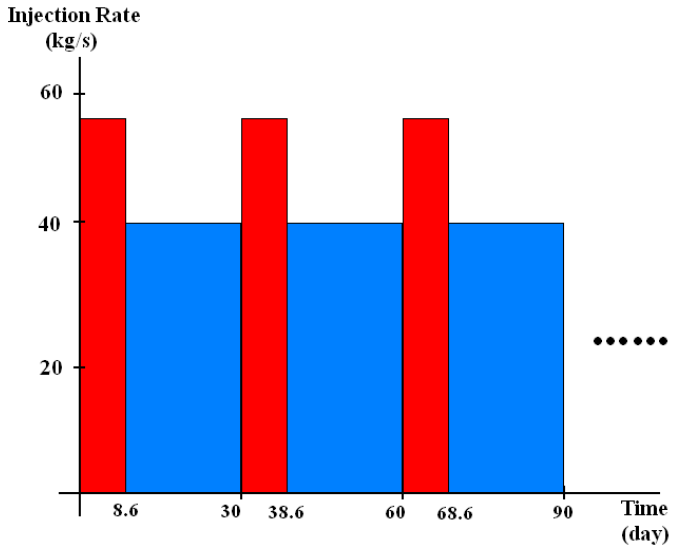

Figure 5.11 Schematic of the optimized WAG operation with vertical injection

In addition, CO_2 migration reduction obtained under the optimal WAG operation can be calculated as

$$\Delta R = M_{water}\, fitness = \frac{55.26\times(2592000-743361)\times 20\times 0.0605}{1000000}$$

$$= 87.66 \text{ m}/(10^3 \text{ tons water})$$

Table 5.5 summarizes the technical benefits of applying the optimal WAG operation.

Table 5.5 Summary of the benefits for implementing optimized WAG operation using a vertical well

		Vertical Injection Well
CGI	**CO_2 Radial Migration**	1210 m
WAG	**CO_2 Radial Reduction**	87.66 m
	CO_2 Radial Reduction Ratio	7.24 %
	CO_2 Impact Area Reduction	642308 m²
	CO_2 Impact Area Reduction Ratio	14%
	Total Water Injection Required	1448600 tons

The corresponding CO_2 plume migration under the caprock is compared to the CGI operation in Figure 5.12.

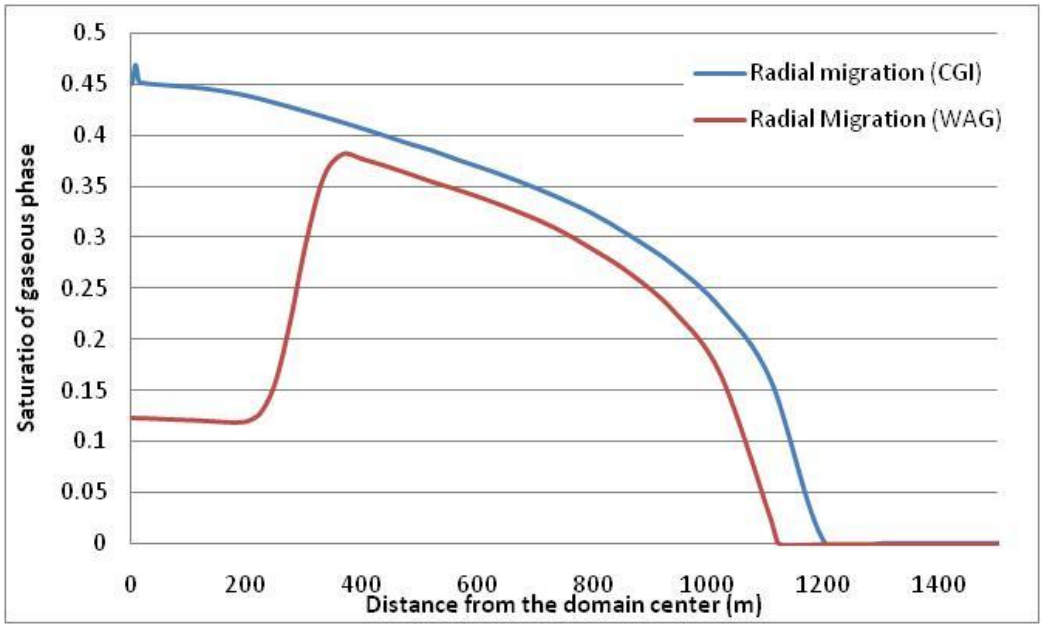

Figure 5.12 Radial gas saturation comparisons of optimized WAG operation and the non-optimized CGI operation for vertical injection well

As summarized in Table 5.5 and shown in Figure 5.12, a 14% reduction in CO_2 impact area and significant lowered CO_2 accumulation underneath the caprock can be achieved by replacing the conventional CGI operation with the optimal WAG injection. The cost of such a benefit is the pumping work required to inject 1448600 tons of water plus the extra CO_2 pumping work needed due to the increased injection pressure.

5.2.3.2 WAG Operation with Horizontal Injection Well over a Hypothetical Generic Saline Formation

As mentioned in an earlier section, Jikich and Sams [56] and Hassanzadeh et al. [57] have suggested the potential benefits of utilizing horizontal injection wells for SAGCS. It has been claimed that vertical wells provide insufficient injectivity, while horizontal injectors can greatly improve injectivity and storage capacity. Some key results on improved horizontal-well injectivity from Jikich and Sams' study are shown in Figure 5.13 [56]. Hassanzadeh et al. have also suggested that horizontal injection well can lead to significantly higher CO_2 dissolution rate compared to the vertical injection well when water chasing injection is applied [57].

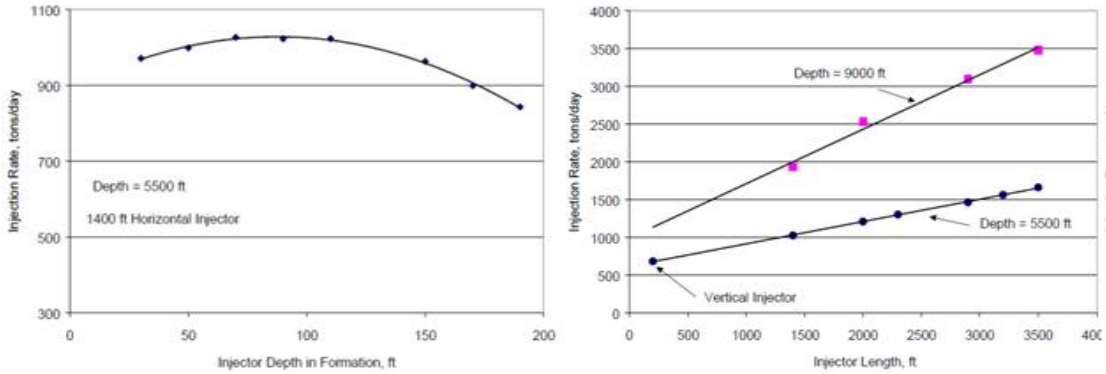

Figure 5.13 Improved well injectivity by utilization of horizontal injectors [56]

These suggested benefits of horizontal injection well have motivated our research to apply and optimize WAG operation for horizontal well injection. Unlike the perfectly symmetric flow patterns with vertical injection well, a full 3-D model is required when horizontal injection well is considered since the flow patterns are no longer symmetric. As a result, the modeling and simulation of the SAGCS with horizontal injection well becomes computationally more intensive and requires higher computational cost. A hypothetical generic aquifer of dimensions 8000 m × 8000 m × 100 m is considered. It is assumed that an 800-m horizontal injection well sits in the middle of the aquifer. Due to symmetry, only a quarter of the domain is modeled, as shown in Figure 5.14. The modeled computational domain is therefore of the dimensions 4000 m × 4000 m × 100 m with a 400-m horizontal injector sitting in the middle of this domain. All the hydrogeological properties and simulation parameters are the same as used in case of vertical well injection (Table 5.2). The boundary conditions and the target injection amounts are adjusted for the quarter domain under consideration.

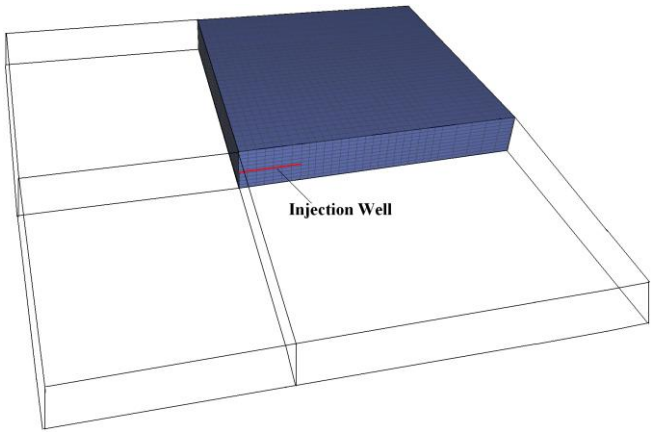

Figure 5.14 Quarter computational domain for WAG operation with horizontal injection

The introduction of horizontal injection well causes uneven CO_2 migration along the two principal axial directions. Since the top-planview of the CO_2 plume is expected to be elliptic than circular, it requires modification of the fitness function from the previous one used in vertical well injection case. For simplicity, the average value of the migration distance along the two principal directions is employed to estimate the fitness function. Therefore, Eq. 33 is modified as

$$fitness = \frac{R_{CGI} - R_{WAG}}{m_{water}} = \frac{\left(R_{CGI,x-direction} + R_{CGI,y-direction}\right)/2 - \left(R_{WAG,x-direction} + R_{WAG,y-direction}\right)/2}{m_{water}} \quad \text{(Eq. 38)}$$

where $R_{x\text{-}direction}$ and $R_{y\text{-}direction}$ represent the CO_2 migration distance along the direction of injection well and perpendicular direction to it respectively.

Again, I_{CO2} and I_{water} are chosen as the design variables. The search space of I_{CO2} and I_{water} is [20 kg/s , 80 kg/s] and the corresponding search space of r_{WAG} is [0.25 , 1.95]. Other performance parameters of GA optimizer are summarized in Table 5.6.

Table 5.6 GA optimizer setup for WAG design with horizontal injection well

	Horizontal Injection Well
Number of Individuals per Generation	6
Maximum Number of Generations	100
Natural Selection Algorithm	Bubble Sort, 50% Elimination

Mutation Rate	8 %
Cross-over Algorithm	Semi-Random Combination of Parents

The convergence history of the fitness function is shown in Figure 5.15.

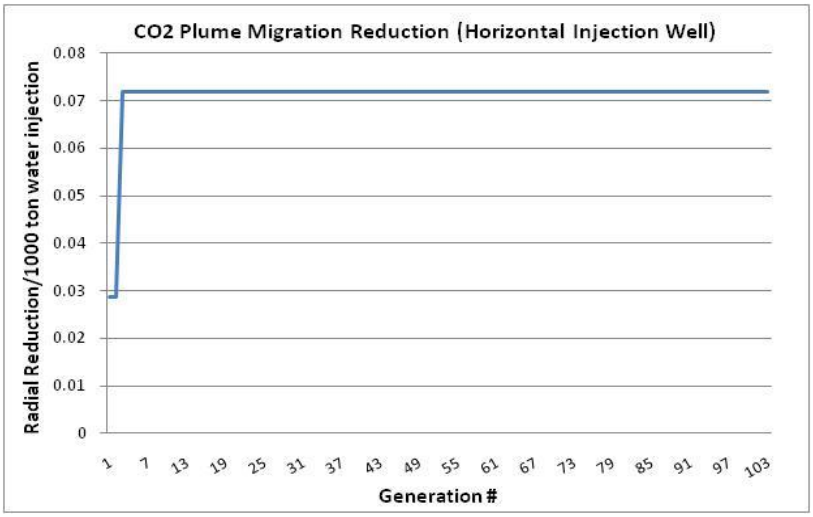

Figure 5.15 Optimization history of fitness function for WAG with horizontal injection

The values of design variables corresponding to optimal WAG operation and the optimal fitness function value are summarized in Table 5.7.

Table 5.7 Optimal WAG operation and its fitness value for horizontal injection well

	I_{CO2} (kg/s)	I_{water} (kg/s)	r_{WAG}	Fitness (m/10^3 tons of water)
Optimal Value	44.87	29.59	0.8229	0.0718

Recalling Eq. 31 and definition of design variables, the durations of CO_2 and water injection in one WAG cycle can be calculated as

$$t_{CO2} = \frac{WAG \cdot I_{water} T}{WAG \cdot I_{water} + I_{CO2}} = \frac{0.829 \times 29.95 \times 2592000}{0.829 \times 29.95 + 44.87} = 923342 \text{ s} = 256 \text{ hr} = 11 \text{ days}$$

$$t_{water} = T - t_{CO2} = 30 - 11 = 19 \text{ days}$$

Thus for each WAG cycle, CO_2 injection lasts for 11 days with an injection rate of 44.87 kg/s before it is cut off; water injection begins with an injection rate of 29.59 kg/s until the 30-day cycle duration is completed. Identical WAG cycles are repeated twenty times

to complete the entire 600-day operation. Figure 5.16 shows the optimal WAG operation.

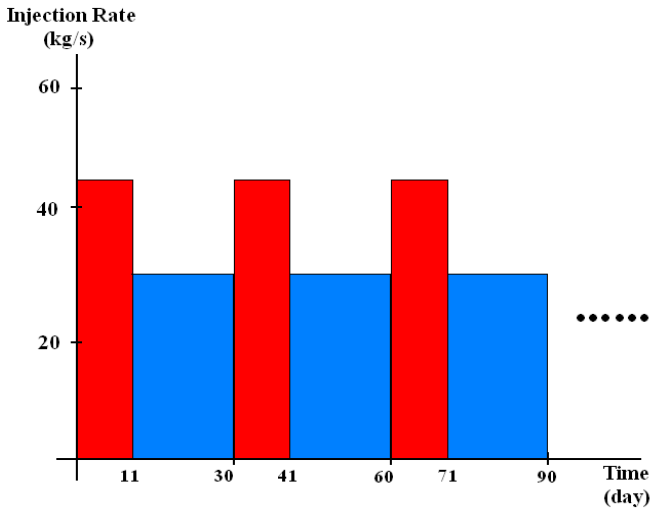

Figure 5.16 Schematic of the optimal WAG operation with horizontal injection

In addition, the CO_2 migration reduction associated with this optimal WAG injection operation can be calculated as

$$\Delta R = M_{water}\, fitness = \frac{44.87 \times (2592000 - 923342) \times 20 \times 0.0718}{1000000}$$

$$= 71.5 \text{ m} / (10^3 \text{ tons water})$$

Table 5.8 summarizes the technical benefits of applying the optimal WAG operation with horizontal injection well. The corresponding CO_2 plume migration underneath the caprock is compared to that for the CGI operation in Figure 5.17.

Table 5.8 Summary of the benefits for implementing optimized WAG operation with horizontal well

		Horizontal Injection Well
CGI	**CO_2 Radial Migration**	*x*-direction: 1082.7 m, *y*-direction: 865.7 m
WAG	**CO_2 Radial Reduction**	*x*-direction: 116.1 m, *y*-direction: 26.9 m
	CO_2 Radial Reduction Ratio	*x*-direction: 10.7 m, *y*-direction: 3.1 m
	CO_2 Impact Area Reduction	397560 m^2
	CO_2 Impact Area Reduction Ratio	14%
	Total Water Injection Required	995635 ton

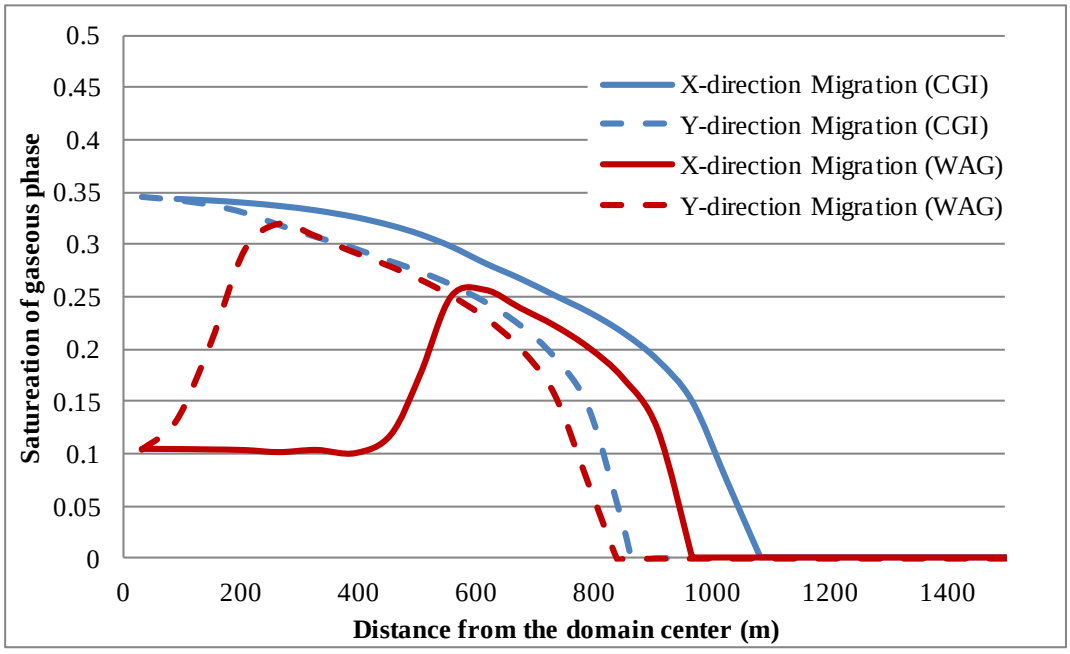

Figure 5.17 Radial gas saturation comparisons of optimized WAG operation and non-optimized CGI operation using a horizontal injection well

As summarized in Table 5.8 and shown in Figure 5.17, a 14% reduction in CO_2 impact area and significant lowered CO_2 accumulation underneath the caprock can be achieved by replacing the conventional CGI operation with the optimal WAG injection. The cost of such benefits is the pumping work required to inject 995635 tons of water plus the extra CO_2 pumping work needed due to the increased injection pressure. These results are qualitatively similar to those obtained for the WAG operation with vertical injection well. However, the water consumption of the WAG operation with horizontal injection well is substantially less, implying significantly less energy penalty and improved technical and economic feasibility.

5.2.3.3 WAG Operation with Vertical Injection Well over an Anisotropic Saline Formation

The actual aquifers are generally heterogeneous in all aspects. It is generally agreed that heterogeneity may cause channeling and fingering of CO_2 plume, thereby increasing the risk of leakage. It is also claimed that the heterogeneity could lead to locally enhanced trapping [53],[54]. Therefore, heterogeneity of aquifer properties should be taken into

account if more realistic simulations of higher accuracy are desired. In section 5.2.3.1 and section 5.2.3.2, optimizations of WAG operation were performed for a hypothetical generic saline aquifer with generic hydrogeological properties. The results have clearly suggested the potential benefits offered by the WAG technique. However, those simulations have not accounted for several types of uncertainties in the description of the reservoir conditions, among which heterogeneity is likely to be the most important one to affect the in situ migration of CO_2. In this section, we consider the optimization of WAG operation for an aquifer with anisotropy. Anisotropy of permeability, especially the horizontal-to-vertical permeability anisotropy, is the most important property that can have significant effect on CO_2 vertical migration. According to the laboratory studies on core samples, horizontal permeability of a saline formation normally is 10~1000 times greater than the vertical permeability. On the other hand, geological stratification such as seen in Mt. Simon formation, also significantly reduces the effective vertical permeability by orders of magnitude resulting in drastic anisotropy in the effective permeability.

In this study, we consider the WAG operation with permeability anisotropy for vertical well injection. The model geometry, domain discretization, reservoir conditions, and all other hydrogeological properties are the same as used in the simulation described in Section 5.2.3.1. A horizontal-to-vertical permeability ratio of 10, i.e. $k_{horizontal}/k_{vertical}=10$, is considered. A quick estimation of the effective permeability of the Utsira formation indicates that setting the permeability ratio of 10 is actually a conservative value as shown below.

Considering a stratified formation with all layers being horizontal, one can have the directional flow through that formation as shown in Figure 5.18. In Figure 5.18, each layer has its unique permeability as k_1, k_2, k_3, and thickness as h_1, h_2, h_3. The total thickness of the stratified formation is H. Flow transportation in horizontal and vertical directions is considered separately.

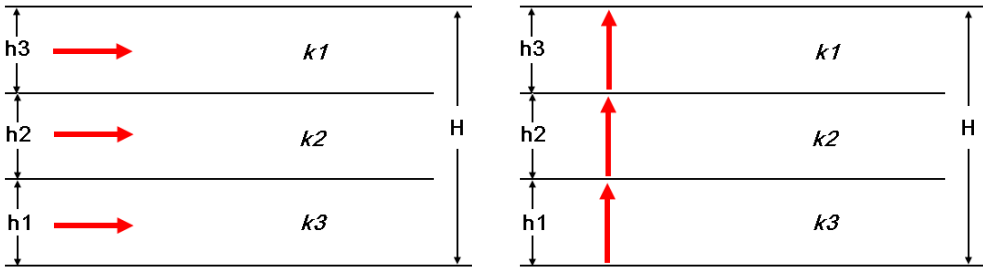

Figure 5.18 Schematic of stratified formation with (a) horizontal flow (b) vertical flow

Using mass conservation law and Darcy's law, Eq. 39 can be derived to evaluate the equivalent permeability along the two principal directions - horizontal and vertical as follows.

$$k_{eq,horizontal} = \frac{k_1 h_1 + k_2 h_2 + k_3 h_3}{H} = \frac{\sum kh}{H}$$
$$k_{eq,vertical} = \frac{H}{\frac{h_1}{k_1} + \frac{h_2}{k_2} + \frac{h_3}{k_3}} = \frac{H}{\sum \frac{k}{h}} \qquad \text{(Eq. 39)}$$

Recalling the Audigane et al.'s work [48], the Utsira formation can be described as a 9-layer structure with sandstone and shale alternatively overlapping each other, as shown previously in Figure 4.14. It is assumed that each layer is isotropic in hydrogeological properties as summarized in Table 5.7. Therefore, the equivalent permeability of the Utsira formation can evaluated as,

$$k_{eq,horizontal} = \frac{\sum_{i=1}^{9} k_i h_i}{\sum_{i=1}^{9} h_i} = \frac{3\times 70 + 4\times(0.01\times 5 + 3\times 25)}{70 + 4\times(5+25)} = 2.69 \text{ Darcy}$$

$$k_{eq,vertical} = \frac{\sum_{i=1}^{9} h_i}{\sum_{i=1}^{9} \frac{h_i}{k_i}} = \frac{70 + 4\times(5+25)}{\frac{70}{3} + 4\times\left(\frac{5}{0.01} + \frac{25}{3}\right)} = 92.4 \text{ mDarcy}$$

And the horizontal-to-vertical permeability ratio is obtained as

$$\frac{k_{eq,horizontal}}{k_{eq,vertical}} = \frac{2.69 \text{ Darcy}}{92.4 \text{ mDarcy}} \approx 29$$

The simple calculations above gives a horizontal-to-vertical permeability anisotropy of 29 for the Utsira formation, i.e. the Utsira formation is 29 times more permeable

horizontally than vertically. It demonstrates the existence of permeability anisotropy in actual aquifers, and also verifies that assigning a horizontal-vertical permeability ratio of 10 is indeed a conservative choice in our investigation for the design of WAG scheme for an anisotropic aquifer.

Two modifications have been made from the original case of WAG operation study with vertical injection well. First, horizontal permeability of the formation is increased to 1 Darcy from the original value of 100 mDarcy. Vertical permeability is retained as 100 mDarcy to keep the permeability anisotropy of 10. Another modification is the perforation of injection well. To take full advantage of the anisotropy, the injection perforation is reduced to one third of its original length and is placed at the lower aquifer following Bryant's suggestion of "injection low let rise" [54]. Other than these two modifications, all other parameters of the model are retained. Same assumptions for WAG operation, i.e. 20 WAG cycles each lasting 30 days, and identical amount of CO_2 for sequestration, i.e. 0.822 million tons over the 600-day injection, are applied. Slightly different from previous studies of WAG operation over isotropic formation, CO_2 migration beneath the caprock is examined immediately after the injection ceases.

The values of design variables corresponding to optimal WAG operation and the optimal fitness function value are summarized in Table 5.9.

Table 5.9 Optimized WAG operation injection in an anisotropic aquifer with vertical well

I_{CO2} **(kg/s)**	36.13
I_{water} **(kg/s)**	33.35
WAG	0.847
Fitness (m/10³ tons of water)	0.1438

Figure 5.19 shows schematic of the optimal WAG operation.

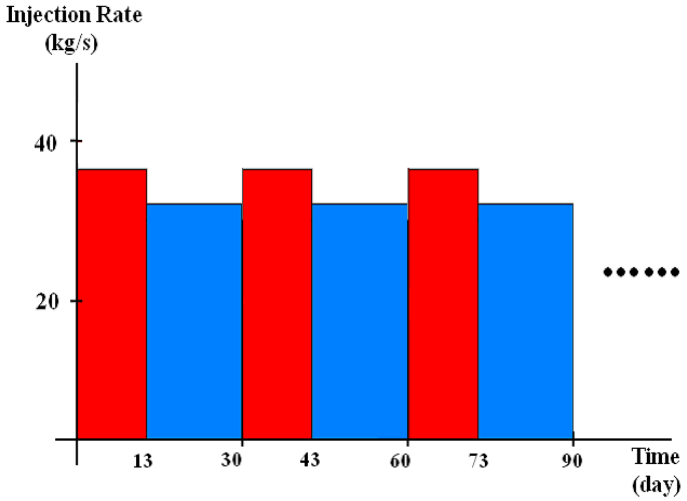

Figure 5.19 Schematic of the optimal WAG operation for anisotropic formation

Table 5.10 summarizes the technical benefits due to adoption of the optimal WAG operation for the anisotropic formation.

Table 5.10 Benefits of implementing the optimized WAG operation in an anisotropic aquifer

CO_2 Radial Reduction	140 m
CO_2 Radial Reduction Ratio	32.56 %
CO_2 Impact Area Reduction	316673 m^2
CO_2 Impact Area Reduction Ratio	54.52 %
Total Water Injection Required	973574 tons

Figure 5.20 illustrates the SG curve underneath the caprock of the formation for the optimized WAG operation and that for the CGI operation with CO_2 injection rate of 15.85 kg/s.

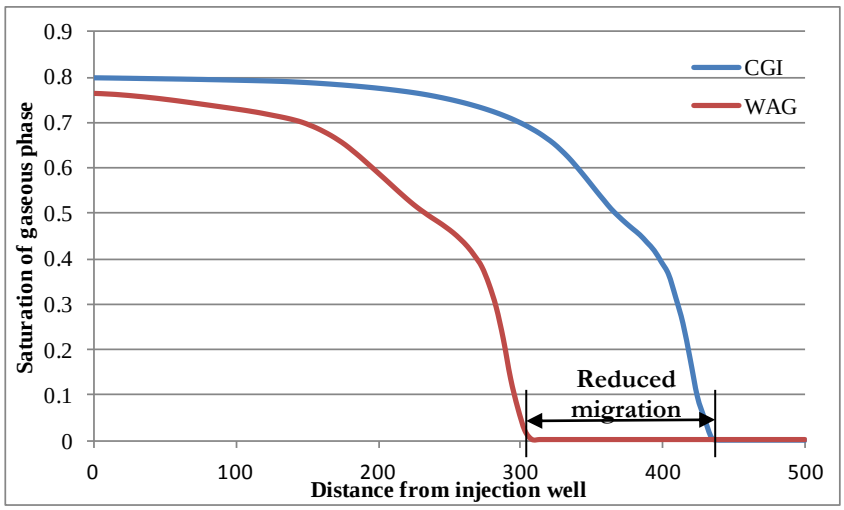

Figure 5.20 SG underneath the caprock showing migration reduction with optimized WAG operation in an anisotropic aquifer

As seen from Table 5.10 and Figure 5.20, consideration of permeability anisotropy has greatly improved the performance of WAG operation. Under a conservative horizontal-to-vertical permeability ratio of 10, CO_2 footprint after a 600-day injection is significantly reduced by 54.52 %. Recalling the 14 % reduction in CO_2 foot print for the isotropic formation, one can draw the conclusion that the anisotropy of formation permeability is an important parameter for high-performance WAG operation. It is also expected that even better performance of WAG operation would be achieved with higher horizontal-to-vertical permeability ratio. Moreover, CO_2 injection rate is significantly lower than that for the isotropic formation case. The duration of CO_2 injection in each WAG cycle is increased by about 4 days to maintain the overall injection amount. The lower injection rate and increased injection duration suggest improved injection conditions such as lower injection pressure.

To have a better illustration of the CO_2 migration reduction, simulations of three other non-optimized injection scenarios were conducted, namely the constant-gas-injection with low injection rate (low-CGI), constant-gas-injection with high injection rate (high-CGI), and cyclic CO_2 injection. For low-CGI case, CO_2 is injected with a constant mass flow rate of 15.85 kg/s for 600 days; for high-CGI case, CO_2 is injected with a constant mass flow rate of 31.71 kg/s for 300 days; cyclic CO_2 injection is very similar to the

optimal WAG injection except that water injection is removed from the operation. Therefore, all three additional cases have identical amount of injected CO_2 but zero water injection. Comparison of the SG curves of the optimized WAG operation and the three non-optimized injection scenarios are shown in Figure 5.21 and Figure 5.22, and summarized in Table 5.11.

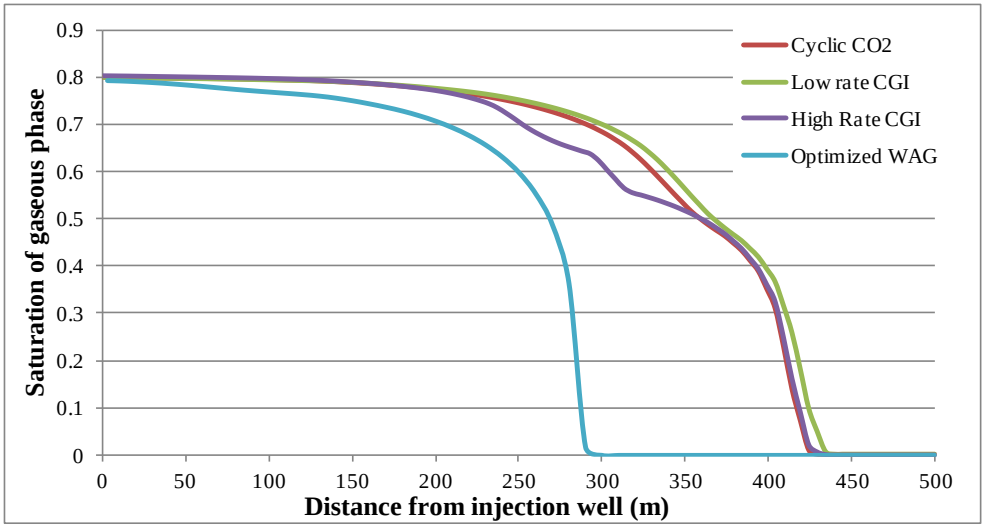

Figure 5.21 SG underneath the caprock; optimized WAG and non-optimized injection operations in an anisotropic aquifer

Figure 5.22 shows SG contours for the optimized WAG and three non-optimized injection scenarios after 600 days of injection at the radial cross-section of the formation.

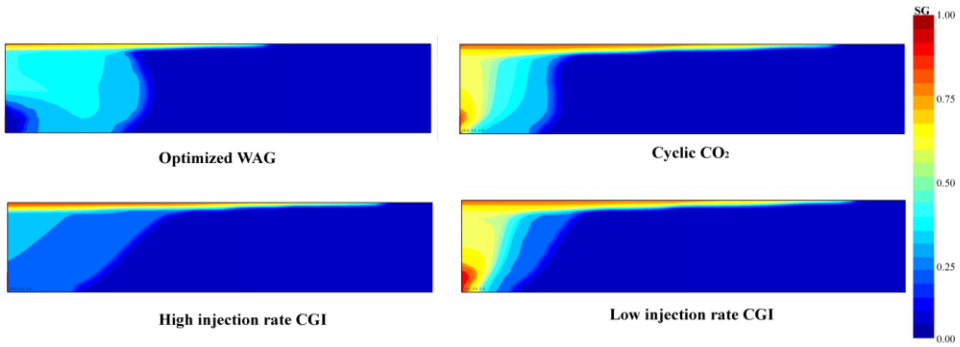

Figure 5.22 SG contours for optimized WAG and three non-optimized injection operations

Table 5.11 provides detailed comparisons between the optimized WAG operation and three non-optimized injection scenarios. The reduction of in situ CO_2 migration in optimized WAG is prominent.

Table 5.11 CO_2 migration comparisons of optimized WAG with three other non-optimized injection scenarios

Relative to Optimized WAG	Optimized WAG	Cyclic CO_2 Injection	High Rate CGI	Low Rate CGI
CO_2 Plume Migration	290 m	420 m	420 m	430 m
Additional CO_2 Migration	-	130 m	130 m	140 m
Increased Plume Radius	-	44.83 %	44.83 %	48.28 %
Increased Footprint Area	-	109.75 %	109.75 %	119.86 %

Results presented above clearly show the benefits of the WAG injection in reducing the in situ CO_2 migration. However, tradeoffs of such benefits need to be carefully considered for the safety and feasibility of SAGCS utilizing WAG operation. One of the most critical operational parameter of SAGCS is the pressure. The bottom line is that injection-induced pressure must not exceed the formation's fracture pressure under any circumstance. In practice, injection pressure is closely monitored and it is common to temporarily reduce the injection rate in order to reduce the elevated injection pressure. Figure 5.23 shows the injection pressure (average value along the injection well) under the optimized WAG operation. According to our investigation, the optimized WAG operation causes the injection pressure to oscillate as the CO_2 injection and water injection alternates. Considering the peak pressure, an 8% increase of reservoir pressure from its hydrostatic condition can be noticed near the injection well under the optimized WAG operation. On the other hand, a maximum of 2% increase in reservoir pressure is induced by the three non-optimized injection scenarios. Therefore, one can draw the conclusion that harsher injection condition is inevitable with WAG operations; however the induced pressure elevation by WAG operation could be moderate enough not to pose significant concerns. It should also be pointed out that reservoir pressure response to the injection of CO_2 and water is very sensitive to the hydrogeological properties of the formation, such as porosity and permeability. Pressure analysis should

be made on a case-by-case basis for different saline formations to ensure the feasibility and safety of WAG operation.

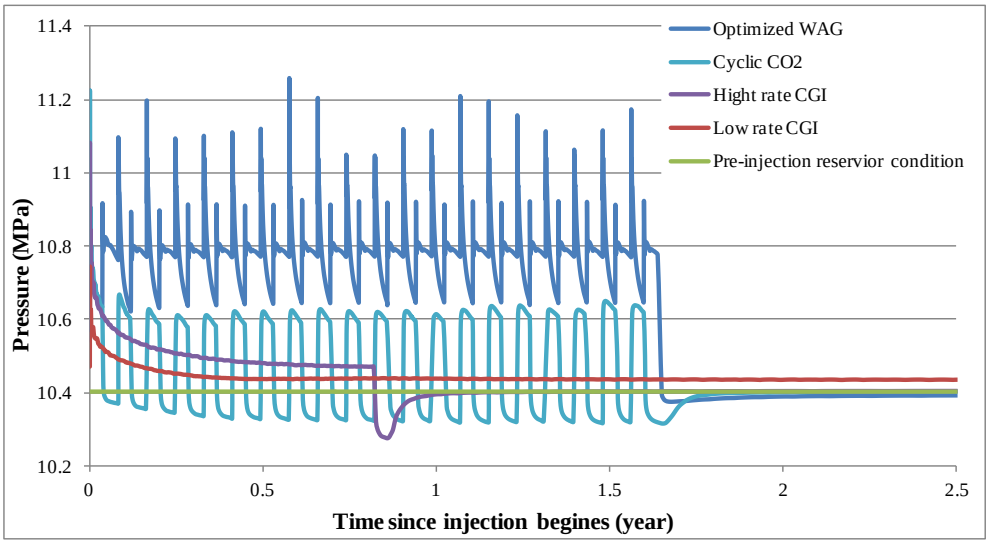

Figure 5.23 Reservoir pressure response of optimized WAG and three non-optimized injection schemes

One additional issue about the reservoir pressure response in the numerical simulations is the effect of boundary conditions. Due to the low compressibility of brine and rock matrix, the pressure disturbance travels throughout the aquifer orders of magnitude faster than the CO_2/brine mass flow. Recalling that the boundary conditions imposed in our numerical model are the fixed-state boundary conditions, which essentially represent an infinite aquifer, the injection pressure given by the simulations would be underestimated. However, we find that such an underestimation is negligibly insignificant if the actual aquifer is sufficiently large so that the pressure disturbance travels only downstream within the time period of interest.

With the success of CO_2 migration reduction using WAG operation for generic saline aquifers, we decided to test the performance of WAG operation on numerical models with hydrogeological properties of real large scale aquifers. For this purpose, we again consider the three representative models of identified saline formations previously described in Chapter 4 for numerical implementation and optimization of WAG operation. These three models are the one established for the Frio pilot project, the

generalized cylindrical Utsira formation model, and a newly established cylindrical Utsira Layer#9 model. The Frio model represents the saline formation of relatively small thickness but with significant geological up-dip. The generalized Utsira model represents the saline formation with relatively large thickness and stratified hydrogeology. The cylindrical Utsira Layer#9 model is a good representative of saline formation with relatively small thickness and anisotropic hydrogeology.

5.2.3.4 WAG Operation for Frio Formation

The numerical model of Frio formation presented in Chapter 4 is used for this investigation. It is helpful to recall the key characteristics of the modeled Frio formation. The modeled formation has a thickness of 23 m and a northern updip of 16°. CO_2 injection occurs in the upper half of the formation over an 8 m perforation under the caprock. Hysteresis of relative permeability and capillary pressure is considered using the work of Doughty et al. [45]. The characteristics of WAG operation described in the previous studies above are largely retained. To be specific, it is assumed that the WAG operation consists of 20 cycles each lasting for 30 days, and a total amount 96,000 tons of CO_2 is injected over the 600-day injection. The northward migration of CO_2 is examined at the 50th year since the beginning of CO_2 injection. The optimized WAG operation is summarized in Table 5.12 and illustrated in Figure 5.24.

Table 5.12 Optimized WAG operation for Frio formation SAGCS

I_{CO2} **(kg/s)**		81.45
I_{water} **(kg/s)**		32.02
r_{WAG}		0.615
Fitness value (m/10^3 tons of water)	***Non-hysteresis***	0.02244
	Hysteresis	0.01284

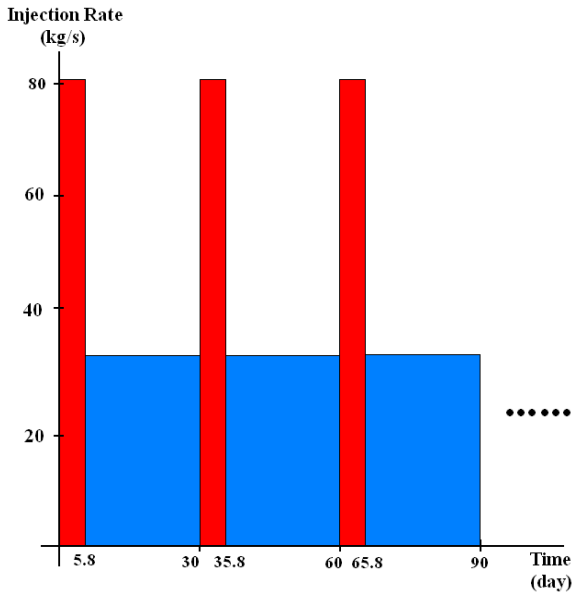

Figure 5.24 Schematic of optimized WAG operation for Frio formation SAGCS

Figure 5.25 shows the migration of CO_2 plume underneath the caprock for optimized WAG operation and for the constant-rate injection. A close-up view of the plume's front-end is shown in Figure 5.25 as the windowed insert.

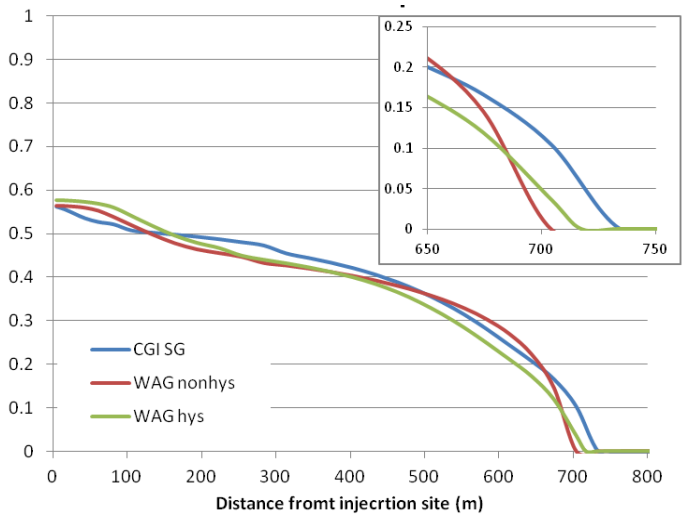

Figure 5.25 SG underneath the caprock showing plume reduction with optimized WAG operation for Frio formation

Table 5.21 summarizes the technical benefits of utilizing the optimized WAG operation for Frio formation.

Table 5.13 Benefits of adopting the optimized WAG operation for Frio formation

CGI	**CO_2 Radial Migration**	734 m
	Dissolution	23.28 %
WAG	**CO_2 Radial Reduction**	30 m (non-hys), 17 m (hys)
	CO_2 Radial Reduction Ratio	4.08 % (non-hys), 2.32 % (hys)
	CO_2 Impact Area Reduction	135528 m^2 (non-hys), 77494 m^2 (hys)
	CO_2 Impact Area Reduction Ratio	8 % (non-hys), 4.45 % (hys)
	Total Water Injection Required	156097 tons
	Dissolution	30.4 % (non-hys), 30.3 % (hys)

As seen from Figure 5.36 and Table 5.21, WAG operation brings noticeable but very limited reduction in CO_2 plume migration for Frio formation SAGCS. It only leads to 8% reduction in CO_2 footprint. Recalling the characteristics of the Frio formation from Chapter 4, it appears that two aspects of Frio formation may be responsible for the lackluster performance of WAG operation. First, the 16° northward updip of the formation is possibly responsible as it introduces dominant buoyancy-driven flow throughout the life-span of the SAGCS project. The significant effect of geological gradient on migration of in situ CO_2 can be revealed with the following analysis. Considering a saline formation with no geological updip, the migration of in situ CO_2 can be decomposed as the buoyancy-driven upward migration and the pressure-driven radial migration. Looking more closely, the radial pressure gradient can be caused by either CO_2 injection or non-uniform CO_2 concentration due to buoyancy. Buoyancy does not directly contribute to radial transportation of CO_2. In contrast, CO_2 migration under geological updip is directly and constantly enhanced by buoyancy due to the upward migration. Such enhanced migration is expected to compromise the performance of WAG operation. Secondly, the small thickness of Frio formation is another factor that could lead to failure of successful WAG operation. Furthermore, the assumption of intermittent CO_2-water slugs being treated as quasi-mixture is only valid when the interaction of the two components takes place before the slug reaches the caprock. In summary, the small thickness together with enhanced buoyancy-driven upward migration are very likely to make it impossible for injected CO_2 and water to interact before reaching the caprock. Therefore, it is suggested by this study that geological updip and aquifer thickness should be carefully considered before deploying WAG operation for those type of aquifers.

5.2.3.5 WAG Operation for Generalized Utsira Model

In contrast to Frio formation, the generalized Utsira model for SAGCS has insignificant geological updip and relatively large thickness. Recalling the simulation studies of the Sleipner SAGCS project in Chapter 4, the Utsira formation is a layered formation with about 200 m in thickness without evidence of any significant geological updip. Therefore, the cylindrical model of layered Utsira formation presented in Chapter 4 is used to study the WAG operations. All hydrogeological properties and numerical conditions used in Chapter 4 are retained, including the amount of CO_2 injection at a rate of 1 million tons per year. The conventional CGI operation used in Chapter 4 is replaced by the WAG operation. Reduction in radial CO_2 migration under the caprock is examined as the optimization criteria for five years of injection.

The generalized Utsira formation model consists of nine alternating shale and sandstone layers, and the injection takes place at the middle of the bottom sandstone layer. The assumption of 30-day WAG cycle duration is retained which was employed in all the previous simulations. The WAG operation lasts for 5 years, during which 1 million tons of CO_2 is injected annually. The radial migration of CO_2 in the topmost sandstone layer is examined after 2, 3, and 5 years of injection.

The values of design variables corresponding to optimal WAG operation and the optimal fitness function value are summarized in Table 5.14

Table 5.14 Optimized WAG operation for generalized Utsira formation

I_{CO2} **(kg/s)**	95.75
I_{water} **(kg/s)**	75.32
r_{WAG}	0.64
Fitness (m/10^3 tons of water)	0.0251

Figure 5.24 shows the schematic of the optimal WAG operation for the generalized Utsira formation model.

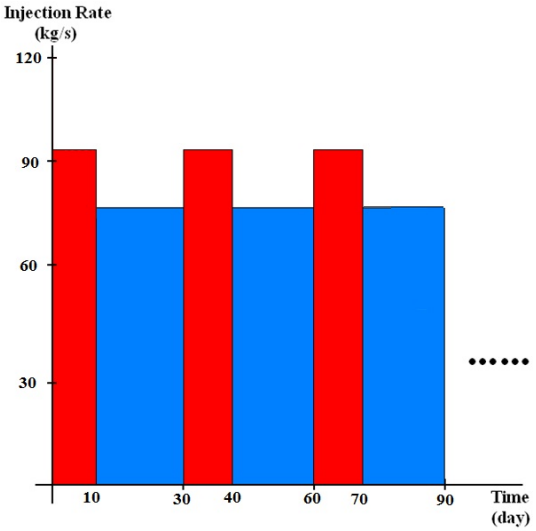

Figure 5.26 Schematic of optimized WAG operation for Utsira formation

Figure 5.27 shows the CO_2 migration underneath the caprock at 2nd, 3rd, and 5th year for optimized WAG and conventional CGI operations. The reduction in radial CO_2 migration is prominent for the WAG operation.

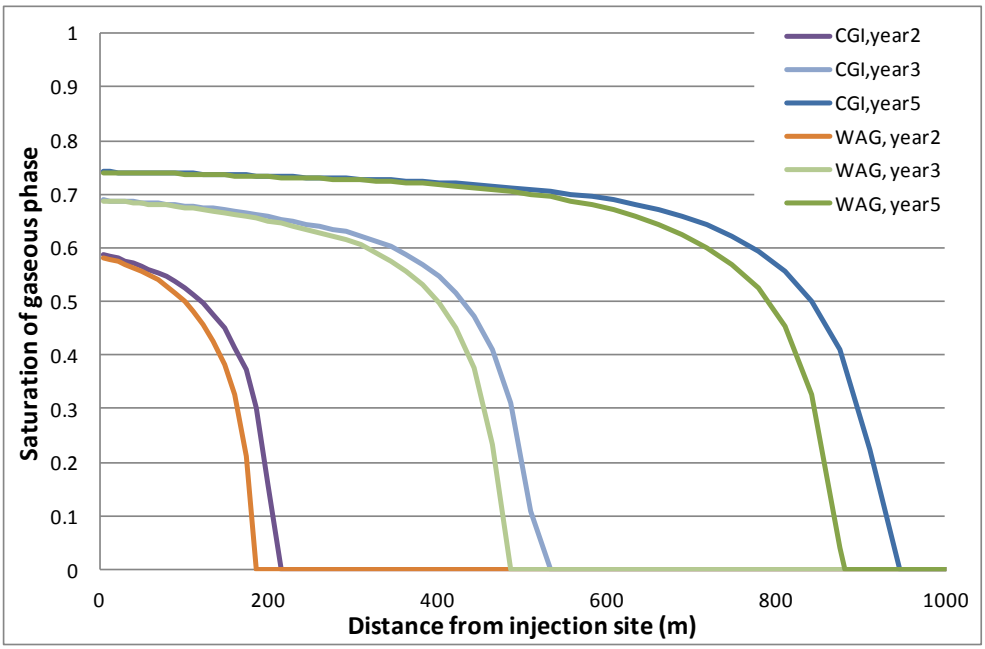

Figure 5.27 SG underneath the caprock showing plume reduction with optimized WAG operation for Utsira formation SAGCS

Table 5.15 summarizes the benefits of adopting the optimized WAG operation for the generalized Utsira formation model.

Table 5.15 Benefits of implementing the optimized WAG operation for Utsira formation SAGCS

CGI	**CO_2 Radial Migration**	946.7 m
	Dissolution	16.89 %
WAG	**CO_2 Radial Reduction**	65.2 m
	CO_2 Radial Reduction Ratio	6.89 %
	CO_2 Impact Area Reduction	372,095 m^2
	CO_2 Impact Area Reduction Ratio	13.23 %
	Total Water Injection Required	1.5625 million tons annually
	Dissolution	23.43 %

As seen from Figure 5.27 and Table 5.15, CO_2 migration under the caprock in the generalized Utsira formation has been significantly reduced by the WAG operation. Compared to the case of Frio formation, higher optimization fitness value for the Utsira formation model means more effective WAG operation. Time-elapsed CO_2 migration recorded in Figure 5.27 provides the clear evidence that noticeable reduction in CO_2 migration can be observed as early as 2 years after injection. More importantly, it can also be seen that migration reduction in later years tends to be greater than that in the earlier years, suggesting the development of greater reduction in CO_2 migration as injection proceeds. This is an encouraging result considering the decade-long life-span of SAGCS projects.

It is also useful to investigate how the layered structure of the formation affects the performance of the WAG operation. Closer look at the in situ CO_2 migration for conventional CGI operation (shown in Figure 5.28) and optimized WAG operation (shown in Figure 5.29) provides the information on effect of layered structure on conventional CGI and optimal WG operation.

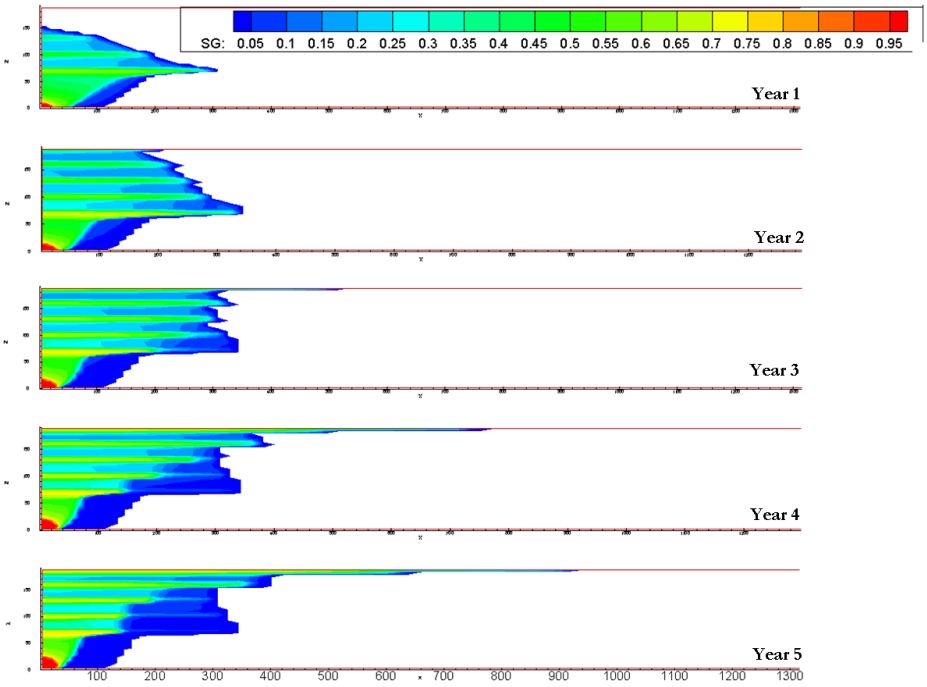

Figure 5.28 CO_2 plume migration during the first 5 years of CGI operation for the Utsira formation

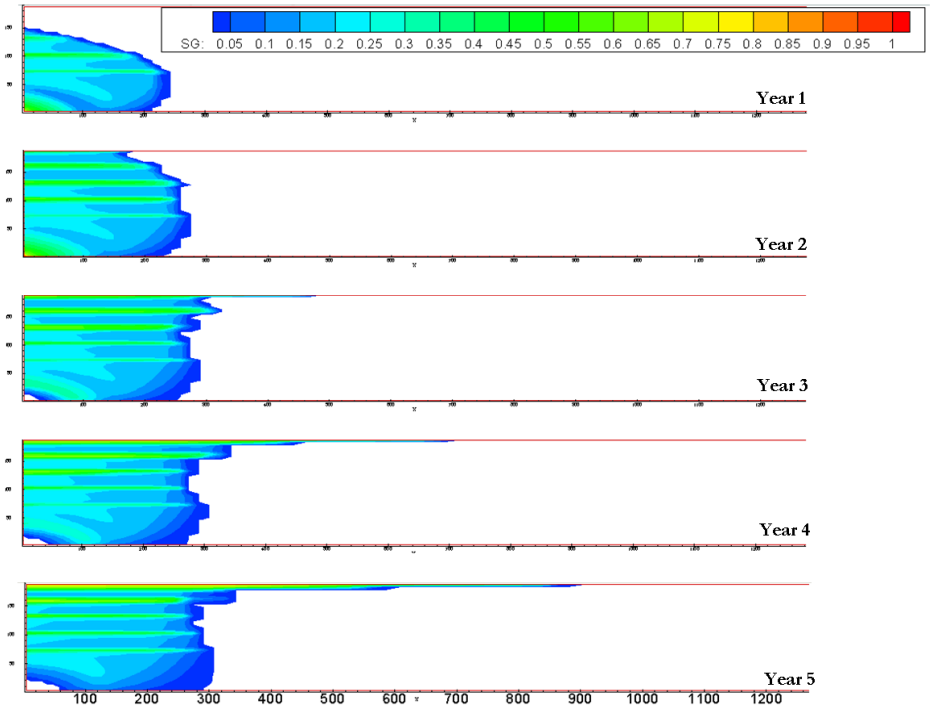

Figure 5.29 CO_2 plume migration during the first 5 years of optimized WAG operation for the Utsira formation

The generalized Utsira formation model has an equivalent horizontal-to-vertical permeability ratio of 29 according to the calculation presented in Section 5.2.3.3. Simulations presented in Section 5.2.3.3 have shown great improvement in WAG performance due to the anisotropic permeability. Similar conclusion can be also drawn from the simulations results presented in this section. Comparing Figure 5.28 and Figure 5.29 side by side, it can be seen that in situ CO_2 migration has been significantly reduced by the WAG operation, under which the displacement of brine in the lower sandstone layer becomes more stable. Storage efficiency increases under such scenario since more pore-space can now be occupied by supercritical CO_2. Additionally, storage safety is also improved due to the lowered concentration of supercritical CO_2.

However, the fitness function value for the layered Utsira formation is not as satisfactory as that for the generic anisotropic aquifer (0.0251 versus 0.1438), although the former case has a higher permeability ratio. Two possible explanations are proposed for these results. First, the upward migration (as well as the resulting radial migration) of in situ CO_2 has already been significantly retarded by the secondary-sealing effect introduced by the layered structure of the formation, as demonstrated in Chapter 3. Recalling previous analysis, it can be seen that the migration reduction mechanism is similar for both WAG operation and the secondary sealing effect. Secondly, the CO_2 injection rate is set at 1 million tons annually for the layered Utsira formation, while it was 0.5 million tons annually for the generic anisotropic aquifer. This doubling of CO_2 injection rate for the Utsira formation effectively speeds up the upward migration of in situ CO_2. However, it has been previously discussed that CO_2-water interaction has to take place before the slug reaches the caprock to ensure the superior performance of WAG operation. It is therefore the enhanced upward migration of CO_2 together with the secondary sealing effect that make the WAG operation less satisfactory when applied to the generalized layered Utsira formation model compared to the WAG operation for the generic anisotropic aquifer.

5.2.3.6 WAG Operation for Utsira Layer#9 Model

The topmost sandstone layer (Layer #9) of Utsira formation as presented in Chapter 4 can server as another excellent candidate for the investigation of WAG operation due to

its well-understood hydrogeological properties. A cylindrical domain with the average thickness of Utsira Layer#9 is modeled, which possesses identical characteristics of the detailed 3D Utsira Layer#9 model (from Chapter 4) except for the absence of 3D topography. Although topographical details could be important in determining the accurate migration of in situ CO_2, such a simplification, without compromising accuracy, is necessary for analyzing the effectiveness of WAG operation on CO2 migration without incurring excessive computational cost.

The geometric and hydrogeological characteristics of the simplified Utsira Layer#9 model can be summarized as follows. We consider a cylindrical domain with thickness of 35 m with horizontal flat caprock. All hydrogeological properties are retained from the detailed 3D Utsira Layer#9 model described in Chapter 4, the most important being the horizontal-to-vertical permeability ratio of 10. CGI operation with nine-year average CO_2 injection rate of 2.7 kg/s is considered as the baseline case for comparison.

The effect of WAG cycle durations on CO_2 migration is investigated for this relatively thin formation. The 30-day, 15-day, and 5-day WAG cycle duration are considered for the WAG optimization design. Our computations show that for the simplified Utsira Layer#9 model, only the WAG operation with 5-day cycle leads to noticeable migration reduction. Therefore, all results given below for 5-day WAG cycle.

The values of design variables corresponding to optimal WAG operation and the optimal fitness function value are summarized in Table 5.16.

Table 5.16 Optimized WAG operation for Utsira Layer#9 model

I_{CO2} **(kg/s)**	11.56
I_{water} **(kg/s)**	7.62
r_{WAG}	0.646
Fitness (m/10³ tons of water)	0.506

Figure 5.30 shows the schematic of optimized WAG operation for the simplified Utsira Layer#9 model with 5-day WAG cycle duration.

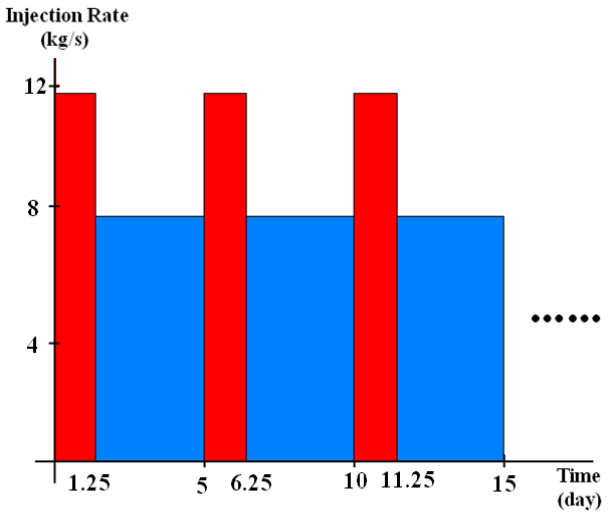

Figure 5.30 Schematic of optimized WAG operation for Utsira Layer#9 model

Figure 5.31 shows the CO_2 migration underneath the caprock after two years of conventional CGI and optimized WAG operation. The reduction in radial CO_2 migration is significant for WAG operation.

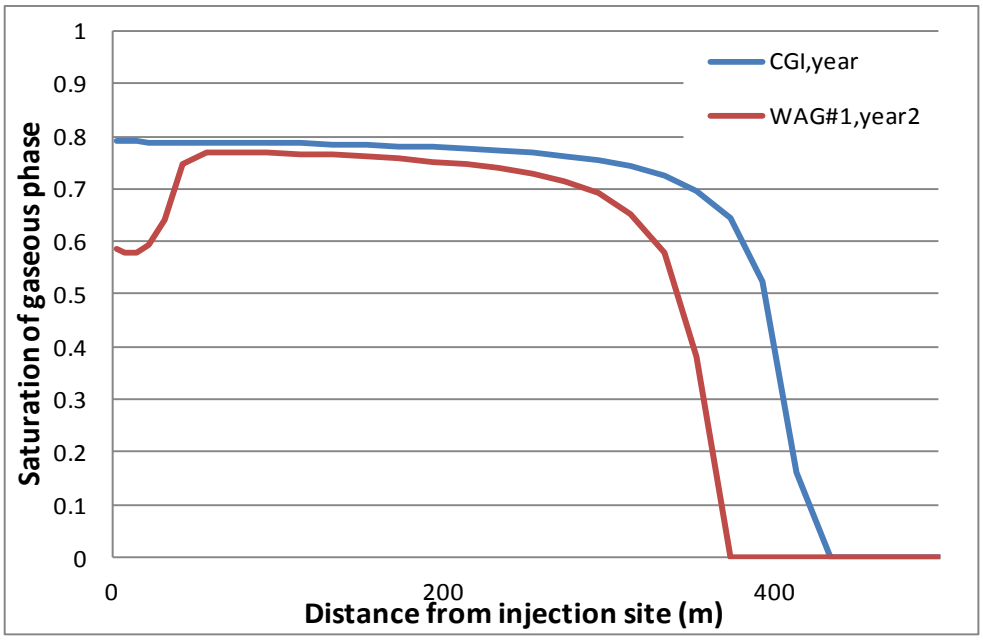

Figure 5.31 SG underneath the caprock showing plume reduction with optimized WAG injection for Utsira Layer#9 model

Table 5.21 summarizes the benefits of adopting the optimized WAG injection for simplified Utsira Layer#9 model.

Table 5.17 Benefits of optimized WAG operation for the Utsira Layer#9 model

CGI	**CO_2 Radial Migration**	423 m
	Dissolution	8.97 %
WAG	**CO_2 Radial Reduction**	49 m
	CO_2 Radial Reduction Ratio	11.58 %
	CO_2 Impact Area Reduction	122689 m2
	CO_2 Impact Area Reduction Ratio	21.83 %
	Total Water Injection Required	231916 tons
	Dissolution	23.02 %

As seen from Figure 5.31 and Table 5.17, significant reduction in CO_2 migration has been achieved after only two years of WAG operation. Additionally, CO_2 dissolution is also significantly enhanced from about 9 % to 22 % of the total injected CO_2. More importantly, the results reveal the strong relationship between WAG cycle duration and the reservoir thickness regarding the performance of WAG operation. Surprisingly our simulation results show that the 30-day cycle WAG operation actually "enhances" (not "reduces") the lateral migration of the CO_2 plume. Such a situation can be slightly mitigated when the 15-day WAG cycle duration is applied; however, no noticeable migration reduction is achieved. Considering all three cases of WAG operation for identified formations, it appears that the aquifer thickness and WAG cycle duration are critical factors affecting the performance of a WAG operation. When the aquifer is thin, it takes less time for the CO_2 to reach the caprock. The assumption of treating alternative water and CO_2 slugs as quasi-mixture is only valid when injected CO_2 interacts with the chasing water before it reaches the caprock. Failing to fulfill this requirement leads to poor WAG performance. It is the reservoir thickness and WAG cycle duration that determine the validity of quasi-mixture assumption for a given aquifer. Longer WAG cycle duration requires larger reservoir thickness and vice-versa. Our simulations show that minimum reservoir thickness may exist for a given WAG cycle duration under which the quasi-mixture assumption is valid and vice-versa. This minimum thickness requirement may ultimately determine the technical feasibility of WAG operation for an aquifer for achieving any reduction in CO_2 migration. Following

this rationale, the success of WAG operation with 5-day cycle duration and its failure with the 15-day and 30-day cycle durations can be explained for Utsira Layer#9 model. This also implies that the CO_2 injected at the bottom of Layer#9 reaches the caprock between 5 to 30 days (more likely in approximately 15 days since minor reduction in plume can be observed in this case) with the given reservoir hydrogeological properties and injection parameters.

With the simulation and optimization of WAG operation for three distinct identified saline aquifers, one can draw the conclusion that the WAG operation certainly holds technical promise in retarding the spread of gaseous CO_2 in actual large scale saline aquifers. It is also obvious from the results that the timeframe of in situ CO_2-water mixing versus the chosen WAG cycle duration are important considerations that must be carefully determined in assuring the improved reservoir performance due to implementation of WAG operation. Various geological factors of the formation, such as geological updip and reservoir thickness could contribute to insufficient mixing and thus compromise the performance of WAG operation. Therefore the operational parameters of WAG operation need to be designed on a case-by-case basis for achieving the optimal performance.

5.2.3.7 Sensitivity of WAG Operational Parameters

In the previous sections, it has been shown that the performance of WAG operation varies depending upon the geometric and hydrogeological parameters of the aquifer. It is therefore beneficial to look into the effect of various operational parameters on the performance of WAG operation. If the total amount of CO_2 for sequestration is given, any three out of the four operational parameters, namely the CO_2 injection rate (I_{CO2}), the water injection rate (I_{water}), the WAG ratio (r_{WAG}), and the WAG cycle duration (t_{WAG}) determine a unique WAG operation pattern. Using the case of generic anisotropic saline formation for SAGCS described in Section 5.2.3.3, the effect of WAG operational parameters on the performance of WAG operation is investigated. The optimized case presented in Section 5.2.3.3 is used as the baseline case. The CO_2 injection rate (I_{CO2}), water injection rate (I_{water}), and cycle duration (t_{WAG}) are chosen as the WAG operational

parameters. Four additional cases are considered, the results of which are summarized in Table 5.18.

Table 5.18 Various simulations used in the sensitivity study of WAG operation to its operational parameters

	I_{CO2} (kg/s)	I_{water} (kg/s)	Cycle Duration (day)	r_{WAG}
Baseline case	36.13	33.35	30	0.847
Variation #1	50	33.35	30	0.697
Variation #2	36.13	50	30	0.565
Variation #3	36.13	33.35	15	0.847
Variation #4	36.13	33.35	50	0.847

In the following figures, radial cross-sectional views showing the migration of in situ CO_2 under the above four WAG cases of Table 5.18 are presented. Since all these cases are small variations from the optimal WAG baseline case, they all show significant reduction in CO_2 migration compared to the CGI case. However, the performance of WAG operation (fitness function) which is defined as plume reduction per unit amount of water injection differs greatly from one case to another.

Figure 5.32 shows the in situ CO_2 distribution in the reservoir for the optimized WAG operation and its variation #1 (with higher CO_2 injection rate compared to the baseline case).

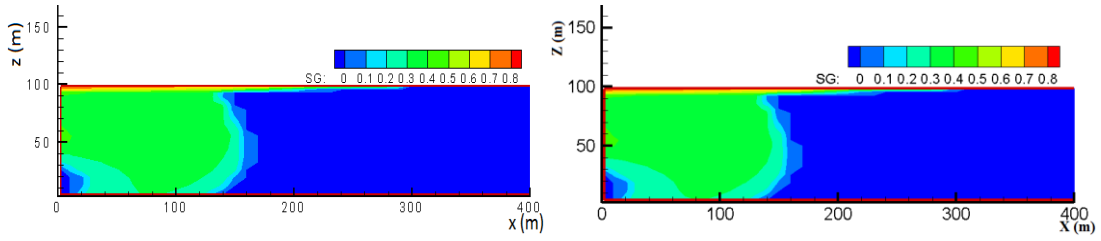

Figure 5.32 CO_2 distribution in the reservoir (left: optimized WAG; right: WAG with variation #1)

Figure 5.33 shows the in situ CO_2 distribution in the reservoir for the optimized WAG operation and its variation #2, (with higher water injection rate compared to baseline case).

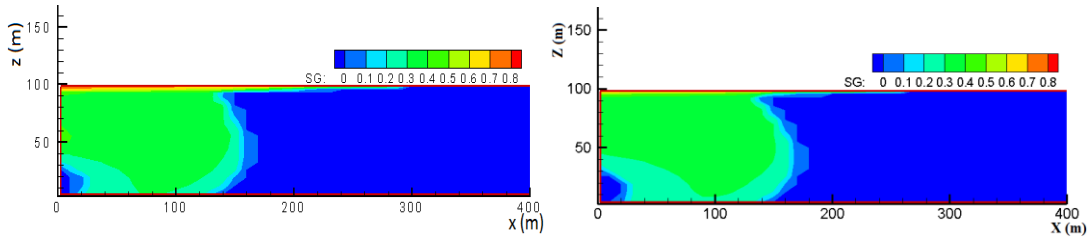

Figure 5.33 CO_2 distribution in the reservoir (left: optimized WAG; right: WAG with variation #2)

Figure 5.34 shows the in situ CO_2 distribution in the reservoir for variation #3 and variation #4 (with shorter and longer WAG cycle duration respectively compared to baseline case).

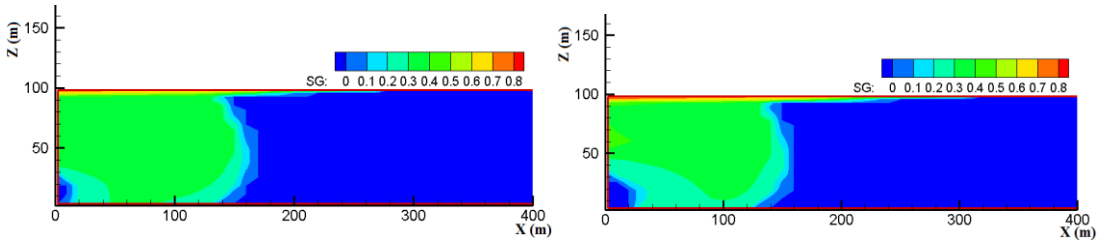

Figure 5.34 CO_2 distribution in the reservoir (left: WAG with variation #3; right: WAG with variation #4)

Since the lateral extent of the CO_2 plume is determined by the gaseous phase concentration beneath the caprock, its saturation is examined for the original optimized WAG operation and its four variations as shown in Figure 5.35.

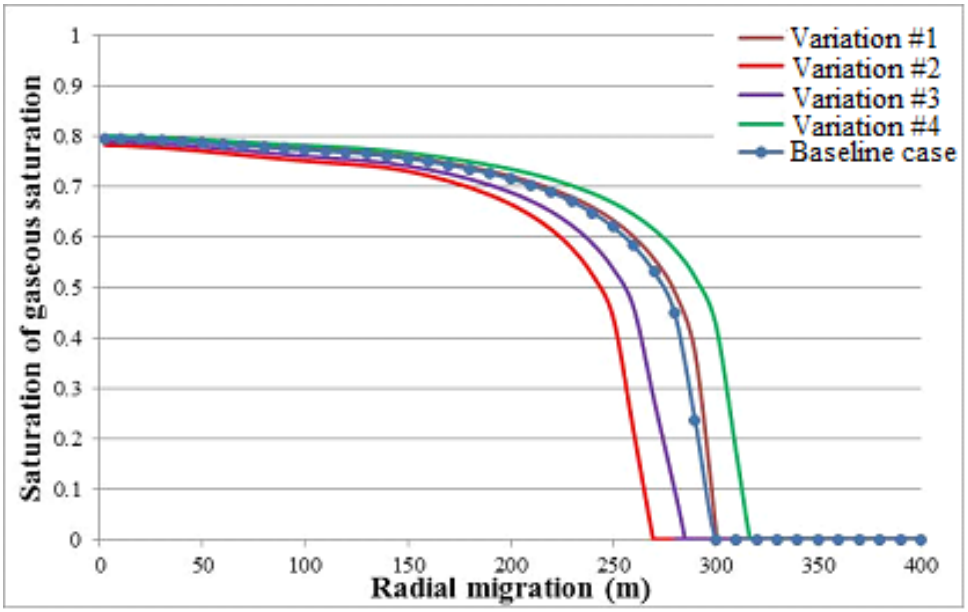

Figure 5.35 SG underneath the caprock, original optimized WAG operation and its four variations

Table 5.19 shows the relative performance of the original optimized WAG operation and its four variations.

Table 5.19 Performance of the original optimized WAG operation and its variations

	Baseline case	Variation#1	Variation#2	Variation#3	Variation#4
Total CO_2 injection (kg)	821917	821917	821917	821917	821917
Total water injection (kg)	973574	1179222	1454722	973574	973574
WAG ratio	0.847	0.697	0.565	0.847	0.847
Maximum migration (m)	290	301	270	280	317
Migration reduction (m)	140	129	160	150	113
Fitness value ($m/10^3$ tons water)	0.1438	0.1096	0.1103	0.1545	0.1166

The results from above sensitivity analysis are very informative; the following conclusions can be made. First, none of the four additional cases with slight variations in WAG operational parameters led to higher fitness function value than the optimized

baseline case. This result further validates the optimization capability of GA-TOUGH2. Secondly, CO_2 migration reduction is obtained in all the four cases. Variation case #2 and #4 even achieve greater reduction in migration compared to the baseline case. However, cases with greater migration reduction may not be desirable because the energy penalty (additional water requirement) is more severe for these cases. Third, the crucial role of WAG cycle duration on its performance is also evident. It is clearly that the shorter WAG cycle duration is preferable for efficient WAG operation due to the resulting enhanced mixing of CO_2 and water. However, the frequent switching between CO_2 and water injection may to be limited by the existing technology barriers.

5.3 Optimal Pressure Management

There are two reasons that make the injection pressure as one of the most important operational parameter for the success of SAGCS. One is the well injectivity which determines the total amount of CO_2 that can be injected in a given amount of time, and the other is the safety constraint on injection pressure that it should not exceed the formation's fracture pressure. In petroleum engineering, injectivity of an injection well is defined as the net fluid flow delivered per unit pressure differential between the mean injection pressure and the mean formation pressure. The definition of injectivity is given by Eq. 40

$$injectivity = \frac{Q_{CO2}}{p_{injection} - p_{reservior}} \qquad \text{(Eq. 40)}$$

where Q_{CO2} is the injection mass rate and $p_{injection}$ is the injection pressure. Injectivity serves as a quantity indicating the ability of an injection well to deliver supercritical CO_2 into the aquifer.

The injection pressure response for a given SAGCS operation can be analyzed as follows. Applying the Darcy's Law from Eqs. 3 and 4 to the region adjacent to the injection well, the achievable CO_2 injection mass rate Q_{CO2} is proportional to the product of relative permeability $k_{r,g}$ of CO_2 and pressure gradient near the injection well ∇p. For two-phase flow of supercritical CO_2 and brine, $k_{r,g}$ is a function inversely

proportional to the saturation of brine S_b. At an early stage of CO_2 injection, the pore space near the injection well is primarily occupied by the brine, which means high S_b in the adjacent region of the injection well. As a direct consequence, $k_{r,g}$ is relatively low and it results in considerable difficulty to displace brine by injecting CO_2. A direct indicator of this difficulty is the significant elevation of injection pressure, or in other words, very low injectivity. However, CO_2 injectivity does not remain unchanged. As injection continues, more brine is displaced from the pore space adjacent to the injection well, which effectively lowers the S_b. Simultaneously, $k_{r,g}$ increases. The increased $k_{r,g}$ at intermediate and later stages of CO_2 injection results in improvement of CO_2 injectivity. Therefore if the injection rate is assumed constant, one can draw the conclusion that at the beginning of the injection, high injection pressure is required to overcome the low effective permeability of CO_2. However, as more brine is being displaced, injection pressure gradually drops because the permeability of CO_2 increases. Figure 5.36 schematically shows the effect of injection rate on injection pressure with time.

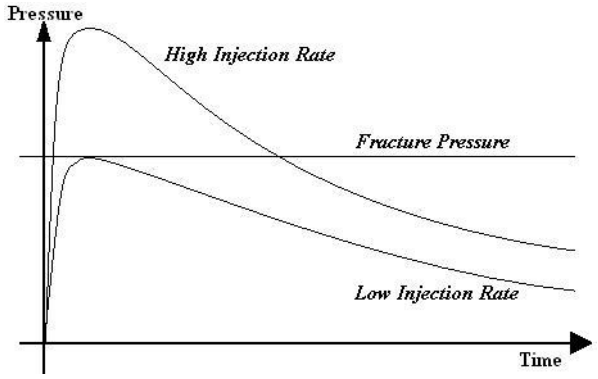

Figure 5.36 Schematic of injection pressure response with time under various CO_2 injection rates

Intuitively, high injection rate is always preferred, since it can lead to more mass injection within a given time. However, higher injection rate requires greater injection pressure. Regardless of the pumping capacity of the available injection equipment to provide required the needed injection pressure, a critical constraint on allowable injection pressure exists. Like all mechanical structures, geological formations can also bear only a certain level of maximum stress to maintain their integrity. They fracture

when exerted with excessive stress. Fractures in a formation can serve as pathways for the in situ mobile CO_2 to migrate to shallower aquifers and even all the way to ground surface. The leakage of CO_2 through geological fracture is potentially threatening to the ecosystem near storage site, needless to say it will also significantly compromise its storage efficiency. Therefore, every attempt should be made to ensure the integrity of the formation, i.e. under no circumstance should the injection pressure exceed the fracture pressure of the formation. Since the fracture pressure is an intrinsic property of the formation, it is likely to remain constant during the injection phase of SAGCS, shown by the horizontal line in Figure 5.36.

Considering the injection pressure response under CGI operation and the fracture pressure guideline, Figure 5.36 reveals a crucial issue that must be addressed. If CO_2 is pumped into the aquifer with a relatively high injection rate (following the "High Injection Rate" scenario in Figure 5.36), the excessive pressure elevation at the early stage of injection can easily jeopardize the integrity of the formation; on the other hand, if CO_2 is pumped with a relatively low injection rate to ensure formation's integrity, the injection will become inefficient at the intermediate and late stage as more CO_2 injection could have been achieved by moderate increase in the injection pressure at these stages. Therefore, the overall injectivity can be improved while sustaining the sequestration security, if the injection rate can be adjusted with respect to time such that the injection pressure levels off as it approaches the fracture pressure and is maintained at that level during the later injection stage. Such a scenario is identified as the constant pressure injection (CPI) since the injection pressure is more or less maintained at a constant level. The concept of CPI fits perfectly well into the category of the development of "smart" injection well for SAGCS.

5.3.1 Methodology of Designing Constant Pressure Injection (CPI)

The setup of optimization problem for CPI is rather straightforward. Prior to the optimization, a threshold pressure (the pressure limit chosen based on the formation's fracture pressure and other engineering concerns and regulations) is chosen as the

optimization constraint. Since it is assumed that the injection rate is the only quantity to be adjusted for CPI, it becomes the design variable. The optimization is then carried out to minimize the fitness function defined by Eq. 41.

$$\text{fitness function} = \text{modified injectivity} = \frac{\left| p_{\text{threshold}} - p_{injection}(Q_{CO2}) \right|}{Q_{CO2}} \qquad \text{(Eq. 41)}$$

With fitness function in Eq. 41 approaching zero, CPI operation is obtained and the corresponding injection scenario can then be determined. The optimization design of CPI operation is carried out using GA-TOUGH2. The optimization is essentially a solution-searching problem utilizing GA optimization technique.

Unlike the optimization of the WAG operation, a new challenge emerges as to describe the CO_2 injection rate as a time-dependent continuous function with limited discrete data. The concept of Bézier curve is introduced to address this problem. A Bézier curve is a parametric curve frequently used in computer graphics and related fields [59],[60]. It is defined by a set of control points, and uses them as coefficients of a certain polynomial to describe continuous curves. The control points of a Bézier curve can be denoted as P_0 through P_n, with (n-1) being the order of the Bézier curve. The order determines the complexity of the Bézier curve. Bézier curve provides a simple means of creating arbitrary complex curves. A generalized mathematical expression of an n^{th} order Bézier curve is given as

$$B(t) = \sum_{i=0}^{n} \binom{n}{i} (1-t)^{n-i} t^i P_i \qquad \text{(Eq. 42)}$$

where (n,i) is the binomial coefficient, P_i is the i^{th} control point defined prior to the generation of Bézier curve, and t is a variable defined on [0,1]. Defining four control points as P_1, P_2, P_3, and P_4, an example of cubic Bézier curve is shown in as Figure 5.37.

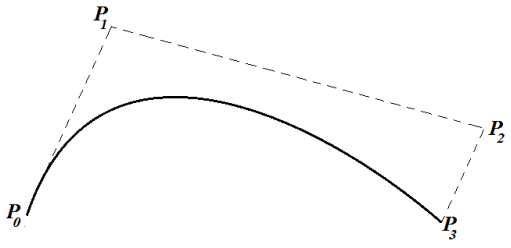

Figure 5.37 Schematic of a cubic (3rd order) Bézier curve

In our research, each CO_2 injection scenario is described by a cubic Bezier curve. The CO_2 injection is a time dependent function of mass flow rate. Discretization of the injection with respect to time is needed to make the problem tractable for numerical simulation. With the discretization, CO_2 injection becomes step-functions for each time interval, and ultimately approximates to the smooth injection as time interval becomes small enough. Injection rate for each discrete time step is described at the midpoint of the interval, known as the sample point. Since both the information of time (*x*-axis) and flow rate (*y*-axis) is needed to describe a certain injection scenario for GA-TOUGH2, an alternative expression of Bézier curve in Cartesian coordinate system has been derived. Assuming that the four control points are $P_0(x_0,y_0)$, $P_1(x_1,y_1)$, $P_2(x_2,y_2)$ and $P_3(x_3,y_3)$, any point $P(x(t),y(t))$ on the Bézier curve can be expressed as

time $$x(t) = A_x t^3 + B_x t^2 + C_x t^1 + x_0 \quad \text{(Eq. 43)}$$

injection rate $$y(t) = A_y t^3 + B_y t^2 + C_y t^1 + y_0 \quad \text{(Eq. 44)}$$

where the coefficients are defined as

$$\begin{aligned} C_x &= 3(x_1 - x_0) & C_y &= 3(y_1 - y_0) \\ B_x &= 3(x_2 - x_1) - C_x & B_y &= 3(y_2 - y_1) - C_y \\ A_x &= x_3 - x_0 - C_x - B_x & A_y &= y_3 - y_0 - C_y - B_y \end{aligned} \quad \text{(Eq. 45)}$$

Because the injection starts at time zero, the first control point is anchored to the *y*-axis by setting $x_0=0$, i.e. $P_0(x_0,y_0)= P_0(0,y_0)$. Coordinates of other control points are arbitrarily generated for each GA individual. With this setup, an arbitrary CO_2 injection scenario beginning at $t=0$ can be generated by letting the parameter *t* increase from 0 to 1.

The design of CPI operation employs the identical hypothetical generic saline formation modeled for the optimization of WAG injection with a horizontal injector, as shown previously in Figure 5.14. All hydrogeological properties and numerical parameters remain unchanged. A threshold pressure of 180 bar is set for the maximum allowable injection pressure with the assumption of a 50% increase from the initial pressure (120 bar). As mentioned earlier, the choice of threshold pressure is based on result by the considerations of various aspects, such as fracture pressure, injection regulation, safety factor, and risk analysis. The injection rate is allowed to vary between 0 kg/s to 150 kg/s, and the injection lasts for 5 years. Parameters of the GA optimizer are summarized in Table 5.20.

Table 5.20 GA parameters for designs of CPI operation

Number of Individual per Generation	6
Maximum Number of Generations	100
Natural Selection Algorithm	Bubble Sort, 50% Elimination
Mutation Rate	8 %
Cross-over Algorithm	Semi-Random Combination of Parents

The injection pressure response of the optimized CPI operation is given in Figure 5.38; the corresponding time-dependent injection rate is given in Figure 5.39. Two CGI cases, one with high injection rate (44 kg/s) and one with low injection rate (24 kg/s), are also included in these figures for comparison.

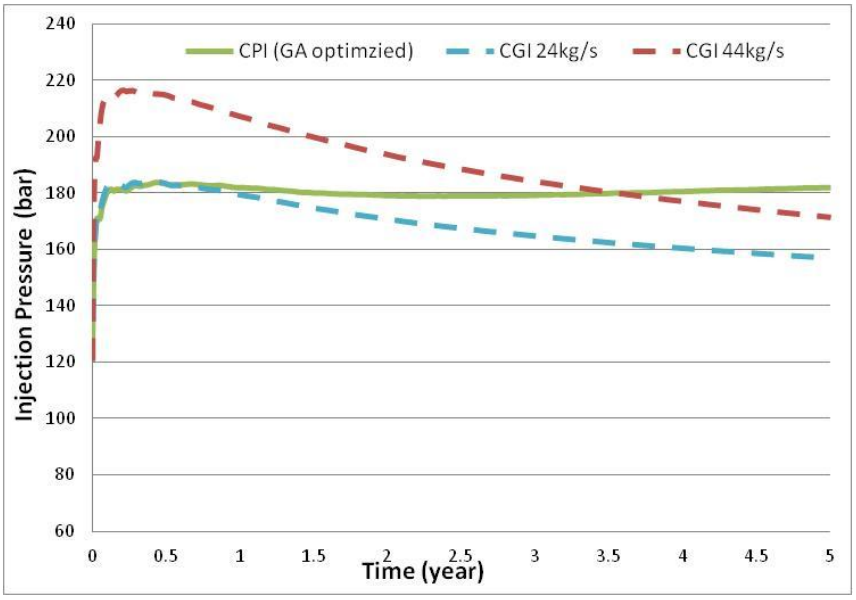

Figure 5.38 Injection pressure response of the optimized CPI operation with low CGI and high CGI

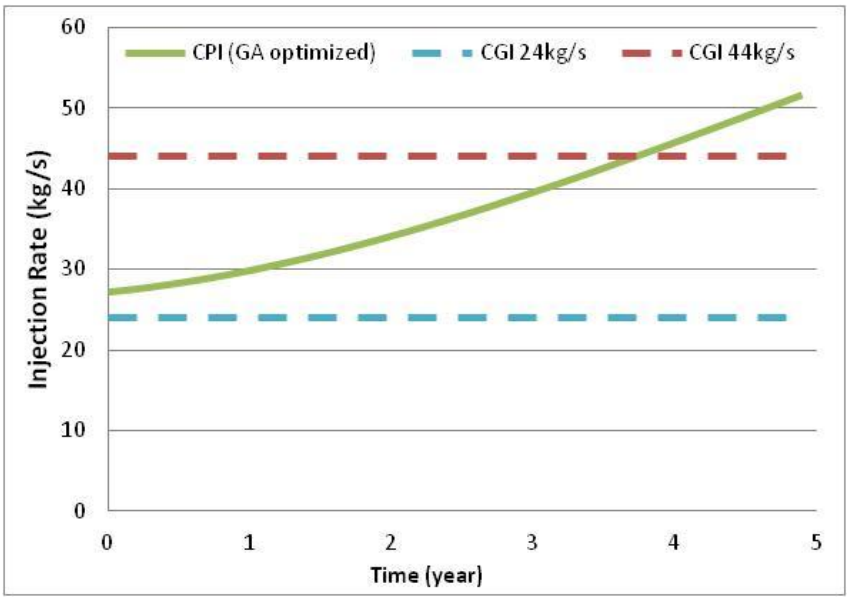

Figure 5.39 Injection scenario of the optimized CPI operation with low CGI and high CGI

Several conclusions can be made by carefully examining the results of Figure 5.38 and Figure 5.39. First, the injection pressure (green curve in Figure 5.38) is well behaved under the constraint of the threshold pressure. It increases rapidly at the early stage of the injection (in the order of days), and levels off as it approaches 180 bar. This is exactly the desired behavior of injection pressure response. Starting from 28 kg/s, the injection rate keeps increasing with the stabilized injection pressure. It means that the well injectivity gradually improves as CO_2 injection continues. Improved injectivity indicates more injected amount of CO_2 after 5-year operation. A direct indicator of the success of the designed CPI operation is the 5-year average injection rate of 38 kg/s (compared to 34 kg/s for CGI operation). Secondly, both CGI operations give first an increase and then a decrease in injection pressure response, validating our previous conclusion. Similar behavior of loss in injectivity has also been suggested by Burton et al. [62]. It can be seen that the injection pressure reaches about 220 bar with the high rate CGI operation (44 kg/s), which is a 40 bar overshoot above the threshold pressure; additionally such pressure overshoot lasts for over 3.5 years before the injection pressure falls below 180 bar. Such large and prolonged pressure overshoot poses a significant risk to the formation's integrity. On the other hand, it is also seen that the injection pressure response with the low rate CGI operation (24 kg/s) falls much below

the threshold pressure after it peaks at the early stage. Although the integrity of the formation is not threatened, the injectivity has been severely compromised under such low injection rate. Thus, only the CPI operation gives the optimal injection pressure management which realizes the best injectivity while ensuring the injection safety by keeping the pressure always below the fracture pressure of the formation. Again, GA-TOUGH2 has successfully designed the CPI operation for a given pressure constraint.

5.4 Performance Optimization of a Multi-well System

It is likely that only a system of multiple injection wells would deliver enough injectivity for industrial level SAGCS. In the presence of multiple wells, the low compressibility of brine can potentially result in strong interference in pressure generated by each well. It then brings up the question of how much is the pressure interference generated in a multi-well injection system, and how the injection wells should be placed to have interference minimized.

Two types of interference have been identified in a multi-well injection system, namely the CO_2 front interference and the pressure front interference, as described by Eccles et al. [63]. Neglecting complex in situ interactions such as phase shifting and mineralization, the interface between injection wells can be roughly estimated by superposition of the quantities from each single-well injection. A schematic of the desired and undesired well spacing is shown in Figure 5.40.

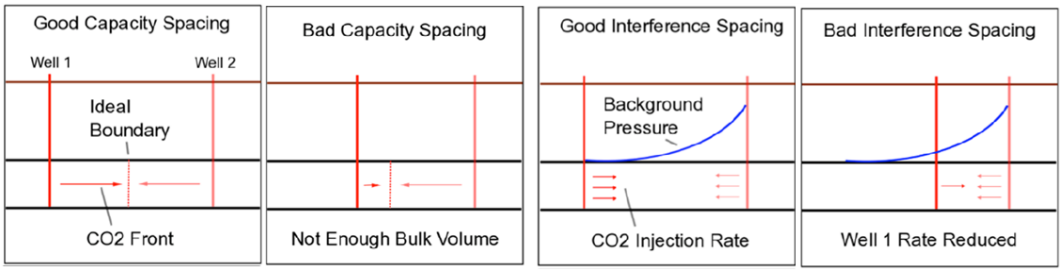

Figure 5.40 Favorable and unfavorable capacity and interference spacing [64]

If the aquifer is assumed to be relatively isotropic in its hydrogeological properties, Darvish et al. have shown that placing the wells on corners of regular polygons is preferred for uniform interference among wells [64]. Following this suggestion, the preferred well distribution for a 2-well, 3-well, and 4-well system can be obtained as shown schematically in Figure 5.41.

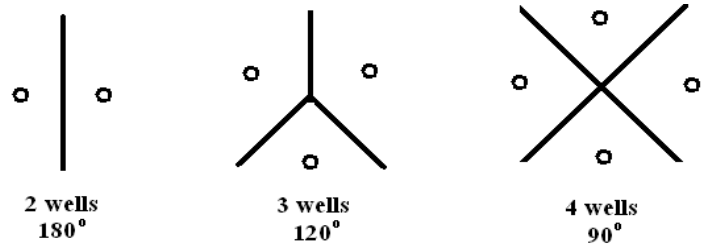

Figure 5.41 Preferred angular distribution for a 2-well, 3-well, and 4-well system

With the preferred angular distribution of injection wells as shown in Figure 5.41, the distance among the wells becomes the design variable for optimization. A four-well injection system is first considered to investigate the interference of plume migration and pressure disturbance between the wells. Afterwards a two-well injection system is considered to study the relationship between well spacing and injectivity.

5.4.1 Four-well Injection System

A hypothetical saline aquifer with dimensions 4000 m × 4000 m × 70 m is modeled for this study. Generic hydrogeological properties and reservoir conditions similar to those used in the WAG operation study are assigned. Computational mesh is refined near the injection wells for accurate capture of the interference. Four cases with different inter-well distance are considered, in which injection wells are 600 m, 800 m, 1200 m, and 1600 m diagonally apart. The computational domains for the four cases are shown in Figure 5.42.

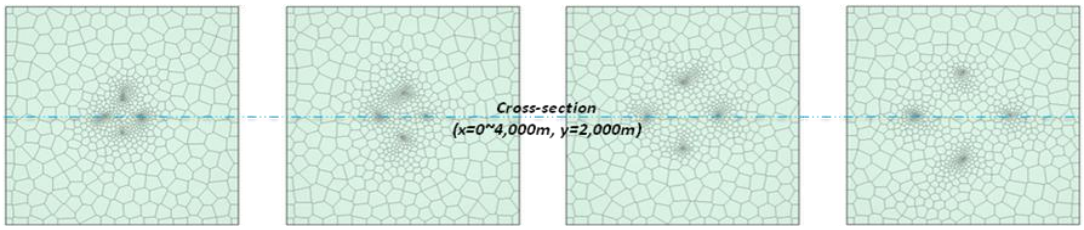

Figure 5.42 Computational domain of four-well injection systems with various inter-well distance

CO_2 is injected at constant rate of 5 kg/s at each well. Mean injection pressure and gas saturation underneath the caprock after 5 years of injection is examined along the cross section indicated in Figure 5.42. The pressure response and CO_2 saturation curves are shown and compared in Figure 5.43 and Figure 5.44 respectively.

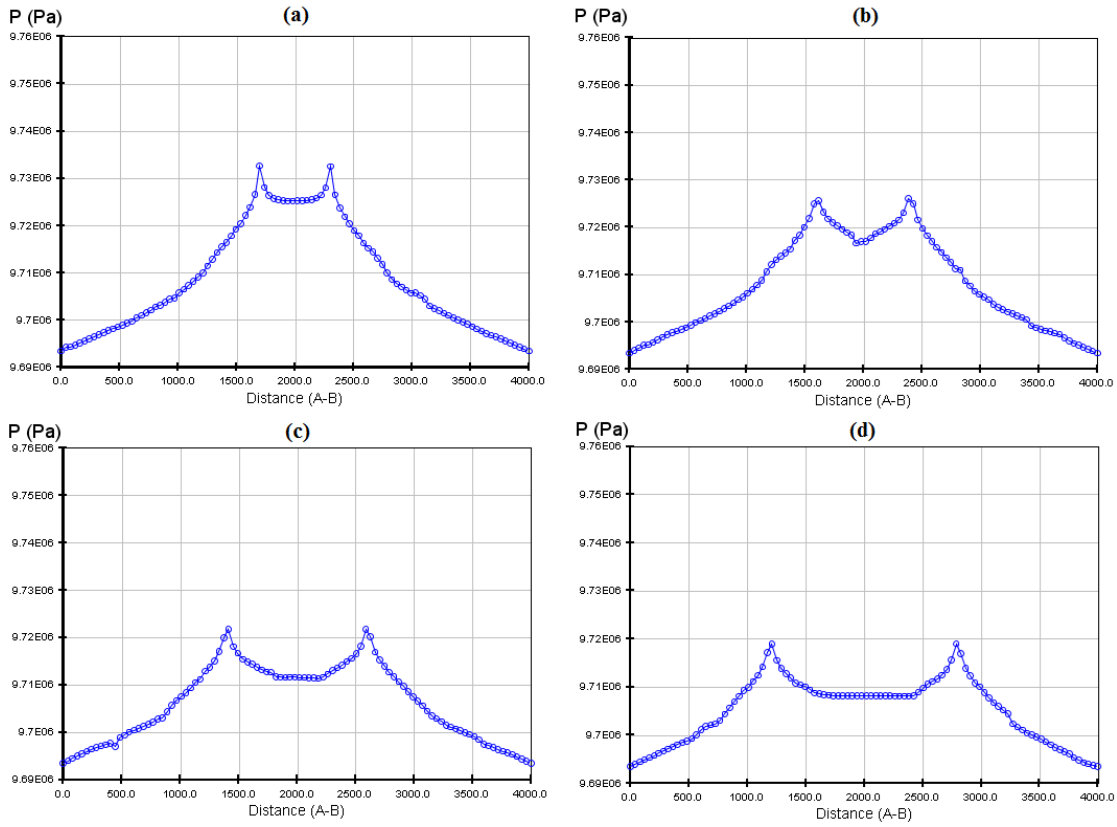

Figure 5.43 Pressure profile at the cross-section: (a) wells 600 m apart, (b) 800 m apart, (c) 1200 m apart, and (d) 1600 m apart

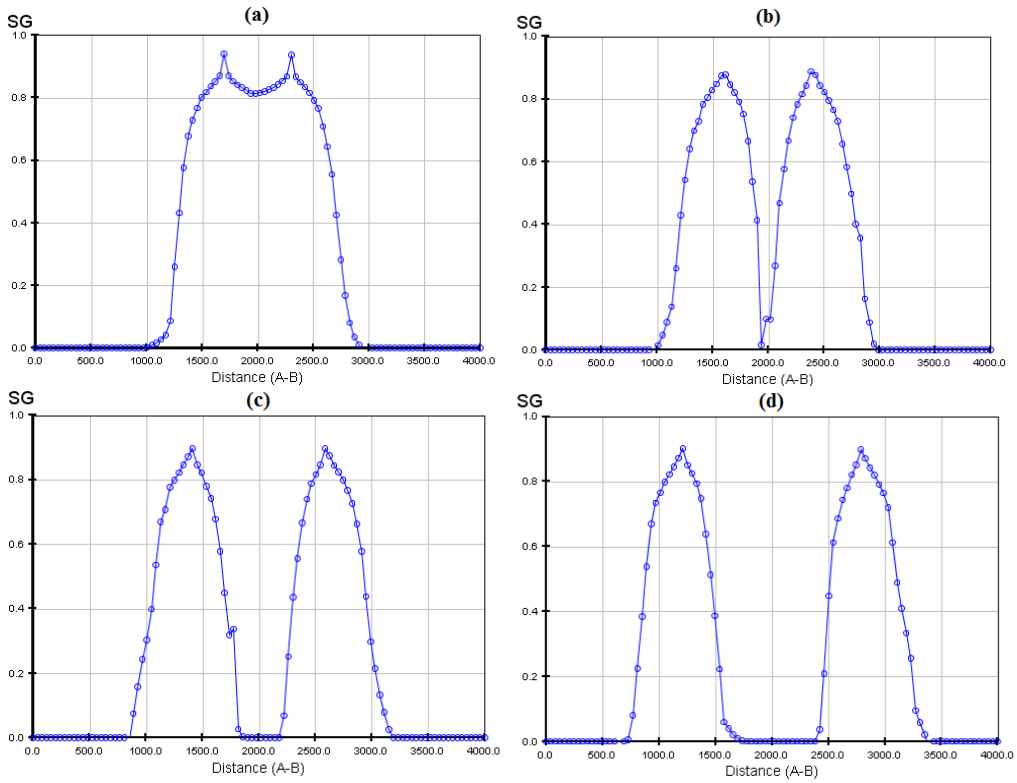

Figure 5.44 Gas saturation underneath the caprock at the cross-section: (a) wells 600 m apart, (b) 800 m apart, (c) 1200 m apart, and (d) 1600 m apart

Following conclusions can be made based on the results shown in Figure 5.43 and Figure 5.44. First, well injectivity can be greatly improved by utilization of a multi-well injection system. The four-well system considered delivers CO_2 at total rate of 20 kg/s with no greater than 0.4 % increase in reservoir pressure. This is orders of magnitude smaller than that of a single injection well for the same injection rate. It shows the technical benefit of utilizing a multi-well injection system for industrial level SAGCS. Secondly, well interference is prominent due to the presence of multiple injection wells. In Figure 5.43, the injection induced pressure elevation is 0.38 % of the reservoir mean pressure for the case of 600-m inter-well spacing, while it drops to only 0.26 % for the case of 1600 m inter-well spacing. That is to say, pressure interface is about 32 % stronger when injection wells are 600 m apart compared to when they are 1600 m apart. The interference of CO_2 plume is also seen in Figure 5.44. Thirdly, comparison of Figure 5.43 and Figure 5.44 shows that the pressure interference is dominantly

responsible for the compromised injectivity in multi-well injection system. Plume interference can be easily avoided by moderately increasing the well-spacing. For instance, plume interference is prominent for 600 m inter-well spacing, but almost disappears for 800 m inter-well spacing (as shown in Figure 5.44). On the other hand, the pressure interference remains persistent, which requires at least 1600 m inter-well spacing to become insignificant. However, large spacing between injection wells may result in greater land use. Therefore an optimal placement of wells is desirable to achieve an acceptable pressure and capacity interference as well as land use.

5.4.2 Two-well Injection System

Because pressure interference is largely responsible for compromised injectivity of a multi-well injection system, in this section we examine the relationship between inter-well spacing and well injectivity. A half domain with dimensions 50000 m × 25000 m × 100 m is modeled. The computational domain is horizontally discretized by a uniform quadrilateral mesh with resolution of 200 m × 200 m and 500 m × 500 m. Two injection wells are assigned symmetrically at the center of the domain. The distance between these two injection wells is allowed to change freely and is considered as a design variable for the GA optimizer. Similar to the previous investigations of four-well injection system, the injection operation is assumed to last for 5 years. Three cases with different injection rates and model parameters are considered, which are summarized in Table 5.21.

Table 5.21 Optimization cases for two-well injection system

	Case #1	**Case #2**	**Case #3**
Single well injection rate	2 kg/s	16 kg/s	16 kg/s
Hydrogeological properties	Generic formation	Generic formation	Generalized Utsira formation
Mesh resolution	200 m × 200 m	500 m × 500 m	500 m × 500 m

Denoting the injection pressure of the two-well injection system as $P_{two\text{-}well}$, and the injection pressure of the single-well injection system as $P_{single\text{-}well}$, the pressure difference ΔP between $P_{two\text{-}well}$ and $P_{single\text{-}well}$ is chosen as the fitness function. GA-TOUGH2 is

employed to determine the minimal inter-well distance for a designated value of ΔP. For each case in Table 5.21, three optimization criteria are considered, namely ΔP being no greater than 0.1%, 0.5%, and 2% of $P_{single\text{-}well}$. The value of ΔP is examined and optimization is performed at the end of the 5-year injection. In addition, well injectivity loss due to the pressure interference is also evaluated for the optimal well spacing given by GA-TOUGH2. Recalling the definition of well injectivity, Eq. 36, the injectivity loss of the two-well injection system can be evaluated as

$$\begin{aligned}\text{injectivity loss} &= \text{injectivity}_{\text{two-well system}} - \text{injectivity}_{\text{single-well system}} \\ &= \left(\frac{Q_{CO2}}{P_{\text{two-well}} - P_{\text{reservior}}} - \frac{Q_{CO2}}{P_{\text{single-well}} - P_{\text{reservior}}} \right) \Bigg/ \frac{Q_{CO2}}{P_{\text{sin}\,glewell} - P_{reservior}} \\ &= \frac{P_{\text{two-well}} - P_{\text{single-well}}}{P_{\text{single-well}} - P_{\text{reservior}}}\end{aligned} \quad \text{(Eq. 46)}$$

where Q_{CO2}, $P_{two\text{-}well}$, and $P_{single\text{-}well}$ have been defined earlier.

The optimization results are summarized in Table 5.22.

Table 5.22 Optimal inter-well spacing and injectivity trade-off for three cases under three optimization criteria

	Case #1		Case #2		Case #3	
Optimization criteria	**Inter-well distance**	**Injectivity loss**	**Inter-well distance**	**Injectivity loss**	**Inter-well distance**	**Injectivity loss**
$\Delta P < 0.1\% P_{single\text{-}well}$	5.4 km	-2.84%	32 km	-0.94%	14 km	-2.53%
$\Delta P < 0.5\% P_{single\text{-}well}$	1.8 km	-12.76%	19 km	-4.54%	below mesh resolution	
$\Delta P < 2\% P_{single\text{-}well}$	below mesh resolution		6.5 km	-28.57%	below mesh resolution	

Several conclusions can be made after careful examination of the optimization results in Table 5.22. First, it should be noted that the total amount of injected CO_2 is doubled from the single-well injection case for all optimization cases due to the presence of the second injection well. Secondly, the results show that for Case #1 pressure interference can be significantly avoided for ($\Delta P < 0.1\%$ of $P_{single\text{-}well}$) by placing injection wells 5400

m apart, for (ΔP < 0.5% of $P_{single\ well}$) by placing injection wells 1800 m apart, and for (ΔP < 2% of $P_{single\ well}$) by placing injection wells less than 200 m apart. The relative ease of mitigating the pressure interface for Case #1 can be explained by its low injection rate of 2 kg/s per well. However, low injection rate leads to low injection pressure, which in turn makes the injectivity more sensitive to injection pressure. 2.84% and 12.76% injectivity loss is found for Case #2 and Case #1 respectively. Case #2 is similar to Case #1 except for the significantly increased injection rate of 16 kg/s per well. Accordingly, the inter-well distance increases to meet the optimization criteria. It is estimated that at least 32 km, 19 km, and 6500 m distance between the wells is needed to realize the three levels of avoidance in pressure interference respectively. An encouraging result is that the injectivity loss for Case #2 is significantly smaller than that for Case #1. Such reduction in injectivity loss also implies the dominant role of injection rate when evaluating the injectivity of a multi-well injection system. Therefore, simply increasing the injection rate can be a direct and effective means to mitigate the injectivity loss due to pressure interference. However, it is worth noting that even for the reasonable avoidance of pressure interference in Case #2, the wells need to be placed 6500 m apart, which is still a significant distance considering the land use. The exacerbated injectivity loss of 28.57% may also pose concerns on injection well performance. In Case #3, the hydrogeological properties of the Utsira sandstone formation are assigned to the modeled domain to obtain some real-life sense of the performance of a multi-well injection system. Due to the improved reservoir conditions, i.e. higher porosity and permeability, the inter-well distance to achieve the significant avoidance of pressure interference decreases greatly from 32 km in Case #2 to 14 km in Case #3. Moreover, the required inter-well distances even fall under the mesh resolution, i.e. less than 500 m, for the other less rigorous criteria in pressure interference. This suggests the great potential of implementing a multi-well injection system to the SAGCS for Utsira formation without concern of large pressure interference. These results also show promise for implementing a multi-well injection system for other large scale saline formations.

Concluding Remarks

In this dissertation, some key factors relevant to of saline aquifer geological carbon sequestration (SAGCS) have been investigated. In Chapter 4, numerical simulations have been performed for proposed/completed/ongoing SAGCS projects on three large scale identified saline formations using the DOE numerical simulator TOUGH2. Before performing these studies, TOUGH2 was validated against the available analytical solutions and the benchmark numerical test cases. These three studies have provided important insights into the reservoir performance and sequestration uncertainties. In Chapter 5, the development of a generic-algorithm based optimizations has been described which has been integrated into TOUGH2; the new code has been designated as GA-TOUGH2. GA-TOUGH2 has the ability to determine optimal reservoir engineering techniques for improved CO_2 storage efficiency in saline aquifer carbon sequestration. Using GA-TOUGH2, the feasibility and technical benefits of adopting water-alternating-gas (WAG) injection technique has been investigated for SAGCS. In addition, the problem such as optimal injection pressure management in SAGCS and well placement in a multi-well injection system have been investigated for the purpose of achieving higher storage efficiency and safer sequestration. Encouraging results have been obtained from all these optimization studies. Validated GA-TOUGH2 thus offers an innovative platform which holds great promise in studying a host of optimization/design problems for geological carbon sequestration.

As recommendations for the future work, more complex optimization studies could be performed to address a broader set of optimization problems, such as non-uniform WAG injection and maximization of capillary trapping. Some analytical solutions could be derived for more fundamental understanding of the WAG injection. Multi-objective GA optimization should also be introduced to obtained higher level of optimization capability with consideration of multiple fitness functions. Additional real-life SAGCS projects such as the ADM project should be continually studied over the years as more detailed field data becomes available. Optimization studies for these large scale SAGCS

projects should be performed for greater storage efficiency and reduced plume migration. GA-TOUGH2 should also be considered for the study of other aspects of GCS such as enhanced oil or gas recovery in combination with carbon sequestration.

References

[1] World Energy Consumption, *Wikipedia* website, http://en.wikipedia.org/wiki/World_energy_resources_and_consumption.

[2] International Energy Outlook 2010, *US Energy Information Administration, Office of Integrated Analysis and Forecasting, US Department of Energy*, July 2010.

[3] R. Agarwal, L. Chusak, and Z. Zhang, Economics of Carbon Dioxide Sequestration and Mitigation versus a Suite of Alternative Renewable Energy Sources for Electricity Generation in US, *10th Annual Conference on Carbon Capture and Sequestration*, Pittsburg, PA, May 2011.

[4] Carbon Dioxide Information Analysis Center, *US Environmental Protection Agency* website, http://www.epa.gov/climatechange/ emissions/globalghg.html

[5] S. Solomon, D. Qin, M. Manning, Z. Chen, M. Marquis, K. B. Averyt, M. Tignor, and H.L. Miller (eds.), IPCC Fourth Assessment Report: Climate Change 2007, *Cambridge University Press*, 2007.

[6] J. Hansen, M. Sato, R. Ruedy, K. Lo, D. W. Lea, and M. Medina-Elizade, Global Temperature Change, *Proceedings of National Academy of Sciences*, 2006, Vol. 103, No. 39.

[7] I. Wright, Industrial-Scale CCS Projects: US and International, *National Energy Technology Laboratory CCS Conference*, Pittsburgh , PA, May 2007.

[8] Arctic Sea Ice Shrinks to New Low in Satellite Era, *NASA* website, http://www.nasa.gov/topics/earth/features/arctic-seaice-2012.html

[9] 2010 Carbon Sequestration Atlas of the United States and Canada, 3rd Edition, *US Department of Energy, Office of Fossil Energy*, 2010.

[10] K.S. Lackner, A Guide to CO_2 Sequestration, *Science*, 13 June 2003, Vol. 300 no. 5626 pp. 1677-1678, DOI: 10.1126/science.1079033

[11] M. L. Szulczewskia, C. W. MacMinnb, H. J. Herzogc, and R. Juanesa, Lifetime of Carbon Capture and Storage as A Climate-Change Mitigation Technology,

Proceedings of the National Academy of Science of the United States of America, Vol. 109, No.14, pp. 5185-5189.

[12] R. A. Esposito, J. C. Pashin, and P. M. Walsh, Citronelle Dome: A Giant Opportunity for Multizone Carbon Storage and Enhanced Oil Recovery in the Mississippi Interior Salt Basin of Alabama", *Environmental Geosciences*, 2008, Vol. 15, No. 2, pp. 53-62.

[13] Fact Sheet on Carbon Capture and Storage, *National Mining Association* website, http://www.nma.org/pdf/fact_sheets/ccs.pdf

[14] H. Herzog and D. Golomb, Carbon Capture and Storage from Fossil Fuel Use, *Encyclopedia of Energy*, 2004, Vol. 1.

[15] J. W. Johnson, J. J. Nitao, and K. G. Knauss, Reactive Transport Modelling of CO_2 Storage in Saline Aquifers to Elucidate Fundamental Processes, Trapping Mechanisms, and Sequestration Partitioning, *Geological Society of London Special Publication on Carbon Sequestration Technologies,* July 29, 2004

[16] B. Metz, O. Davidson, H. de Coninck, M. Loos, and L. Meyer (eds.), IPCC Special Report on Carbon Dioxide Capture and Storage, *Cambridge University Press*, 2005.

[17] 2008 Carbon Sequestration ATLAS of the United States and Canada, *US Department of Energy, Office of Fossil Energy*, 2008.

[18] Plains CO_2 Reduction (PCOR) Partnership - Development Phase, *National Energy Technology Laboratory* website, http://www.netl.doe.gov/technologies/carbon_seq/core_rd/RegionalPartnership/PCOR-DP.htm

[19] Southeast Regional Carbon Sequestration (SECARB) Partnership - Development Phase, *National Energy Technology Laboratory* website http://www.netl.doe.gov/technologies/carbon_seq/core_rd/RegionalPartnership/SECARB-DP.html

[20] 2008 Carbon Sequestration ATLAS of the Midwest Geological Sequestration Consortium, *US Department of Energy, Office of Fossil Energy*, 2008.

[21] Shallow Carbon Sequestration Demonstration Project, *National Energy Technology Laboratory* website http://www.netl.doe.gov/publications/factsheets/project/Proj587.pdf

[22] FutureGen 2.0 Project*, FutureGen Alliance* website, http://www.futuregenalliance.org/futuregen-2-0-project/

[23] M. A. Celia and J. M. Nordbotten, Practical Modeling Approaches for Geological Storage of Carbon Dioxide, *Underground Water*, 2009, Vol. 47, No. 5, pp. 627-638.

[24] M. A. Celia and J. M. Nordbotten, How Simple Can We Make Models for CO_2 Injection, Migration, and Leakage?, *Energy Procedia*, 2001, Vol. 4, pp. 3857-3864.

[25] K. Pruess, TOUGH2: A General Numerical Simulator for Multiphase Fluid and Heat Flow, *Lawrence Berkeley Laboratory Report LBL-29400*, Berkeley, CA, 1999.

[26] K. Pruess, C. Oldenburg, and G. Moridis, TOUGH2 User's Guide, Version 2.0 (revised), *Lawrence Berkeley Laboratory Report LBL-43134*, Berkeley, CA, 2011.

[27] S. Bachu, J. M. Nordbotten, and M. A. Celia, Evaluation of the Spread of Acid-Gas Plumes Injected in Deep Saline Aquifers in Western Canada as an Analogue for CO_2 Injection into Continental Sedimentary Basins, *Proceedings of the 7th International Conference on Greenhouse Gas Control Technologies*, September 5-9, 2004, Vancouver, Canada.

[28] M. A. Celia, S. Bachu, J. M. Nordbotten, S. Gasda, and H. Dahle. Quantitative Estimation of CO_2 Leakage from Geological Storage: Analytical Models, Numerical Models, and Data Needs, *Proceedings of the 7th International Conference on Greenhouse Gas Control Technologies*, September 5-9, 2004, Vancouver, Canada.

[29] J. M. Nordbotten, M. A. Celia, and S. Bachu, Injection and Storage of CO_2 in Deep Saline Aquifers: Analytical Solution for CO_2 Plume Evolution During Injection, *Transport in Porous Media*, 2005, Vol. 58, No. 3, pp. 339-360(22)

[30] S. E. Buckley and M. C. Leverett, Mechanism of Fluid Displacement in Sands. *Transactions AIME*, 1942, Vol. 146: 107-116.

[31] Genetic algorithm, *Wikipedia* website, http://en.wikipedia.org/wiki/Genetic_algorithm

[32] D. E. Goldberg, Genetic Algorithms in Search, Optimization & Machine Learning, *Addison-Wesley*, 1989.

[33] PetraSim User Manual, *Thunderhead Engineering* website, http://www.thunderheadeng.com/downloads/petrasim/PetraSim-4-manual.pdf

[34] PetraSim Example Manual, *Thunderhead Engineering* website, http://www.thunderheadeng.com/downloads/petrasim/4/examples/PetraSimExamples.pdf

[35] Workshop on Numerical Models for Carbon Dioxide Storage in Geological Formations, *University of Stuttgart* website, http://www.iws.uni-stuttgart.de/CO2-workshop/

[36] A. Ebigbo, J. M. Nordbotten, and H. Class, Numerical Investigations of CO_2 Sequestration in Geological Formations: Problem-Oriented Benchmarks, Problem 1, CO_2 Plume Evolution and Leakage through an Abandoned Well, *R&D-Program of GEOTECHNOLOGIEN* website, http://www.hydrosys.uni-stuttgart.de/co2-workshop/Problem1.pdf

[37] A. Ebigbo, J. M. Nordbotten, and H. Class, Numerical Investigations of CO_2 Sequestration in Geological Formations: Problem-Oriented Benchmarks, Problem 2, Enhanced CH4 Recovery in Combination with CO_2 Storage in Depleted Gas Reservoirs, *R&D-Program of GEOTECHNOLOGIEN* website, http://www.hydrosys.uni-stuttgart.de/co2-workshop/Problem2.pdf

[38] A. Ebigbo, J. M. Nordbotten, H. Class, and G. Eigestad Numerical Investigations of CO_2 Sequestration in Geological Formations: Problem-Oriented Benchmarks, Problem 3, Estimation of the CO_2 Storage Capacity of a Geological Formation, *R&D-Program of GEOTECHNOLOGIEN* website, http://www.hydrosys.uni-stuttgart.de/co2-workshop/Problem3.pdf

[39] H. Class, A. Ebigbo, H. Rainer, H.K. Dahle, J. M. Nordbotten, M. A. Celia, P. Audigane, M. Darcis, J. Ennis-King, and Y. Fan, A Benchmark Study on Problems Related to CO_2 Storage in Geologic Formations, *Computational Geosciences*, 2009, Vol. 13, pp. 409-434.

[40] H. E. Leetaru, S. M. Frailey, J. Damico, R. Finley, J. H. McBride, and D. G. Morse, Developing a Geological Model for the Phase III (ADM) Saline Sequestration Validation Site. *7th Annual Conference on Carbon Capture and Sequestration*, Pittsburgh, PA, May 2008.

[41] D. A. Barnes, D. H. Bacon, and S. R. Kelley, Geological sequestration of carbon dioxide in the Cambrian Mount Simon Sandstone: Regional Storage Capacity, Site Characterization, and Large scale Injection Feasibility, Michigan Basin, *Environmental Geosciences*, 2009, Vol. 16, No. 3, pp. 163-183

[42] Midwest Regional Carbon Sequestration Partnership, CO_2 Injection Test in the Cambrian-Age Mt. Simon Formation, *Final Report*, April 29, 2011.

[43] Q. Zhou, J. T. Birkholzer, E. Mehnert, Y, Lin, and K. Zhang, Modeling Basin- and Plume-Scale Processes of CO_2 Storage for Full-Scale Deployment, *Ground Water*, 2010, Vol. 48, No. 4, pp: 494–514.

[44] S. D. Hovorka, S. M. Benson, C. Doughty, B. M. Freifeld, S. Sakurai, T. M. Daley, Y. K. Kharaka, M. H. Holtz, R. C. Trautz, H. S. Nance, L. R. Meyer, and K. G. Knauss, Measuring Permanence of CO_2 Storage in Saline Formations—the Frio Experiment, *Environmental Geosciences*, 2006, Vol. 13, No. 2, pp: 105–121.

[45] C. Doughty, B. M. Freifeld, and R. C. Trautz, Site Characterization for CO_2 Geologic Storage and Vice Versa: The Frio Brine Pilot, Texas, USA as A Case Study, *Environmental Geology*, 2008, Vol. 54, pp: 1635–1656.

[46] S. Bachu, B. Bennion, Effects of In-situ Conditions on Relative Permeability Characteristics of CO_2-Brine Systems, *Environmental Geology*, 2007, Vol. 54, pp: 1635–1656.

[47] R. A. Chadwick and D. J. Noy, History-matching Flow Simulations and Time-lapse Seismic Data from the Sleipner CO_2 Plume, *Proceedings of the 7th Petroleum Geology Conference*, 2010, Vol. 7, pp. 1171–1182

[48] P. Audigane, I. Gaus, I. Czernichowski-Lauriol, K. Pruess, and T. Xu, Two-Dimensional Reactive Transport Modeling of CO_2 Injection in a Saline Aquifer at the Sleipner Site, *American Journal of Science*, 2007, Vol. 307, pp: 974-1008.

[49] V. Singh, A. Cavanagh, H. Hansen, B. Nazarian, M. Iding, and P. Ringrose, Reservoir Modeling of CO_2 Plume Behavior Calibrated Against Monitoring Data from Sleipner, Norway, *Society of Petroleum Engineers*, 2010, 134891-PP.

[50] C. Zhu, CO_2-water-rock Interaction in Geological Carbon Sequestration, seminar presentation at Washington University in St. Louis, 2011.

[51] C. Zhu and P. Lu, Personal Communication, Department of Geological Sciences, University of Indiana, 2012

[52] H. Tchelepi, L. Durlofsky, and K. Aziz, A Numerical Simulation Framework for the Design, Management and Optimization of CO_2 Sequestration in Subsurface Formations, *Global Climate and Energy Project (GCEP) Report*, Stanford, 2009.

[53] L. Orr, Carbon Capture and Sequestration: Where do We Stand?, *Presentation at NAE/AAES Convocation*, Washington DC, 19 April, 2010.

[54] S. L. Bryant, S. Lakshminarasimhan, and G. A. Pope, Buoyancy-dominated Multi-Phase Flow and Its Effect on Geological Sequestration of CO_2, *Society of Petroleum Engineers Journal*, 2008, pp. 447-454.

[55] Y. Leonenko and D. W. Keith, Reservoir Engineering to Accelerate the Dissolution of CO_2 Stored in Aquifers, *Environmental Science & Technology*, 2008, Vol. 42, pp. 2742-2747.

[56] S. A. Jikich, W. N. Sams, G. Bromhal, G. Pope, N. Gupta, and D. H. Smith, Carbon Dioxide Injectivity in Brine Reservoirs Using Horizontal Wells, *2nd Annual Conference on Carbon Sequestration*, Pittsburgh, PA, May 2003.

[57] H. Hassanzadeh, M. Pooladi-Darvish, and D. W. Keith, Accelerating CO_2 Dissolution in Saline Aquifers for Geological Storage - Mechanistic and Sensitivity Studies, *Energy and Fuels*, 2009, Vol. 23, pp. 3328-3336.

[58] F. M. Nasir and Y. Y. Chong, The Effect of Different Carbon Dioxide Injection Modes on Oil Recovery, *International Journal of Engineering & Technology*, 2009, Vol. 9, pp: 66-72.

[59] G. Farin, Curves and Surfaces for Computer-Aided Geometric Design, Fourth Edition, *Academic Press*, Waltham 1996.

[60] Bézier curve, *Wikipedia* website, http://en.wikipedia.org/wiki/B%C3%A9zier_curve

[61] D.P Yale., G.W. Nabor, and J.A. Russell, Application of Variable Formation Compressibility for Improved Reservoir Analysis, *Society of Petroleum Engineers*, 1993, 26647.

[62] M. Burton, N. Kumar, and S. L. Bryant, CO_2 Injectivity into Brine Aquifers: Why Relative Permeability Matters as Much as Absolute Permeability, *Energy Procedia*, 2009, Vol. 1, No. 1, pp: 3091-3098.

[63] J. Eccles, M. Chandel, and L. Pratson, Large Scale Carbon Storage Deployment: Effects of Well Spacing on Geosequestration Site Costs and Capacity Estimates, *10th Annual Conference on Carbon Capture & Sequestration*, Pittsburgh, PA, May 2011.

[64] M. Pooladi-Darvish, S. Moghdam, and D. Xu, Multiwell Injectivity for Storage of CO_2 in Aquifers, *Energy Procedia*, 2011, Vol. 4, pp: 4252-4259.

Curriculum Vita

Zheming Zhang

Degrees	Ph.D. Department of Mechanical Engineering & Materials Science, Washington University in St Louis, May 2013 M.S. Department of Mechanical Engineering & Materials Science, Washington University in St Louis, May 2010 B.S. Department of Automotive Engineering, Tsinghua University, July 2008
Professional Societies	Society of Professional Engineers American Society of Mechanical Engineers Society of Petroleum Engineers

Publications

Zheming Zhang, Ramesh Agarwal, Numerical Simulation and Optimization of CO_2 Sequestration in Saline Aquifers for Enhanced Storage Capacity and Secured Sequestration, *International Journal of Energy and Environment*, 2013, Vol. 4, No. 3, pp. 387-398

Zheming Zhang, Ramesh Agarwal, Numerical Simulation of Geological Carbon Sequestration in Saline Aquifers - Three Case Studies, *12th Annual Conference on Carbon Capture Utilization & Sequestration*, Pittsburg, PA, May 2013.

Zheming Zhang, Ramesh Agarwal, Numerical Simulation and Optimization of CO_2 Sequestration in Saline Aquifers, *Computers & Fluids*, DOI:10.1016/j.compfluid.2012.04.027

Zheming Zhang, Ramesh Agarwal, Numerical Simulation and Optimization of CO_2 Sequestration in Saline Aquifers for Vertical and Horizontal Well Injection, *Computational Geosciences*, 2012, Vol. 16, No. 4, pp 891-899

Zheming Zhang, Ramesh Agarwal, Optimization of Reservoir Performance for CO_2 Sequestration in Saline Aquifers, *11th Annual Conference on Carbon Capture Utilization& Sequestration*, Pittsburg, PA, April 2012.

Ramesh Agarwal, Zheming Zhang, and Lee Chusak, Economics of Carbon Dioxide Sequestration versus A Suite of Alternative Renewable Energy Sources for Electricity Generation in US, California and Illinois, *International Journal of Energy Economics and Policy*, 2012, Vol. 2, No. 3, pp. 184-200.

Zheming Zhang, Ramesh Agarwal Numerical Simulation and Optimization of CO_2 Sequestration in Saline Aquifers, *6th International Conference on Energy Sustainability*, San Diego, CA, July 2012

Ramesh Agarwal, Zheming Zhang, and Lee Chusak, Economic Impact of CO_2 Sequestration and Mitigation versus A Suite of Alternative Renewable Energy Sources for Electricity Generation at US National Level and State Level, *11th Annual Conference on Carbon Capture Utilization & Sequestration*, Pittsburg, PA, April 2012

Ramesh Agarwal, Lee Chusak, and Zheming Zhang, Economics of Carbon Dioxide Sequestration and Mitigation versus A Suite of Alternative Renewable Energy Sources for Electricity Generation in US, *International Journal of Energy Economics and Policy*, 2011, Vol. 1, No. 4, pp.78-94,

Zheming Zhang, Ramesh Agarwal, Numerical Simulation and Optimization of CO_2 Sequestration in Saline Aquifers, *10th Annual Conference on Carbon Capture Utilization & Sequestration*, Pittsburgh, PA, May 2011.

May 2013